N°d'ordre NNT: 2019LYSEI014

THÈSE de DOCTORAT DE L'UNIVERSITÉ DE LYON

préparée au sein de

l'Institut National des Sciences Appliquées de Lyon

École Doctorale 162

Mécanique, Énergétique, Génie civil, Acoustique

Spécialité discipline de doctorat

GÉNIE MÉCANIQUE

Soutenue publiquement le 14 mars 2019, par:

Liangxiao BU

Study of Thermal Homogeneity in Single-Screw Plastication Process

---

Devant le jury composé de:

T. BARRIERE	Professeur (UNIVERSITÉ DE FRANCHE-COMTÉ)	Rapporteur
N. REGNIER	Professeur (ENSBCP INP BORDEAUX)	Rapporteur
N. ALLANIC	MCF-HDR (UNIVERSITÉ DE NANTES)	Examinatrice
C. BARRES	MCF-HDR (INSA-LYON)	Examinatrice
Y. BEREAUX	MCF-HDR (UNIVERSITÉ DE NANTES)	Directeur de thèse
J.Y. CHARMEAU	Professeur (INSA-LYON)	Co-Directeur de thèse

LaMCoS - UMR CNRS 5259 - Site de Plasturgie - INSA de Lyon
85 rue H. Becquerel, 01108 Oyonnax Cedex (FRANCE)

Département FEDORA – INSA Lyon - Ecoles Doctorales – Quinquennal 2016-2020

SIGLE	ECOLE DOCTORALE	NOM ET COORDONNEES DU RESPONSABLE
CHIMIE	**CHIMIE DE LYON** **http://www.edchimie-lyon.fr** Sec : Renée EL MELHEM Bat Blaise Pascal 3e etage secretariat@edchimie-lyon.fr Insa : R. GOURDON	M. Stéphane DANIELE Institut de Recherches sur la Catalyse et l'Environnement de Lyon IRCELYON-UMR 5256 Équipe CDFA 2 avenue Albert Einstein 69626 Villeurbanne cedex directeur@edchimie-lyon.fr
E.E.A.	**ELECTRONIQUE, ELECTROTECHNIQUE, AUTOMATIQUE** **http://edeea.ec-lyon.fr** Sec : M.C. HAVGOUDOUKIAN Ecole-Doctorale.eea@ec-lyon.fr	M. Gérard SCORLETTI Ecole Centrale de Lyon 36 avenue Guy de Collongue 69134 ECULLY Tél : 04.72.18 60.97 Fax : 04 78 43 37 17 Gerard.scorletti@ec-lyon.fr
E2M2	**EVOLUTION, ECOSYSTEME, MICROBIOLOGIE, MODELISATION** **http://e2m2.universite-lyon.fr** Sec : Sylvie ROBERJOT Bât Atrium - UCB Lyon 1 04.72.44.83.62 Insa : H. CHARLES secretariat.e2m2@univ-lyon1.fr	M. Fabrice CORDEY CNRS UMR 5276 Lab. de géologie de Lyon Université Claude Bernard Lyon 1 Bât Géode 2 rue Raphaël Dubois 69622 VILLEURBANNE Cédex Tél : 06.07.53.89.13 cordey@univ-lyon1.fr
EDISS	**INTERDISCIPLINAIRE SCIENCES-SANTE** **http://www.ediss-lyon.fr** Sec : Sylvie ROBERJOT Bât Atrium - UCB Lyon 1 04.72.44.83.62 Insa : M. LAGARDE secretariat.ediss@univ-lyon1.fr	Mme Emmanuelle CANET-SOULAS INSERM U1060, CarMeN lab, Univ. Lyon 1 Bâtiment IMBL 11 avenue Jean Capelle INSA de Lyon 696621 Villeurbanne Tél : 04.72.68.49.09 Fax :04 72 68 49 16 Emmanuelle.canet@univ-lyon1.fr
INFOMATHS	**INFORMATIQUE ET MATHEMATIQUES** **http://infomaths.univ-lyon1.fr** Sec :Renée EL MELHEM Bat Blaise Pascal, 3e étage Tél : 04.72. 43. 80. 46 Fax : 04.72.43.16.87 infomaths@univ-lyon1.fr	M. Luca ZAMBONI Bâtiment Braconnier 43 Boulevard du 11 novembre 1918 69622 VILLEURBANNE Cedex Tél :04 26 23 45 52 zamboni@maths.univ-lyon1.fr
Matériaux	**MATERIAUX DE LYON** **http://ed34.universite-lyon.fr** Sec : Marion COMBE Tél:04-72-43-71-70 –Fax : 87.12 Bat. Direction ed.materiaux@insa-lyon.fr	M. Jean-Yves BUFFIERE INSA de Lyon MATEIS Bâtiment Saint Exupéry 7 avenue Jean Capelle 69621 VILLEURBANNE Cedex Tél : 04.72.43 71.70 Fax 04 72 43 85 28 Ed.materiaux@insa-lyon.fr
MEGA	**MECANIQUE, ENERGETIQUE, GENIE CIVIL, ACOUSTIQUE** **http://mega.universite-lyon.fr** Sec : Marion COMBE Tél:04-72-43-71-70 –Fax : 87.12 Bat. Direction mega@insa-lyon.fr	M. Philippe BOISSE INSA de Lyon Laboratoire LAMCOS Bâtiment Jacquard 25 bis avenue Jean Capelle 69621 VILLEURBANNE Cedex Tél : 04.72 .43.71.70 Fax : 04 72 43 72 37 Philippe.boisse@insa-lyon.fr
ScSo	**ScSo*** **http://recherche.univ-lyon2.fr/scso/** Sec : Viviane POLSINELLI Brigitte DUBOIS Insa : J.Y. TOUSSAINT Tél : 04 78 69 72 76 viviane.polsinelli@univ-lyon2.fr	M. Christian MONTES Université Lyon 2 86 rue Pasteur 69365 LYON Cedex 07 Christian.montes@univ-lyon2.fr

*ScSo : Histoire, Géographie, Aménagement, Urbanisme, Archéologie, Science politique, Sociologie, Anthropologie

Acknowledgements

This thesis is the result of a research work I have carried out between 2015 and 2019 at the Laboratory of Mechanic of Contacts and Structures (LaMCoS), funded by the China Scholarship Council (CSC).

I would like to express my gratitude to all those who helped me during the completion of the thesis. Without their support and encouragement, this thesis would not have reached its present form.

First and foremost, I want to extend my heartfelt gratitude to my supervisor, Professor Yves BÉREAUX, whose patient guidance, valuable suggestion and constant encouragement make me successfully complete this thesis. He has walked me through all the stage of the writing of this thesis. He is one of the most smart, learned, and kind persons I have ever met with. His advice during the whole process of my work helps me make great progress.

Also, I would like to express my sincere gratitude to my co-supervisor, Professor Jean-Yves CHARMEAU, who helps me and my wife a lot in the life, and always forgive me and encourage me when I made silly and embarrassed mistakes and faced difficulties.

I am also grateful to all the members of the jury: Professor Thierry BARRIERE, Professor Nicolas REGNIER, Professor Nadine ALLANIC, and Professor Claire BARRES. Thanks for giving me precious revisions for my thesis and so many encouragements for my future work, and inspiring me to consider my work from other perspectives.

I would like to thank all the teachers and colleagues in the Site de Plasturgie for their feedback, cooperation and of course friendship: Yao AGBESSI, Herve TOLLENAERE, Jordan BIGLIONE, Mahamed DKIER, Isabelle PONCELET, Hayet LAKHDAR, Anne BLOND, Sambor CHHAY, Shubham GUPTA, Chiara BALBINOT, Murat ARLI, Geraldine CABRERA-ALVINO, Ibtissame TOUIL, Hikmet HOUICHI, Khalid LAMNAWAR, Ronan LE-GOFF, Pierre DUMONT, Florian MARTOIA. They have allowed me to enjoy coffee breaks, lunches, and so many other pleasant times.

A special thanks for all of my friends that accompany with me in these years: Bo LU, Xiaodong LIU, Charles PIONCHON, Emilie SMRECNIK, Philippe SITTLER, Théo JACQUEL, Clothilde, Chao ZHANG, Shuai CHEN, Changyi XU. Your present make my life become much more wonderful, and I cherish all the memories of the activities and parties we enjoyed together.

I wish to thank the professors and colleagues who have helped me in IUT-Nantes: Pierre MOUSSEAU, Eric FOUCHER, Antoine ROLLAND, Julien LAUNAY, and Yannick OLIVIER. Your encouragements help me go through the last period of my thesis work successfully.

Last but not least, I would like to express my special thanks to my parents, my father Enyuan BU and my mother Shuhua ZHANG, whose care and support motivate me to move on and make me want to be a better person. A very special thanks to my wife Yao TAN for her love, her support and for giving me so many reasons to be happy and so many motivations to walk forward.

Résumé

La plastification par monovis, utilisée dans l'extrusion et le moulage par injection, est un moyen essentiel de transformer les thermoplastiques courants et techniques. Dans le moulage par injection, un niveau de fiabilité élevé est généralement atteint, ce qui rend ce processus parfaitement adapté à la production de masse. Néanmoins, des fluctuations de processus apparaissent, faisant du contrôle de la qualité des pièces moulées un problème quotidien. Dans ce travail, une modélisation combinée de la plastification, du calcul du point de fonctionnement et de la dispersion laminaire est utilisée pour étudier la manière dont les fluctuations thermiques pourraient être générée et se propager le long de la vis et affecter l'homogénéité de la matière fondue à l'extrémité de la section de dosage. Pour ce faire, nous avons utilisé des modèles de plastification pour relier les modifications des paramètres de traitement aux modifications de la longueur de plastification. De plus, un modèle simple de calcul du débit est utilisé pour relier la géométrie de la vis, la rhéologie du polymère et les paramètres de traitement afin d'obtenir une bonne estimation du débit massique. Par conséquent, nous avons constaté que le temps de séjour typique dans une seule vis est d'environ un dixième de l'échelle de temps de diffusion thermique. Ce temps de séjour est trop court pour que le coefficient de dispersion atteigne une valeur constante mais trop long pour pouvoir négliger la diffusion thermique radiale et recourir à une solution purement convective. Par conséquent, un problème de diffusion-convection complet doit être résolu avec un écoulement de base par déplacement relatif de paroi et par différence de pression. L'importance majeure des paramètres procédé sur la courbe de température moyenne mesurée au cours du temps à l'extrémité de la section de dosage de la vis est démontrée. Lorsque la contre-pression dans l'écoulement est élevée, la fluctuation de température est répartie de manière plus uniforme avec le temps, tandis qu'une chute de pression entraîne une courbe de rupture qui présente un pic de fluctuation plus important. Le logiciel commercial ANSYS Polyflow, appelé Computational Fluid Dynamics (CFD), a été utilisé pour vérifier le modèle.

En outre, une analyse thermique et structurelle a été réalisée sur un cylindre de moulage par injection existant, comportant 3 blocs de verre optiques pour la visualisation, dans le but d'analyser l'effet des conditions de fonctionnement sur le facteur de sécurité des fenêtres en verre existantes. Cette analyse a été réalisée avec ANSYS Workbench (Mechanical), avec des problèmes de contact inclus.

MOTS CLÉS: Simulation numérique, Plastification monovis, Fluctuation thermique, Écoulement par déplacement de paroi et différence de pression, Dispersion laminaire, ANSYS Polyflow/Workbench

Abstract

Single-screw plastication, used in extrusion and in injection molding, is a major way of processing commodity thermoplastics. In injection molding, a high level of reliability is usually achieved that makes this process ideally suited to mass market production. Nonetheless, process fluctuations still appear that make molded part quality control an everyday issue. In this work, a combined modeling of plastication, throughput calculation, and laminar dispersion are used, to investigate how thermal fluctuations could generate and propagate along the screw length and affect the melt homogeneity at the end of the metering section. To do this, we used plastication models to relate changes in processing parameters to changes in the plastication length. Moreover, a simple model of throughput calculation is used to relate the screw geometry, the polymer rheology, and the processing parameters to get a good estimate of the mass flow rate. Hence, we found that the typical residence time in a single screw is around one-tenth of the thermal diffusion timescale. This residence time is too short for the dispersion coefficient to reach a steady state but too long to be able to neglect radial thermal diffusion and resort to a purely convective solution. Therefore, a full diffusion-convection problem has to be solved with a base flow described by the classic pressure and drag velocity field. The major importance of the processing parameters in the breakthrough curve of arbitrary temperature fluctuation at the end of the metering section of the injection molding screw is demonstrated. When the flow back-pressure is high, the temperature fluctuation is spread more evenly with time, whereas a pressure drop in the flow will results in a breakthrough curve which presents a larger peak of fluctuation. A commercial Computational Fluid Dynamics (CFD) software, ANSYS Polyflow, was used to verify the model.

Moreover, a thermal and structural analysis has been performed on an existing injection molding barrel, featuring 3 optical glass blocks for visualization, with the aim of analyzing the effect of operating conditions on the safety factor of the existing glass windows. This analysis was performed using ANSYS Workbench (Mechanical), with contact problems included.

KEYWORDS: Numerical simulation, Single-screw plastication, Thermal fluctuation, Drag and pressure flow, Laminar dispersion, ANSYS Polyflow/Workbench

Contents

Nomenclature

δ_c	Thickness of the melt film C (delay zone)
δ_f	Flight clearance
η	Melt viscosity
γ	Shear rate
μ_k	Eigenvalues
Ω	The frequency of inlet temperature fluctuation
ϕ	Volume fraction of air
ρ_s	Solid density
τ	The dimensionless time
θ	Dimensionless temperature fluctuation
a	Temperature sensitivity
C_p	Solid specific heat
D	The thermal diffusivity of polymer melt
D_b	Internal barrel diameter
D_s	External screw diameter
f_b	Polymer-barrel frictional coefficients
f_s	Polymer-screw frictional coefficients
G	Pressure gradient along the screw channel
H	Metering zone depth
H_f	Feed zone depth

K	Power-law consistency
k_{air}	Thermal conductivity of air
k_{eff}	Effective thermal conductivity of a porous solid bed
k_s	Solids thermal conductivity
n	Constant of the power-law viscosity equation
N_s	Screw speed
P_e	The dimensionless Peclet number
p_g	Dimensionless pressure gradient coefficient
Q	Volumetric flow rate
q_b	Heat flux on the barrel
q_s	Heat flux on the root of the screw
T_1	Barrel temperature set in feed zone(from 2.7D to 12D)
T_2	Barrel temperature set in compression zone(from 12D to 19D)
T_3	Barrel temperature set in metering zone(from 19D to 26D)
V_0	Constant velocity of barrel in the Z direction
V_{bz}	Barrel velocity along the down-channel direction
V_z	Laminar flow velocity in the Z-direction
V_{ave}	Average velocity in the z-direction
W	Screw channel width
y	Dimensionless coefficient of depth
$Y_k(y)$	Eigenfunctions
Z	Axis taken along the length of the unwound screw channel
z	The dimensionless length in the flow direction
Z_{feed}	Length of the feed section of the screw channel

List of Figures

List of Tables

General introduction

Plastics have become the ubiquitous workhorse material of the modern economy, due to the unrivalled functional properties like versatility and imperviousness to water, combining with low unit cost and ease of manufacture. Their usage has increased twenty-fold in the past half-century and is expected to double again in the next 20 years [FOU 16]. Today nearly everyone, everywhere, every day comes into contact with plastic applications: packaging products such as containers and plastic bags, building products including plastic pipes or vinyl cladding, automotive applications with common products such as door carrier module and all kinds of interior applications, and toy/furniture products such as LEGO Bricks and Kartell.

The increasing utility of polymer products is making demands on the polymer processing industry, defined as the "engineering activity concerned with operations carried out on polymeric materials or systems to increase their utility" [BER 58]. Different technologies such as injection molding, extrusion, blow molding, compression and transfer molding have rapidly developed in recent years, and the corresponding principles of polymer processing are widely studied by a number of researchers. By now, quite mature systems have already been mastered to produce a large amount of plastic products.

In spite of the significant improvements in polymer processing control over the last few decades, quality issues in plastic products, such as color streaking, burn marks and surface/internal cracks, still take place and range from minor surface defects to more serious structural problems that can affect the safety, performance and function of the product. Plenty of room for expensive errors still exists when it comes to polymer processing. The quality instability and controllability of the current plastic products are still an everyday issue and are becoming more apparent by the day as a higher requirement of product quality.

The project SAPRISTI (Autocorrective System for the PRoduction of zero defects In plaSTIcs), in which this thesis work was undertaken, aims to develop an auto-corrective injection molding system for the plastic production based on the control of products. The objectives of this project are multiple: (1) The control of the variability of material; (2) Automatic quality control of produced parts; (3) The diagnosis of the injection method anomaly detection; (4) Self-correction of quality drifts; (5) Demonstration of the performance of the self-correcting system on industrial parts.

To better achieve these different goals, SAPRISTI has brought together several industrial and academic partners. On the industrial side, there are two major groups of high value-added automotive parts manufacturers POAE and RENAULT, and two manufactur-

ing data-control technology suppliers in the plastics industry SISE and ACSYSTEME; On the other hand, various research teams were selected: IPC (the Technical Center for Plastics and Composites whose work on the control of the injection process is widely recognized on a European scale), and three academic laboratories in the field of plastics: LaMCoS/IMP (INSA-Lyon) and SYMME (Université Savoie Mont Blanc). Most of the partners, such as SYMME, ACSYSTEME and IPC, employed statistical methods with artificial neural network to develop an integral auto-corrective system for the whole process. To supplement, our work utilized the physical methods, based on the current theories and models, to help understand the plastication process step by step.

This work of thesis was mainly conducted at INSA-Lyon (Site de Plasturgie), and largely focused on the thermal homogeneity in single-screw plastication process. Temperature is treated as the most critical parameter (pressure being the second important parameter) in plastics processing [CHA 97], hence, the thermal homogeneity in the polymer processing is of great value to study. Single-screw plastication process, which takes place in injection molding and in extrusion, is extensively used for polymer processing, nearly half of the marketing plastic products have experienced the single-screw plastication process. Plastication is in poor relation to process control because it is rarely sufficiently instrumented and therefore difficult to control. The link between a quality defect on the product and the process parameters of plastication is not yet relevant and robust, or even not recognized at all. Indeed, in the particular case of thermal fluctuations, it is open to discussion that these fluctuations could be convected from the screw tip to the mould cavity during the filling process without much change, due to the low thermal diffusion coefficient of any thermoplastic melt.

Single-screw plastication process has been widely studied by a number of scholars with the experimental study, theoretical development, and computational analysis. Most notably, the "cooling experiment", conducted by Maddock [MAD 59], enlightens the experimental study and theoretical development on the plastication process; The classical three regions melting model, formulated by Tadmor [TAD 66], provide reference for plenty of following models and theories on the plastication process; The first computer-aided software, pioneered by the Western Electric Engineering Research Center team [KLE 68], support the simulation on the pressure profile, the melt temperature profile, residence times and power consumption in the plasticating process, and since then numerous commercial computer simulation packages for extrusion/injection molding have been developed and marketed [TAD 13].

Thermal homogeneity in the plastication process is crucial and thus got a lot of attention in the previous studies. On the one hand, the measuring methods, both intrusive and non-intrusive, have been utilized in the experimental thermal detection. Pujos *et al.* [PUJ 08] used thermocouples installed along the die, in walls, at the borders of the extrusion channel to conduct temperature measurements in unsteady flow, the data was used to validate a new model that determines the temperature profile at the inlet of an extrusion die. Launay *et al.* [LAU 14] were able to assess the influence of the thermal measurement cell on the temperature field, and to record evidence of viscous heating at higher flow rate. Abeykoon *et al.* [ABE 12] assessed both intrusive and non-intrusive measurement meth-

ods by using a piece of equipment installed with five different sensors. Results showed that both wall-mounted thermocouples and IR sensor are not capable of detecting most of the important thermal variations. The thermocouple mesh provides highly accurate and detailed measurements, but itself is not robust enough for the industrial applications and is intrusive. On the other hand, the influence factors of thermal homogeneity have been also reported. VeraSorroche *et al.* [VER 14] reported the melt temperature is sensitive to polymer rheological property, screw geometry, and screw speed. Abeykoon *et al.* [ABE 16b] presented that thermal fluctuations highly varied on the barrel set temperature and screw speed. And the radial location of the highest melt temperature fluctuation depends particularly on the screw geometry. Moreover, a positive correlation was found between the level of melt temperature fluctuations and the level of energy demand of the heaters.

The first part of this work, Chapter 2, aims at discussing the generations of thermal fluctuations in solid conveying and melt conveying of the plastication process. The effect of solid bed velocity and solid bed voidage on the thermal fluctuations in the solid conveying zone are quantified. Gaspar-Cunha's model [GAS 00] and finite difference method are used to formulate and solve the temperature field profile at the end of the delay zone. An equation [DEE 13] was used to connect the solid bed voidage with the effective thermal conductivity. Besides, the constituent of raw material can be numerous, especially with the addition of some waste recycling. Fluctuations of throughput and peak pressure caused by the changes in the polymer properties are formulated with the simple model developed by Bereaux *et al.* [BÉR 09].

Most of the published experiments and models are focused on the determination of temperature profile and the origin of thermal fluctuations in the plasticating process. In this thesis, the transport of thermal fluctuations in the screw channel is explored. The second part of this work aims at exploring the laminar dispersion behavior of thermal fluctuations in the plastication process. Two types of thermal fluctuations are envisaged: an initial temperature slug field and a transient inlet temperature boundary condition. As illustrated by Fig. 1. An initial temperature slug would be related to the sudden event of some material with a different temperature entering the screw channel, whereas a transient inlet temperature would signal a fluctuation in the plastication parameter settings.

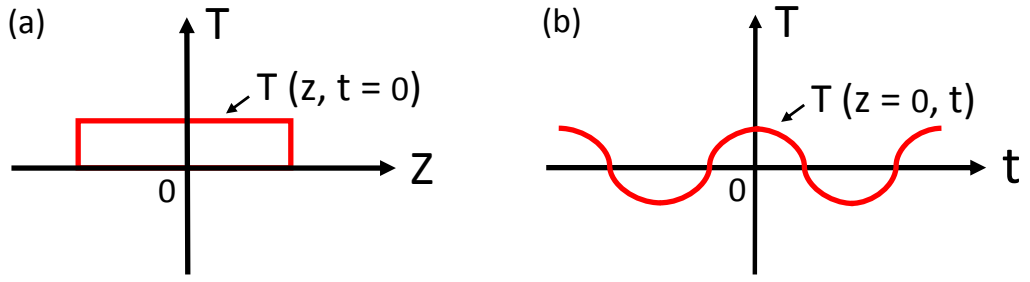

Figure 1: Schematic representation of thermal fluctuations. (a) initial thermal slug; (b) transient inlet temperature boundary condition.

In Chapter 3, the laminar dispersion behavior of initial slug thermal fluctuations in Newtonian fluid and non-Newtonian fluid is investigated analytically and numerically.

A new mathematical model is formulated to study the laminar behavior of a drag and pressure flow of Newtonian fluid between two parallel plates. The results of the mathematical model are compared with the results from the numerical simulation with ANSYS Polyflow, and it founds that a thermal fluctuation can disperse more efficiently in a flow with a back pressure than with a pressure drop. Then, the mathematical model is developed to be used in non-Newtonian fluid, and numerical simulation results present the same conclusion. It gives hints that a higher back pressure can be used to expect a more stable thermal fluid.

In Chapter 4, the laminar dispersion behavior of inlet periodic thermal fluctuations in the polymer melt in the metering zone of the screw channel is studied. The integral transform method is applied to the transient energy conservation equation with the laminar velocity profile obtained for drag and pressure driven flows of a Newtonian fluid. First, the steady state laminar heat transfer problem is solved and extended to the transient case with a periodic single frequency transient inlet temperature. Then the procedure established by Cotta *et al.* [COT 86b] is exactly followed. The steady-state eigenvalues are calculated to build the transient solution. The results reveal the capacity of the drag and pressure flows to dampen inlet temperature disturbances occurring at the beginning of the metering zone of the screw channel. It is found that a higher level of backpressure is indeed improving the thermal homogeneity in the flow. Moreover, for any given flow, the high frequency disturbances are dampened more efficiently than the low frequency disturbances.

The third part of this work focuses on the numerical analysis of a barrel with transparent windows with ANSYS Workbench. A transparent barrel used in injection molding machine was designed and manufactured by Pham *et al.* [PHA 13], which enable the in-line visualization of the plastication process. The transparent glass windows, however, could not endure the working environment for a long time. In Chapter 5, Pham's model of a transparent barrel is simplified and rebuilt with ANSYS DesignModeler. The failure theory of the barrel system is established, the maximum equivalent stress safety tool is used for the steel barrel, and the Mohr-coulomb stress safety tool is used for the glass blocks. Then, the effect of contact type, length of glass windows, temperature, pressure, and material properties on the safety factor of the glass blocks are discussed.

A general conclusion and perspectives of this work will be given at the end of this manuscript.

Chapter 1

State of the art

This chapter contains three main parts, it reviews the previous works on single-screw plastication process, thermal homogeneity in plastication process, and visual barrels for plastication machine. And the objectives of this work are put forward as well.

Contents

Plastication process, defined as the transition of polymer pellets into formable melt along a screw channel in the polymer processing, is a crucial step in injection molding and in extrusion.

Injection molding represents the most important process for mass manufacturing plastic products [FER 14b], which have widespread availability in daily life. Examples include chairs, toys, cases for consumer electronics and disposable cutlery. The raw material can be transformed into a molding in this processing technique and extra finishing operations are not required in most cases. An important benefit of injection molding is the possibility of making intricate and complex geometries automatically in one production step.

Extrusion is another fundamental method for polymer processing. Products can include plastic tubing, pipes, rods, rails, seals, and sheets or films. Extrusion molding has a lower cost relative to other molding processes. This stems, for one part, from the efficiency of the process, and for another part, the reuse of leftover materials, normally discarded as waste in other processes. Another advantage of extrusion is that the plastic remains hot when it leaves the extruder, which allows for post-extrusion manipulation to alter the shape of the extruded plastic to enlarge the flexibility and alterations of the products.

As has been mentioned in the generation introduction, the polymer processing industry is still developing and the products quality problems are still a daily issue to be solved. Hence, the investigation of the thermal homogeneity of the single-screw plastication process is of great value. Up to now, a number of studies have been conducted on this topic. In this chapter, the state of the art of the single-screw plastication process, thermal homogeneity in the plastication process, and visual barrel on injection/extrusion machine are reviewed, and the motivation of the current work are introduced.

1.1 Fundamental of single-screw plastication machines

Plasticating, usually involved in the final stage of many extruded polymer products and also an intermediate stage in injection moulded, blown film, thermoformed, and blow moulded products, occurs inside the screw barrel assembly of the extrusion machine and the injection unit of the injection moulding machine.

The arrangement of basic components of a single screw extruder is illustrated in Fig. 1.1 [ABE 16a]. The electric motor drive unit and the gearbox rotate the screw at a preset speed. The raw material of polymer pellets is fed into the barrel through a hopper. The barrel is enveloped by the heaters and cooling elements, which connected to the control unit to hold the temperature at the predetermined temperatures. The screw is the key component of an extruder and it has been separated by three main geometrical zones, which are the solids conveying zone, melting zone, and metering zone, correspondingly. The ability of the screw and barrel assembly to extrude a given material is dependent on the polymer material properties, the screw and barrel characteristics, and the operating system conditions.

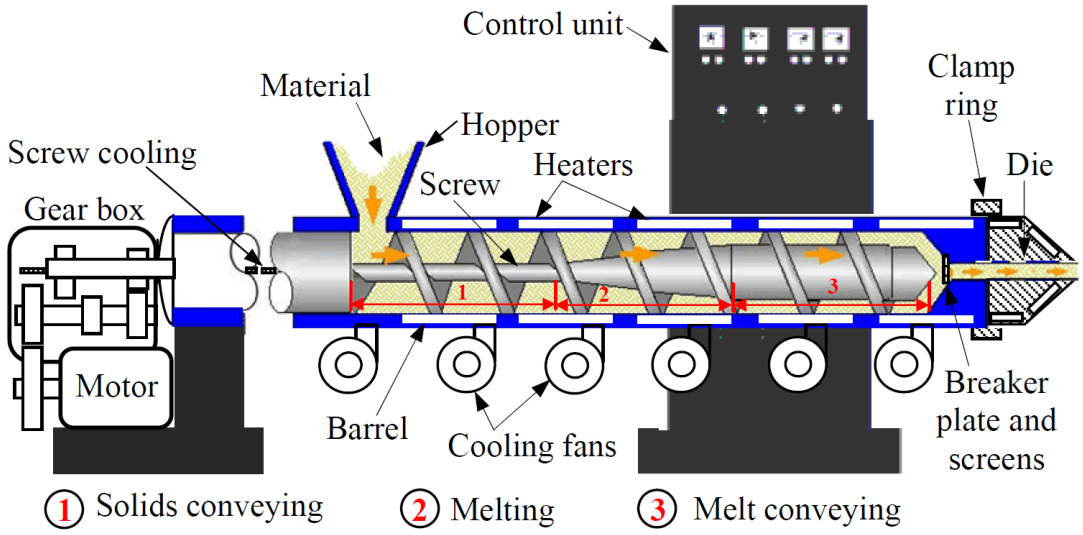

Figure 1.1: Schematic representation of a single screw extruder [ABE 16a].

The injection unit of an injection molding machine, as shown in Fig. 1.2 [FER 18], is similar to an extruder. The main difference lies in the screw operation. A reciprocating screw, which not only rotates but also moves forward/backward, is used in injection molding machine, and acts as a ram in the filling process when the molten polymer is injected into the mold and then retracts backward in the plastication process. Besides, a non-return valve is fitted at the tip of the screw in injection molding machine. The non-return valve allows the melt to flow ahead through this valve while the screw is rotated, while it prevents the melt from slipping back during injection the melt into the mold part.

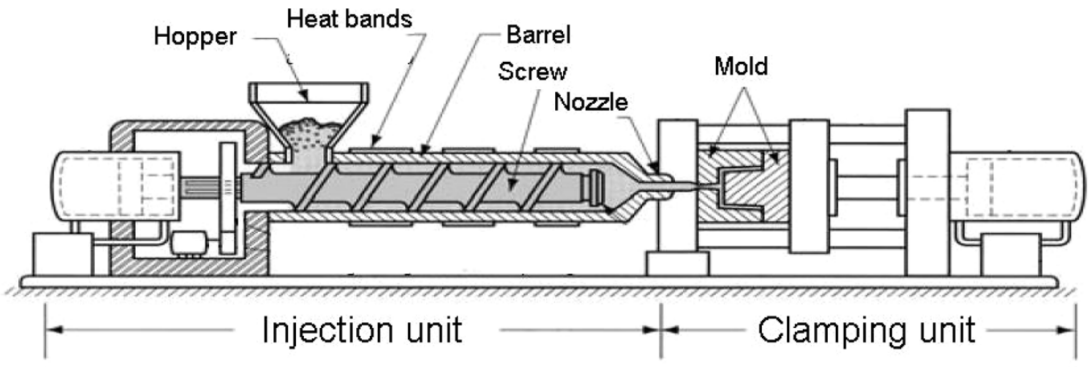

Figure 1.2: Units of an injection-molding machine [FER 18].

1.2 Single-screw plastication process

Single-screw plastication process is widely studied in a multitude of literature. Plenty of experimental studies have been conducted, and mutually completed with the theoretical development. At the same time, various mathematical models have been built to describe the different sections and aspects of plastication process, which can be solved analytically with some simplifications, and also solved numerically in recent decades by applying computer simulation, because of the complexity of the coupled equations of continuity, motion and energy of transport phenomena.

1.2.1 Theoretical development

The main function of the plastication process is to melt and transport the plastics material. The quality of the melt and the plasticating ability of the system determine the production quality and the manufacturing efficiency. A number of research projects have been conducted on the plasticating theory of injection molding machines. At present, the basic theory of injection screw is derived from the theoretical development of extrusion screw, including solid conveying theory, melting theory, and melt conveying theory.

The solid conveying theory is represented by the classical plug flow solid conveying theory: Darnell and Mol [DAR 56] first proposed the solid plug conveying theory in single screw extrusion based on the static balancing of the frictional forces at the screw and barrel surfaces; Chung *et al.* [CHU 70] proposed the viscous drag mechanism, developed in the melt films on the surface of the solid plug; Tedder [TED 71] proposed an energy balance theory. The common point of these classical plug flow theory is that the solid phase material is regarded as a continuous elastic body without deformation, and no relative sliding between the particles, that is, a solid plug. Based on the experimental observation of a visualized extruder, Zhu [ZHU 91] proposed the non-plug solid conveying theory, supplemented the previous solid conveying theory, and improved the accuracy of the theoretical quantitative analysis. Based on this theory, a three-layer model of non-plug flow solid conveying model was further proposed [ZHU 01].

The melting theory studied the mechanism of the melting section, in which the polymer material contains both solid phase and melt phase: Tadmor [TAD 66] first proposed a mathematical model of the Maddock melting mechanism involving three regions: solid bed, melt pool and melt film, as shown in Fig. 1.3 [TAD 70]; Shapiro [SHA 76a] presented a fusion model of melting of granules in a single screw extruder, which is divided into five regions; Yung [YUN 02] considered the injection machine as a reciprocating extruder, and proposed a transient melting model, which gave an explanation for the experimental phenomenon [DON 71a] that melting rate is maximum at the start point of rotating and will decrease till steady state is reached. Besides, the cross-channel flow melting theory was developed with the experimental observation of laminar melt films. Lindt *et al.* [LIN 76] first presented a new melting mechanism, as shown in Fig. 1.4, with a cross-channel flow circulation, a dynamic melting model in a large single screw extruder, which is different from the previous kinematic model of “melting pool”. It was

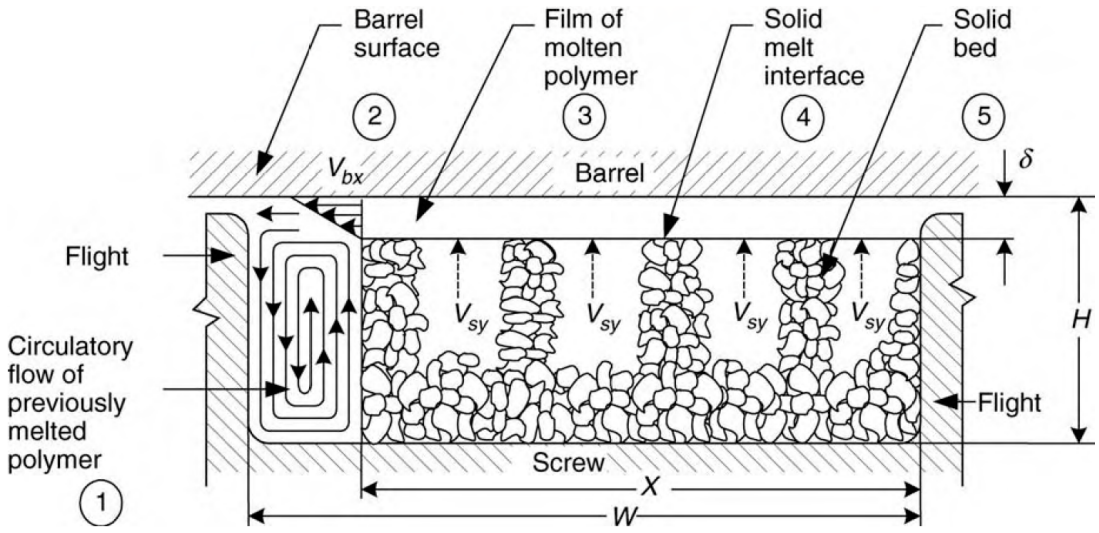

Figure 1.3: Cross-section in the melting zone of a single screw extruder [TAD 70].

combined with a rigid solid bed concept and got a better prediction of the melting rate and axial pressure profile of a non-Newtonian fluid in a large single-screw extruder [LIN 85a]. This type of melting mechanism considers leakage flow through the flight clearance, and more likely to occur in commercial machines. For the situation of cross-channel flow in barrier screw, Elbirli *et al.* [ELB 83] presented that the cross-channel circulation in solids channel is expected to be weak as the barrier-flight clearance being relatively large.

The melt conveying theory is the earliest and most complete theory in the single-screw plastication process. The parameters of the metering section of the screw have long been used to calculate the throughput of the extruder. The earliest melt conveying theory unfolds the screw channel and treats the melt flow as an isothermal Newtonian fluid between two infinitely large parallel plates. It confirms that the flow regime is laminar flow, and the wall is considered to have no slip, indicating that the pressure along the down-channel direction is linearly distributed, i.e., the pressure gradient is constant in the cross-section of the screw channel. At present, the representative melt conveying theory is proposed by Tadmor [TAD 13], and the three-dimensional single-screw melt conveying theory proposed by Zhu *et al.* [ZHU 01].

1.2.2 Experimental study

The plastication process has an important effect on the molding success and is widely studied by a large amount of research groups. A multitude of scholars have carried out a large number of experimental studies on the melt temperature distribution, pressure profile, mixing performance, energy consumption, adaptability and throughput of the single-screw plastication process. The research results helped optimize the design and selection of screw structure and process parameters in actual production.

“Cooling experiment”, an excellent experimental technique to study the plastication

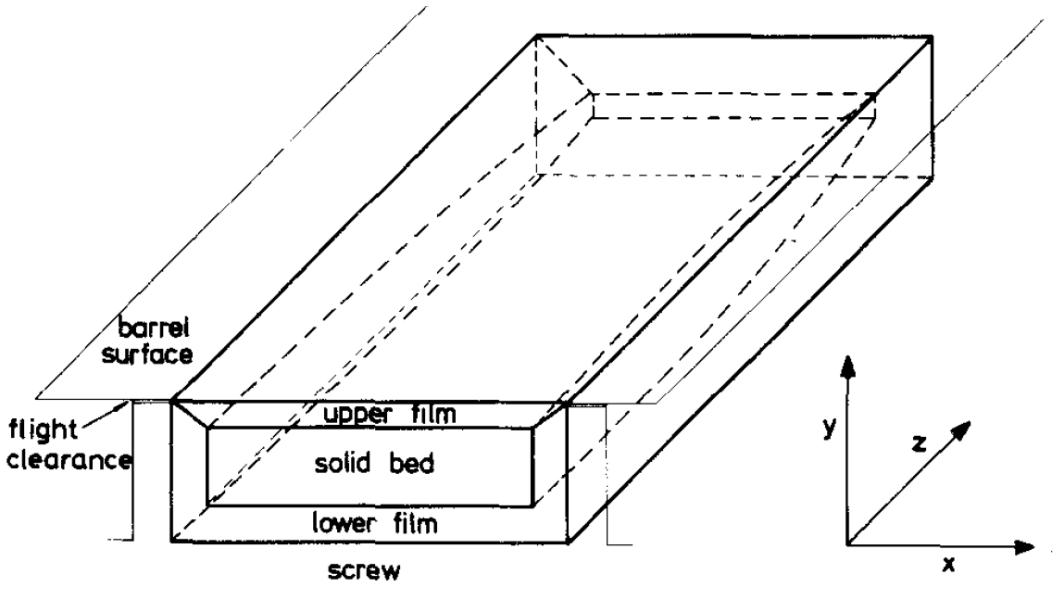

Figure 1.4: Melting mechanism with a cross-channel flow circulation [LIN 76].

process in a single-screw extruder, was first conducted by Maddock [MAD 59]. The main methods of this technique are to suddenly stop the revolving screw and cool down the barrel, then the frozen plastic is taken out together with the screw to observe the polymer melting state along the different part of the screw. By using this method, Tadmor *et al.* [ZEH 67] came up with the famous three-zones melting model, which was then modified and extended to a five-zone model by Sharpiro *et al.* [SHA 76b] and a three-layers model by Lindt *et al.* [LIN 81][LIN 85a].

Single-screw plasticating machine with its barrel embedded with transparent glass, which is called "visual barrel" in this thesis, has been developed by several research groups ([ECC 58][MOH 61][FAN 91][GAO 00][MOG 05][PHA 13]), to promote the understanding of polymer behavior in the plastication process. This system allows the convenient and in-line observation of the dynamic status of polymer inside the injection/extrusion barrel through photography and video recording, and the corresponding material conditions can be further measured via a computerized data acquisition system. The details will be further demonstrated in the following Section 1.4.

Some experiments have been conducted to optimize the screw geometry and operating conditions. For example, Ruberg *et al.* [RUB 08] conducted an experimental study on the energy efficiency of different injection screws. The results present that a new "mixing" injection screw with unique spiral structure has the largest melt delivery volume, most uniform melt temperature and highest energy efficiency, compared with a general-purpose screw, a barrier screw and a new variable barrier screw, which provide suggestions to the optimization of screw design in injection molding.

Many experiments were conducted for the verification of new models ([DON 91][CEL 10][FER 14b][IWK 15][IWK 18]). For example, Fernandes *et al.* [FER 14b] measured the melt temperature in front of the screw nozzle of an injection

molding machine using both an IR camera and an IR thermometer to assess the computational results with a new complex plasticating model, which takes into account the backwards movement of the screw, the presence of a non-return valve and the conduction of heat during the idle times. The effect of barrel set temperatures on the average melt temperature in the injection chamber was studied, as shown in Fig. 1.5, the behavior observed for computational and experimental results is very similar. Besides, the effect of screw speed, backpressure and injection chamber length on the average melt temperature were explored, respectively, and the differences obtained between the results of model and experiments are all below 5%, which validated the plasticating model.

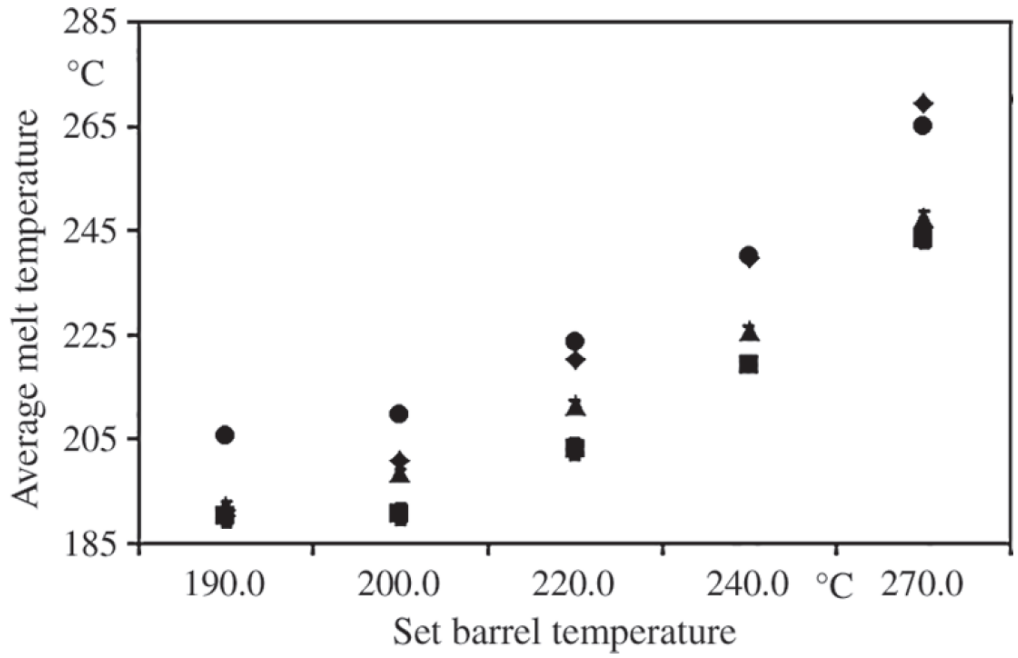

Figure 1.5: Effect of barrel temperatures on the average melt temperature: circle - computation before static phase; diamond - computation after static phase; square - IR thermometer; triangles - IR camera [FER 14b].

A great number of experiments have been conducted by using intrusive or non-intrusive measuring methods to study the temperature distribution and thermal homogeneity of the polymer melt in the plastication process. Plenty of influential and interesting results have been concluded. The details will be further reviewed in Section 1.3.1.

1.2.3 Computational analysis

Although the experimental research can directly reflect the advantages and disadvantages of the performance of the screw barrel assembly, the cost is large, the cycle is time-consuming, and it is difficult to explain the deep plastication mechanism. Therefore, a number of scholars respectively use the modeling calculation and numerical simulation to separate the plastication process, aiming at studying the quantitative relationship between

the processing conditions, including polymer properties, screw geometry and operating conditions, and the processing performance, such as throughput, pressure profile, melt temperature profile, power consumption, residence times and strain, length of the screw required for melting and degree of mixing.

Most of the existing studies on the computational analysis of single-screw plastication are focused on extruders, and many of the studies on the in-line injection process take the simpler course of an extruder [FER 14b]. One of the reasons is that it is more complex to model reciprocating extruders, which changes the process model from steady extrusion to that of a discontinuous process, and considers the transient melting behavior in a reciprocating screw.

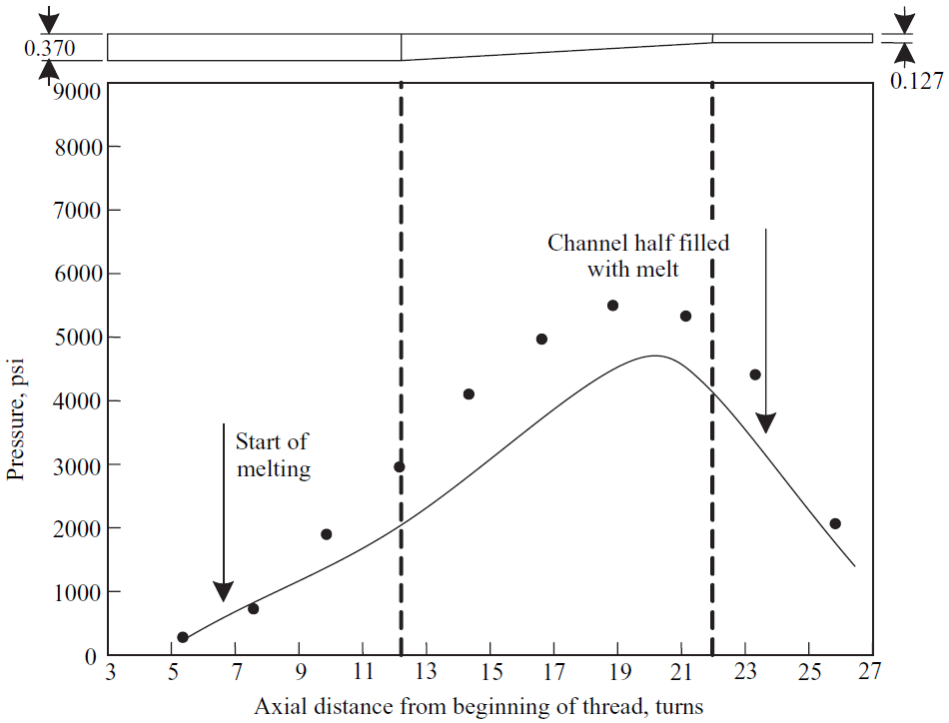

Figure 1.6: Simulated (solid line) and measured (point) pressure profiles for an LDPE extruded in a 2.5-in-diameter, 26.5 length-to-diameter ratio extruder. Simulation was carried out by the first computer simulation package for plasticating extrusion developed by the Western Electric Princeton Engineering Research Center team [KLE 68].

The first computer-aided engineering software package on the simulation of the plasticating extrusion process was pioneered by the Western Electric Engineering Research Center team [KLE 68]. The program is able to simulate the pressure profile along the screw channel, as described in Fig. 1.6 [KLE 68], which indicated that the simulated pressure profile agrees well with the measured one. Besides, the melt temperature profile, residence times and strain, power consumption, power breakdown for the various functions, and expected temperature surging at the die can also be simulated by this program [TAD 13].

Chiruvella [CHI 95] used Finite Difference Method (FDM) to solve the velocity, temperature and pressure fields of a two-dimensional non-isothermal non-Newtonian fluid model of melt flow in the screw channel of a single screw extruder, and solved the matching problem between the extruder and the die with Newton iteration method. The effects of different process conditions, screw geometry parameters and material properties on the plasticating performance were analyzed.

Syrjälä [SYR 97] studied the flow and heat transfer characteristics of fully developed non-Newtonian power-law fluids under the action of the isothermal moving wall in the rectangular screw channel of a extruder, and applied the Finite Element Method (FEM) and the penalty formulation method to solve the governing partial differential equations. The influence of the recirculatory motion set up by the diagonally moving top wall in the cross-section of the screw channel on heat transfer was analyzed.

Gaspar-Cunha [GAS 00] developed a global model of the extrusion process, which adopted numerical models based on finite differences and considered the frictional heat between polymer and screw/barrel surfaces as boundary conditions. The results include the output, melt temperature distribution, power consumption, length of screw required for melting, the degree of mixing, residence time distribution and pressure profile of the plastication process. Besides, the determination of the operational point for a given extruder/die combination is obtained.

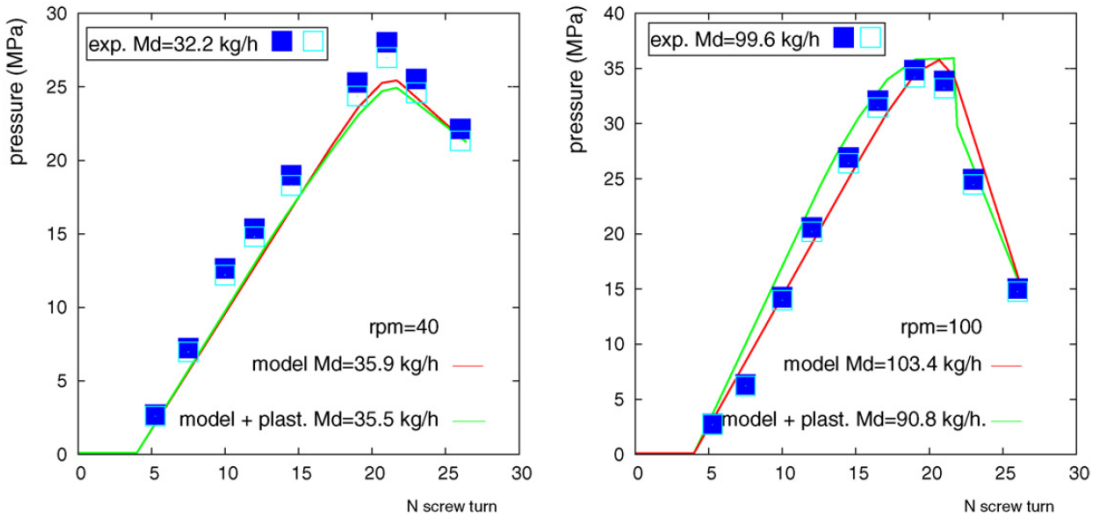

Figure 1.7: Model predictions (with and without plastication included) plotted against experimental data [HAN 90] of pressure along 63.5 mm diameter screw for LDPE at 40 and 100 rpm. [BÉR 09]

Béreaux *et al.* [BÉR 09] developed a simple model to quantify the throughput and peak pressure on the idea of viewing the entire screw as a melt pump. Gauss quadrature formula was used to calculate the pressure gradient along the screw channel. As demonstrated by Fig. 1.7, the model predictions present consistent agreement with experimental data obtained from the literature. The results show that throughput is first and foremost

a function of screw geometry, while pressure development, peak pressure, in particular, is a function of polymer viscosity. Besides, the plastication process is apparent on the pressure profile and throughput only when the plastication length is large.

Buick *et al.* [BUI 06] used the Lattice Boltzmann Method (LBM) to simulate the velocity and stress fields on the cross-section of the screw channel in the mixing section of a screw extruder, and the comparison with Lattice Gas Method (LGM), FDM and theoretical analysis results proved that the LBM simulation method has higher accuracy and computational efficiency. Then, LBM was used for simulation of power-law fluid flow in the mixing section of a single-screw extruder [BUI 09], and the results identified the manner in which the non-Newtonian nature of a fluid changes the flow pattern in the simple geometry considered and highlighted the need to fully consider the non-Newtonian nature of the fluid in such a simulation.

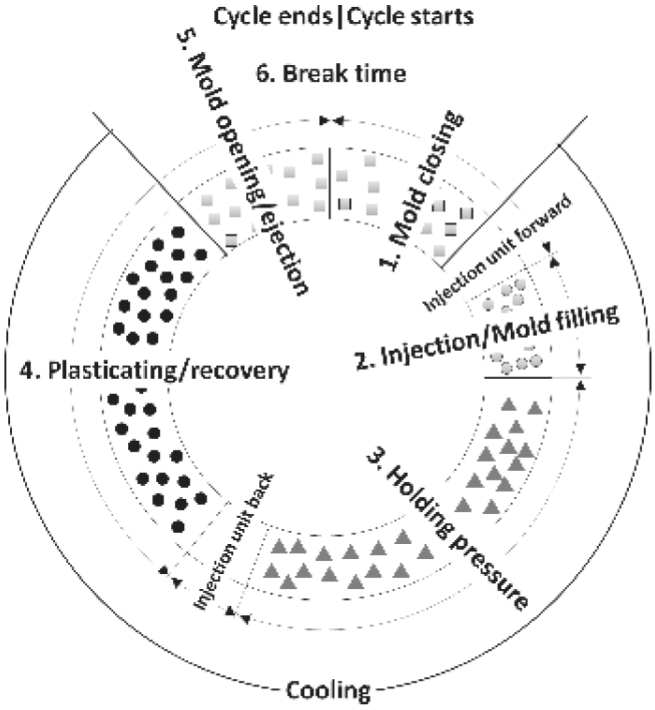

Figure 1.8: Schematic representation of injection molding cycle [FER 14a].

The differences between plastication process in reciprocating injection molding and non-reciprocating extrusion should be recognized. First, the injection cycle can be divided into several steps, as demonstrated in Fig. 1.8 [FER 14a]. The screw performances can have three stages: feeding, in which the screw rotating and moving backwards; idling, during which no screw movement; injecting, in which the screw move forwards without rotation and acts as a ram. Second, axial movements of the screw in reciprocating extruders cause that the solid and melt conveying rates through feeding are reduced, compared with non-reciprocating ones. Third, the time for each stage is limited, and the melting process acts in a transient manner. Consequently, the resultant balance equations for in-

jection are a lot more complicated in comparison with the similar ones for extrusion.

Donovan [DON 74] combined a transient melting model with models for calculating the melt temperature and the pressure profile in the plastication process, to create a plasticating model which serves as an analytical design methodology for the plasticating portion of the injection molding process. Rao [RAO 86] studied the changes in solid bed profile during the injection cycle; Rauwendaal [RAU 92] quantitatively described the solid conveying, melting, and melt conveying in a single screw extruder with both axial and rotational motion of the screw; Yung and Xu [YUN 01] studied the transient models for the melting process at the feeding stages in a reciprocating extruder, identified factors affecting the melting speed; Yung *et al.* [YUN 03] studied the transient models for the melting process in the melting, injection, and stop stages in a reciprocating extruder; Steller and Iwko [STE 08] used a simplified melting model, and solved the equations of energy and momentum analytically, studied the periodical action of the three zones screw, to-and-from screw motion with controlled stroke, and static/dynamic melting. Fernandes *et al.* [FER 14a] developed a new model which takes into account the backwards movement of the screw, the presence of a non-return valve and the conduction of heat during the idle times. Results for the dynamic and static phases of the plastication were presented, respectively.

1.3 Thermal homogeneity in plastication process

In injection moulding or in extrusion, a high level of reliability is usually achieved that makes this process ideally suited to mass market production. Nonetheless, process fluctuations still appear that make moulded part quality control an everyday issue. Whenever some quality problem in the part produced is encountered, the usual response is to incriminate the mould cavity filling stage of the process and to aim at better control of this particular stage by putting pressure sensors inside the mould cavity. Although this is certainly an improvement for reliability by making the process less machine dependent, it is seldom foreseen that the upstream plastication stage could be the source of the fluctuations. Indeed, in the particular case of thermal fluctuations, it is open to discussion that these fluctuations could be convected from the screw tip to the mould cavity during filling without much change, due to the low thermal diffusion coefficient of any thermoplastic melt. Besides, thermal homogeneity in polymer melt has a closed relationship with the energy-consuming efficiency. Therefore, the studies on thermal homogeneity in the plastication process have considerable significance. The state-of-the-art of its measuring methods and influence factors are reviewed in this section.

1.3.1 Measurements of temperature profile

Temperature is treated as the most critical parameter (pressure being the second important parameter) in plastics processing [CHA 97]. Temporal thermal variations may have a large effect on the melt flow, resulting in variations of production rates, non-uniformity of

optical, mechanical, and chemical properties of the extruded parts, even extrudates with un-melted particles, *etc.* [SQU 71][MIA 85]. Therefore, reliable and accurate measurement and suitable mathematical modeling of temperature profile are of great importance for good product quality.

Intrusive measuring methods Intrusive measuring methods have been widely implemented to get the temperature profile in extrusion and injection molding machine, mostly by inserting different kinds of thermocouples, such as conventional thermocouple and auto-traversing thermocouple, into the polymer flow at specific positions.

Amano *et al.* [AMA 88] used a special thermocouple on the nozzle of the injection machine to measure the axial temperature distribution of the screw, and studied the influence of processing conditions, screw configuration and other factors on the temperature distribution.

Esseghir *et al.* [ESS 94] developed a fast-response, cam-driven thermocouple (thermocouple probe can travel in and out of the screw channel driven by a cam) system to measure the temperature profiles in the centerline of the screw channel of a single-screw extruder with various operating conditions of the machine. The effects of viscous dissipation and barrel cooling were observed on the temperature profile. The data obtained indicated the existence of strong cross channel convective heat transfer. The authors stated that the screw speeds still have a limitation and the system needs improvement to allow measurements at more practical speeds.

Pujos *et al.* [PUJ 08] used thermocouples installed along the die, in walls, at the borders of the extrusion channel to conduct temperature measurements in unsteady flow, as illustrated in Fig. 1.9, to determine the temperature profile at the inlet of an extrusion die. Measured temperature data is used to validate a new model that describes flow, heat generation, thermal exchanges, and their coupling by thermal rheological laws.

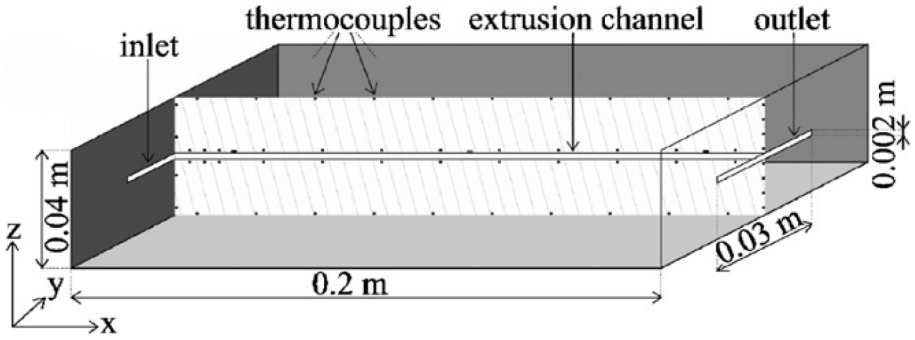

Figure 1.9: Schematic representation of extrusion die [PUJ 08].

Abeykoon *et al.* [ABE 11] used a thermocouple mesh to monitor the die melt temperature profile, a model was generated by the experimental data and could predict the die melt temperature profile. A reduction of up to 60% of melt temperature variations was indicated by the model, which distinctly improved the temperature homogeneity.

Launay *et al.* [LAU 14] developed an experimental device equipped with an innovative intrusive thermal measurement cell, as displayed in Fig. 1.11, its geometry permits

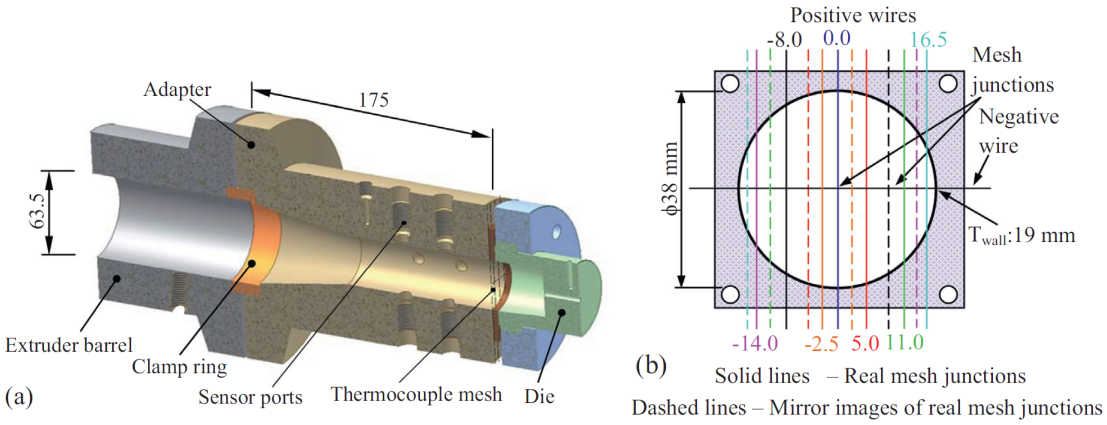

Figure 1.10: (a) The arrangement and the dimensions of the apparatus, (b) the thermocouple mesh arrangement. [ABE 16b]

to avoid the stagnation of the material at the sensor outlet and to reduce the section of the flow. The sensor placed within the cell allows for the measurement of the flow temperature profiles. The influence of the presence of the measurement cell on the temperature field was assessed quantitatively, and evidence of viscous heating and thermal fluctuations at higher flow rate was recorded.

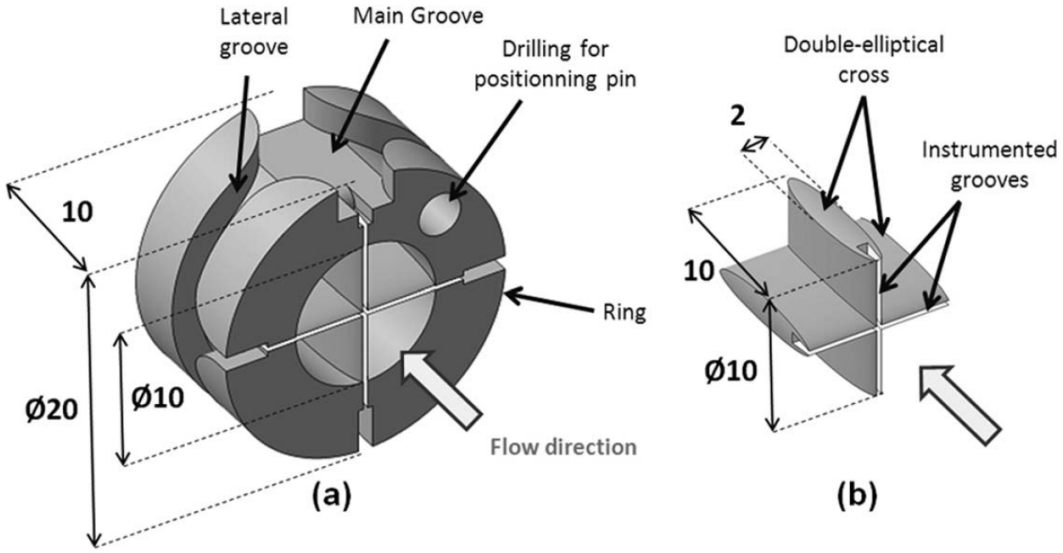

Figure 1.11: Schematic representation of Temperature Measurement Cell, (a) overall view (b) intrusive part (dimensions in mm) [LAU 14].

Non-intrusive measuring methods Non-intrusive measuring methods have been conducted in a number of experiments, as for their advantages compared with the intrusive measuring methods, whose invasive nature affects friction characteristics and heat transfer, and influences the outcome of measured parameters.

Ultrasound velocity method was employed by several scholars. Brown *et al.* [BRO 00] mounted an ultrasonic virtual instrument on industrial scale extruders, by which process data was automated and conducted in real time. Experimental results presented ultrasonic velocity method to be a powerful tool for improving knowledge of polymer melt bulk temperature during extrusion. Muller *et al.* [MÜL 09] created new in-line ultrasonic probes, which apply a buffer rod system with a glassy carbon core material, for monitoring of polymer melts in polymer processing. The ultrasonic attenuation spectra were measured and the content of fillers in polymers in the melt under processing conditions are presented.

Infrared pyrometers/thermometers have been well-documented in a number of publications to measure the temperature of a polymer melt. By detecting the infrared thermal radiation of a molten polymer through a glass window along optical fibers, infrared sensors offer another non-intrusive method of temperature measurement. Most notably, Nietsch *et al.* [NIE 97] presented melt temperature measurements with an infrared thermometer during extrusion and investigated the influence by the surface emissivity and the rotating screw. Dontula *et al.* [DON 91] used infrared sensors to analyze the influence of molding conditions (screw speed, back pressure, injection stroke and road dryness) on the melt temperature distribution, and pointed out that the melt temperature rise, as much as 44°C above the barrel set temperature, was due to the dissipation in the plastication process. Bendada *et al.* [BEN 03] described an on-line infrared method for remote sensing of the surface and the bulk temperatures of a polymer film during injection moulding, which can exhibit low transmission loss of the thermal energy in the mid-and far-infrared, and no end reflection. Besides, a two-wavelength, corresponded to fundamental absorption bands of polyethylene terephthalate (PET), infrared system was developed [BEN 04] for the on-line measurement of the temperature profiles of PET microfibres on an industrial-scale extrusion die. The Near-infrared spectroscopy (NIR) was implemented by Rohe *et al.* [ROH 98]. A transmission sensor was developed for the application of NIR spectroscopy to extrusion processes, at temperatures up to 300°C and pressures up to 35 MPa. An infrared temperature sensor has been used by Vera-Sorroche *et al.* [VER 15] to provide real time quantification of the thermal homogeneity of polymer extrusion at the entrance to the extruder die, the results revealed sensitivity to fluctuations caused by melting instabilities and kept close to bulk melt temperature measured by a complementary technique.

Noriega *et al.* [PIL 04] presented a non-invasive measuring method by using a small quartz window and a rigid boroscope with a fast response time to capture experimental data and images inside an extruder. By sensing the difference in optical properties between the melt and the solid phase, the melting behavior of high density polyethylene was visualized and measured.

A new non-invasive fluorescent measurement sensor, as shown in Fig. 1.12, was created by Bur *et al.* [BUR 04], to measure the temperature profile across the melt flow inside the extruder barrel, i.e., from the screw root to barrel wall. The vertical temperature profiles were obtained as a function of screw speed, screw design and resin melt flow rate, and it was found to be quite flat at low screw speeds with a conventional screw, while became a center-lower line as the screw speed increased. Besides, a large temperature

Figure 1.12: Schematic representation of the confocal optical sensor with micrometer movement [BUR 04].

gradient near the root of the screw was observed, which indicated high shear stress.

Yang *et al.* [YAN 08] reported a new non-invasive technique, electrical capacitance tomography (ECT), to measure the cross section temperature profile in real time in polymer extrusion, through obtaining the permittivity distribution of polymer in a cross-section. The authors present that ECT has several advantages over other measurement methods, such as low cost, fast response, no radiation, non-intrusive, and robust in hostile environments.

In the pre-mentioned work by Abeykoon *et al.* [ABE 12], who measured the temperature profile in extrusion process by using a highly instrumented equipment, which is installed with five different sensors: a non-insulated wall mounted thermocouple, a semi-insulated wall mounted thermocouple, an insulated wall mounted thermocouple, a thermocouple mesh, there was also a Methotrexate IR sensor, as demonstrated in Fig. 1.13. Results showed that the wall mounted thermocouples are poor in capturing process thermal variations, in which the IR sensor performed better. However, both of them are limited to a small volume of the melt flow in where they were fixed, therefore, the authors concluded that point/bulk measurement techniques are not capable of detecting most of these important thermal variations. The thermocouple mesh provides highly accurate and detailed measurements, but itself is not robust enough for the industrial applications and is intrusive.

Even though both the intrusive methods and non-intrusive methods mentioned above have limitations, the temperature profiles along different positions of the screw channel and barrel chamber are quantified. Based on these data, the influence factors of thermal homogeneity in the plastication process could be explored.

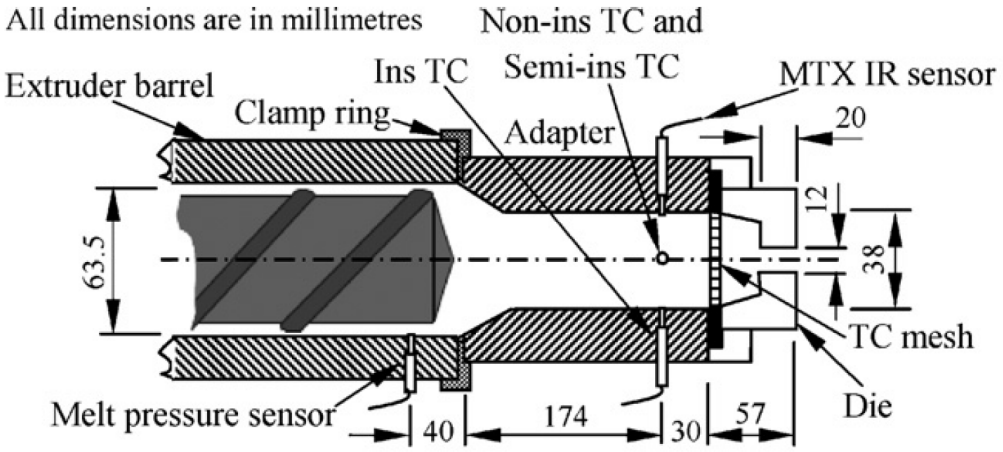

Figure 1.13: Schematic representation of the instrumented equipment. Non-ins TC: non-insulated wall mounted thermocouple; Semi-ins TC: semi-insulated wall mounted thermocouple; Ins TC: insulated wall mounted thermocouple; MTX: Methotrexate IR sensor; TCM: thermocouple mesh. [ABE 12]

1.3.2 Influence factors on thermal homogeneity

Thermal homogeneity has a critical effect on the quality of extrudates and injected products. The influence factors of thermal homogeneity in the plastication process could originate from all of the input parameters, which includes processing materials, screw geometry, and operating conditions. A series of experiments and calculations have been conducted to investigate this problem.

Brown *et al.* [BRO 04] used a higher resolution sensor of electro-welding thermocouple to investigate the influence of screw speeds on the melt temperature at the die section of a single screw extruder. The results showed that at low screw speeds the melt temperature across the flow was flat in shape while it became more pointed at higher screw speeds, and was highest in the center of the flow.

Kelly *et al.* [KEL 06] studied the temperature profile of flowing melts of LDPE at the entrance to a single screw extruder die and concluded that screw geometry has a significant effect on melt temperature profile. Flow melt in a barrier flighted screw provided best melting conditions, especially at higher screw speeds.

VeraSorroche *et al.* [VER 14] reported a number of causes for fluctuations in the temperature field. The melt temperature is found sensitive to polymer type, screw geometry, and set process conditions. Experimental results exhibit that higher levels of thermal fluctuations, which means a lower melt homogeneity, were observed in single flighted screws (both stepped compression screw and tapered compression screw) than barrier flighted screws, as shown in Fig. 1.14 [VER 14]. Besides, thermal fluctuations increased in magnitude with increasing screw speed, which can be explained by a shorter residence time of the polymer inside the extruder barrel. Moreover, due to the differences in rheological

property, melt temperatures for LDPE were lower in all cases and more constant across the channel width than corresponding values for HDPE.

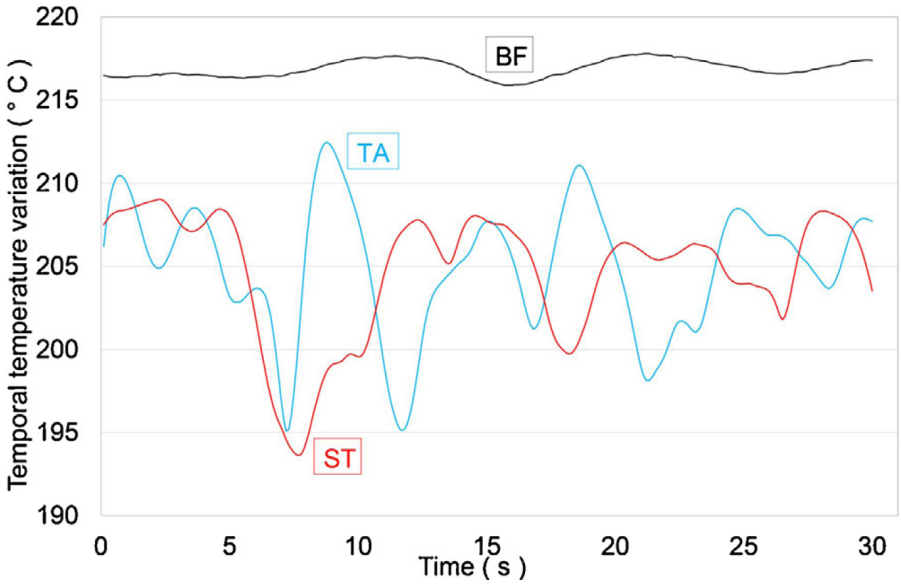

Figure 1.14: Variation of melt temperature for HD6007S at 200°C over a 30 s period at 11 mm from the centre of the flow and screw speed of 70 rpm. ST: stepped compression screw; TA: tapered compression acrew; BF: barrier flighted screw([VER 14].

Abeykoon *et al.* [ABE 16b] provided new insights in a wide range on melt thermal homogeneity in polymer extrusion. The results showed that thermal fluctuations highly varied on the processing conditions, such as barrel set temperature and screw speed. And the radial location of the highest melt temperature fluctuation across the melt flow depends particularly on the screw geometry. Moreover, the level of melt temperature fluctuations was found to relate to the level of energy demand of the heaters, which the higher the energy demand of the heaters the higher the melt thermal fluctuations.

In this thesis, the generation of thermal fluctuations in solid bed conveying and melt conveying zone of the plastication process are explored from a modeling stand-point. The effect of solid bed velocity and solid bed voidage on the thermal fluctuations are revealed quantitatively. Moreover, the influence of polymer properties on the fluctuations of throughput and peak pressure is studied. The details will be presented in Chapter 2.

From the literature reviewed above, we know that the temperature profile in the plastication process can be measured with variety of methods, and the influence factors of thermal homogeneity are also widely discussed. In other words, the thermal fluctuations in the plastication process have been detected and their origins are analyzed, however, few researchers have been found to work on the development/disappearance of thermal fluctuations, which here means the dispersion behavior of thermal fluctuations in the plastication process, make it difficult to understand how thermal fluctuations propagate in the screw channel, and whether and how can they effect on the thermal homogeneity of the following process - the molding stage. The heat transfer mechanisms have been ex-

tensively studied in chemical engineering, and in this thesis, we creatively use it in the polymer processing. As the screw channel can be treated as a rectangular cross-section channel with top wall velocity, an initial slug thermal fluctuation and a periodic inlet thermal fluctuation are assumed to take place at the beginning of the metering zone of the screw channel, respectively, to study their dispersion behavior at the end of the metering zone. The details will be demonstrated in Chapter 3 and Chapter 4.

1.4 Visual barrel for single-screw plastication machine

The plastication process has a crucial influence on the energy efficiency and product quality of the injection molding/extrusion. A number of experiments have been conducted as reviewed above, and plenty of theories and conclusions are drawn up to provide a better understanding of the plastication process and operation control. On the one hand, however, the current experiments have their native drawbacks. For example, the famous "cooling experiment" is a time-consuming operation and the material status within the machine cannot be easily visualized [GAO 00]. On the other hand, temperature measurement may not completely reveal the melting mechanism, unless the melting process can be visually observed. Therefore, one of the best ways to study the plastication process is to design a barrel with transparent windows, which is called "visual barrel" in this work, in order to permit an in-line visualization of the polymer status in the barrel through photography or video recording. Besides, by combining with other instruments and materials, like temperature measurement sensors and temperature-sensitive fluorescent dye, the corresponding material conditions can be also measured or determined via a data acquisition system. The design and fabrication of visual barrels for single-screw plastication machine have been conducted by a number of scholars as follows:

Eccher and Valentinotti [ECC 58] used a small transparent extruder sleeve and a transparent viscous fluid cooperated with tracer particles, the results confirmed the shallow-channel theory.

Mohr *et al.* [MOH 61] used a model extruder with a transparent rotating barrel, two cameras were mounted perpendicular to each other and to the barrel axis. Velocities were found by the photography of tracer particles. Data were obtained near the channel center and again confirmed the shallow-channel theory qualitatively.

Choo *et al.* [CHO 80] inserted two concentrically bored Perspex blocks into an extruder barrel to form viewing windows for tracer particles, which provided channel velocity profiles that used for testing and development of a deep-channel model for single screw extruder. The Perspex cylinders measure 30 mm internal diameter by 80 mm long. A Newtonian liquid under isothermal and developed flow conditions was studied. The temperature of barrel and fluid were only brought up to 40°C.

Fang *et al.* [FAN 91] used an extruder with glass windows in its barrel to do experiments and confirmed the validity of non-plug solid conveying theory proposed by themselves. However, the transparent part of the barrel only showed solid conveying stage, which sustains less heat and pressure than the following stages, like the melting process

and melt conveying process.

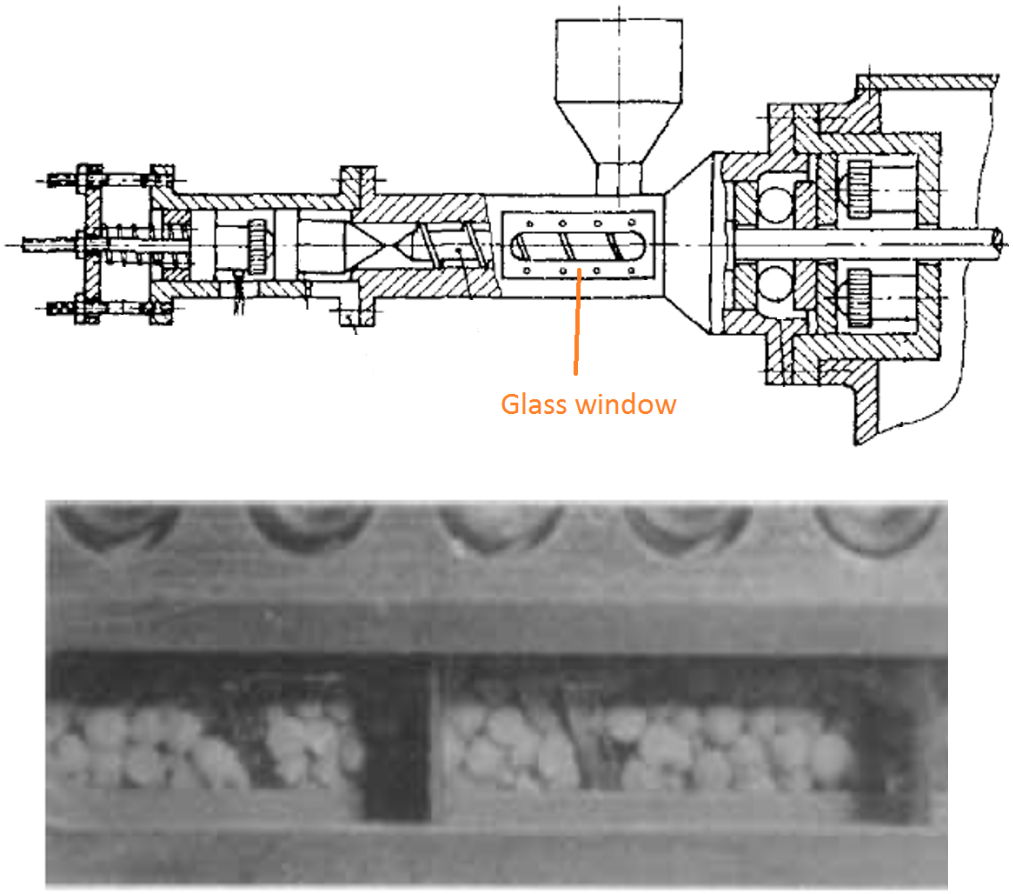

Figure 1.15: Glass window designed by Fang [FAN 91]

Zhu and Chen [ZHU 91] designed an extruder that equipped with 9 glass windows (110 mm in length and 20 mm in width) on both sides of the barrel for the study of the single-screw plastication process. A camera and a video recorder were used for recording the process. The authors claimed that the full process of plasticating extrusion, solid conveying, melting, and melt conveying, can be clearly observed and recorded through the transparent windows. The highest temperature in the record is 180°C.

Campbell *et al.* [CAM 92] conducted a new pump or extruder which allows the barrel, screw helix, and screw core to be rotated independently or in pairs to test the drug flow analysis. The barrel was conducted from a heavy wall glass tube 200 mm long and an inside diameter of 50.3 mm, no temperature field was involved in this study.

A visual barrel system has been developed by Gao *et al.* [GAO 00] to promote the understanding of polymer behavior in a reciprocating screw injection molding machine. This system allows the dynamic status of the polymer inside the injection barrel to be conveniently visualized through photography and video recording. Each glass window is 80 mm in length and 14 mm in width. The 5 glass windows are installed at both the front

and back sides of the barrel, as shown in Fig. 1.16, with the end of one window aligned with the beginning of the next, but only windows 1 to 4 are used. A melting history can be observed, but the melting conveying process is not shown completely. The highest temperature in the record is 200°C. Some photos on plastication process were obtained on injection molding by this equipment. However, the device still has some drawbacks. First, the fifth window was abandoned for a leakage problem. Thus, the melt conveying stage is not visualized. Second, only one camera was used, which lead to a lack of continuous phase transformation of polymer. Finally, the highest temperature in the record is 200°C, which is a little limited for real processing.

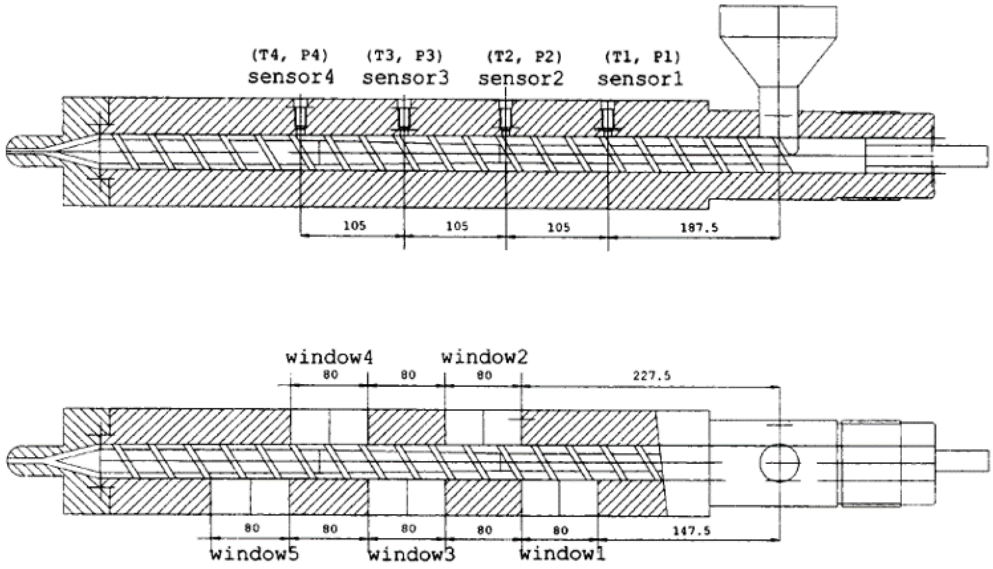

Figure 1.16: Visual barrel designed by Gao [GAO 00]

Moguedet [MOG 05] invented and assembled the "VISIOVIS" visualization tool, which is a fully transparent sleeve in Poly(methyl methacrylate)(PMMA). This instrument was originally designed in the aim of visualizing the 3-dimensional trajectories of a fluorescent particle in a transparent liquid. In recent years, the laboratory has continued to develop this system as original equipment in order to adapt it to the analysis of dispersion (or distribution) of nano-charges in viscous fluids circulating in complex geometry. In this case, it looks like a screw-barrel assembly used in injection molding machines or extruders.

A new barrel with transparent windows used in an industrial-sized injection molding machine was designed and fabricated by Pham [PHA 13] at the laboratory of the "Site de Plasturgie" (University of Lyon), the same place we are now working at. The visual barrel has three glass blocks, each one has one face for lightening and two faces for visualization, record by 3 synchronized cameras and lighting by laser. The 2-D sketch and 3-D view of the barrel are illustrated in Fig. 1.17. This visual barrel is mounted on the "Billion H470-200T" injection molding machine.

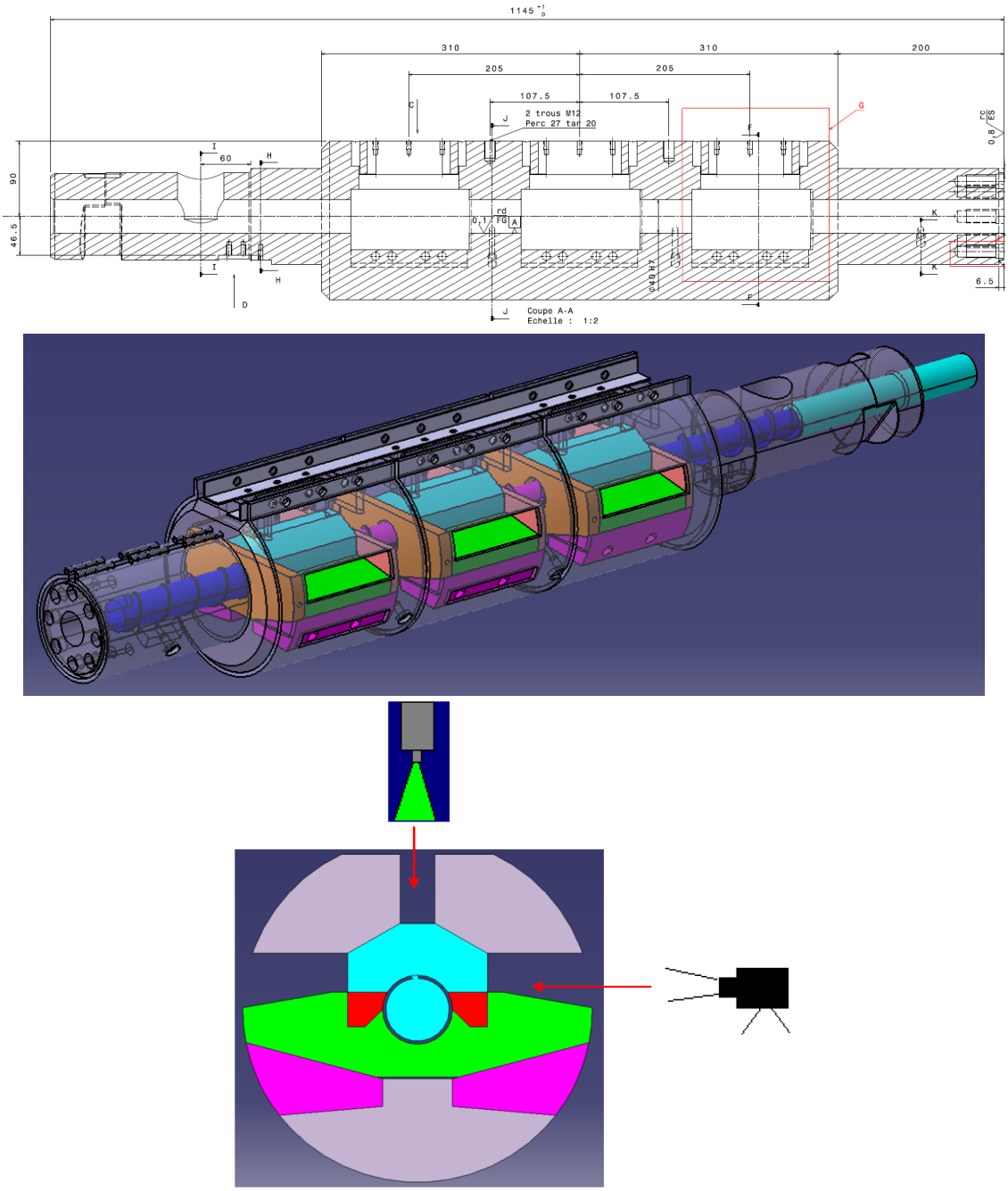

Figure 1.17: Visual barrel designed by Pham [PHA 13]. Top: Sketch of the visual barrel; Middle: 3-D view of the visual barrel; Bottom: Schematic representation of light resource and camera.

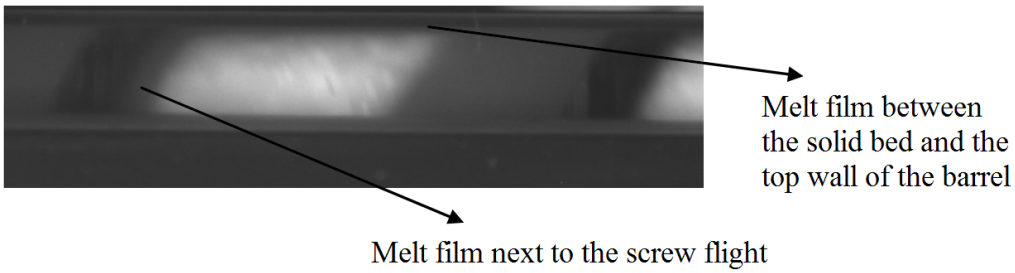

Figure 1.18: Photo of plastication process taken with visual barrel system - the melt film [PHA 13].

Plenty of photos were taken by using this visual barrel system. The results demonstrate the evolution of the solid bed relative to the speed of rotation of the screw, and illustrate the appearance of molten films between the flight of the screw and the solid bed, and between the top wall of the barrel and the solid bed, as shown in Fig. 1.18, which confirm the usual observations of the solid bed in polymer transformation processes. Besides, the results show the appearance of the rupture of the solid bed, as demonstrated in Fig. 1.19, whatever the rotation speed of the screw, and obtain the speed of the solid bed with respect to the speed of the rotation speed of the screw, which could be verified by other experiments.

Figure 1.19: Photo of plastication taken with visual barrel system - solid bed breakage [PHA 13].

By using this visual barrel system, the first reconstructed video from the captured photos in the world of plastics was edited, and it shows what is happening in the screw-barrel system during the injection-molding process.

The optical glass blocks were not robust enough in the common working conditions, however, despite an extremely meticulous and careful procedure for warming up the barrel before any experiment and cooling it down after, cracks were appearing in the glass windows. The reasons for the breakage of the glass windows are still unclear. The failure analysis, with the aim of analyzing the effect of operating conditions on the safety factor of the existing glass windows, was conducted with ANSYS Workbench in Chapter 5.

Chapter 2

Thermal fluctuations generated in solid bed conveying and melt conveying

In this chapter, an investigation is conducted to reveal the effect of solid bed velocity and voidage on the thermal fluctuations. Moreover, the influence of polymer properties on the fluctuations of throughput and peak pressure is studied.

Contents

2.1 Introduction

A high level of reliability is usually achieved that makes the injection molding and extrusion ideally suited to mass market production. Nonetheless, process fluctuations still appear that make molded part quality control an everyday issue.

A number of research groups have taken up the task of detecting and analyzing thermal fluctuations in the plastication process of an extruder or an injection moulding machine. Most notably a temperature measurement cell has been designed and used by [LAU 14] and [VER 14]. Both used a network of thermocouples plunged into the polymer flow and measuring the melt temperature free from the influence of the metallic barrel. Launay *et al.* [LAU 14] were able to assess the influence of the measurement cell on the temperature field, and to record evidence of viscous heating at higher flow rate, while VeraSorroche *et al.* [VER 14] report the effect of polymer type, screw geometry, and processing conditions on the fluctuations in the temperature field.

As the first crucial step in the plastication process, the solid conveying has not received enough attention, due to the difficulties associated namely in considering that the solid bed does not behave as consistent block, as well as in determining some important polymer physical proprieties such as bulk density and coefficients of friction, which depend on process variables like temperature, velocity, and local pressure [GAS 00]. It is open to discussion that the thermal fluctuations generated in solid conveying zone could propagate and influence the whole following process.

Polymer rheological properties, such as viscosity, have been observed experimentally to have a significant effect on thermal homogeneity of the melt [VER 14]. The reason could be that the viscosity, referred to inner friction between molecules, determines the efficiency of the transformation of kinetic energy into internal energy of the fluid. The variation of the polymer properties are larger and much more common with recycled materials, which are increasingly utilized in the practical industry. Therefore, it could be very interesting to investigate the influence of polymer properties on the homogeneity of the plastication process in an analytical method.

In this chapter, fluctuations caused by solid bed and polymer properties in solid conveying and melt conveying process, respectively, are studied. To do this, a brief introduction of the fundamental of plastication principles and operating conditions are given in section 2.2. In section 2.3, the effect of solid bed velocity and solid bed voidage on the thermal fluctuations are studied after solving the temperature field profile with Tadmor's melting mechanism and Gaspar-Cunha's operating conditions. In section 2.4, the effect of polymer rheology properties on the fluctuations of throughput and peak pressure is investigated by using the model formulated by Béreaux *et al.*, which treats the entire screw as a melting pump. The results can be used to have a better understanding of the generation of the thermal fluctuations.

2.2 Plastication principles and operation conditions

2.2.1 Plastication Principles

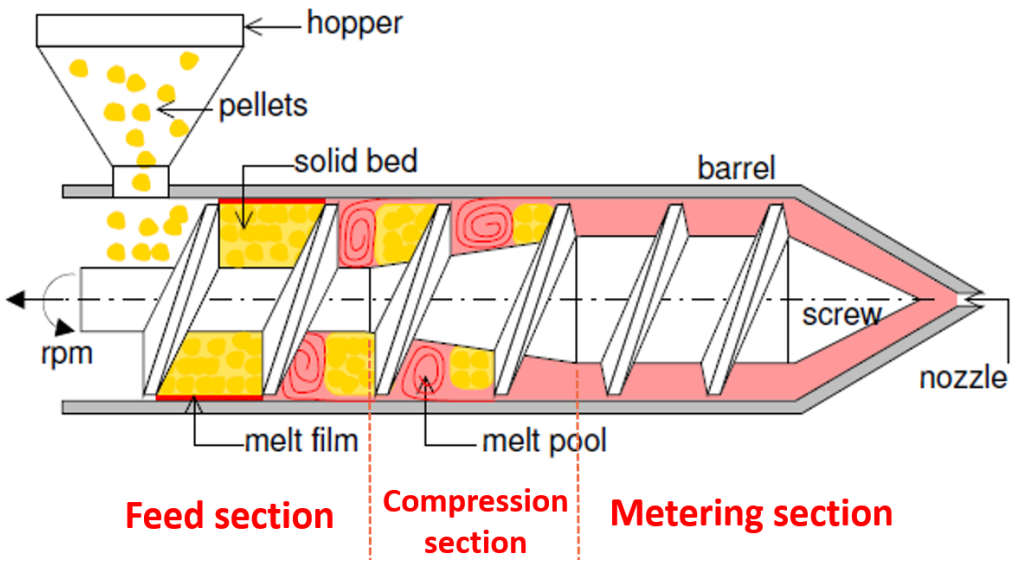

Figure 2.1: Schematic representation of a single screw plasticating extruder. [BÉR 04]

A typical single screw used in injection molding or in extrusion has three geometrical sections: the feed section, the compression section, and the metering section, as shown in Fig. 2.1 [BÉR 04]. The channel depth is constant in the feed section and the metering section, while in the compression section the channel depth changes along the axis. Correspondingly, the classical melting mechanism in plastication process is divided by 4 zones [KAC 72]: the solid bed conveying zone, the delay zone, the melting zone, and the metering zone. A sketch of the plastication process is demonstrated in Fig. 2.2. The 4 distinct zones of plastication in a three sections single screw are listed below:

1. First, in the feed zone of the screw, there is conveying of a solid bed made of compacted pellets. Pressure increases steeply along the screw but cannot reach very high values in a smooth barrel extruder without actually provoking the melting of the superficial layer in contact with the barrel hence releasing any extra-pressure.

2. The next step is called the delay zone whereby the molten film of polymer increases in thickness and possibly permeates the solid bed itself.

3. Proper melting should occur in the compression zone, when the melt film has increased up to a point where it pierces the solid bed to create a melt pool. This melt pool coexists side by side with the solid bed of ever decreasing width.

4. Toward the end of the compression zone and in the metering zone of the screw, the solid bed is completely melted and there is melt conveying solely.

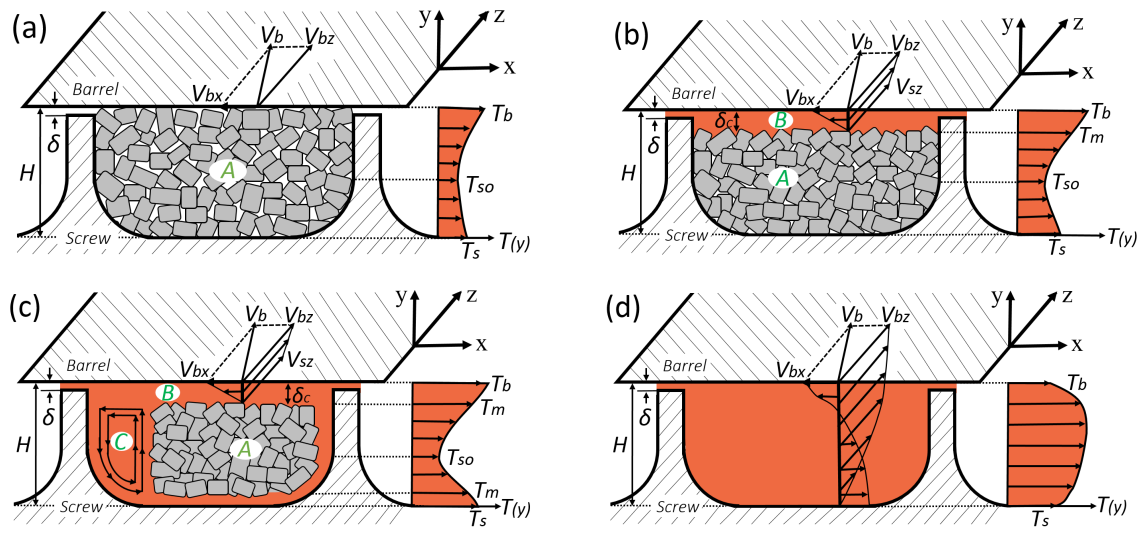

Figure 2.2: Cross-section schematic of plastication process along the screw channel: (a) solid bed conveying zone, (b) delay zone, (c) melting zone, and (d) metering zone. (A)Solid bed, (B) melt film ,(C) melt pool.

2.2.2 Modeling parameters

In this section, the extruder geometry from Gaspar-Cunha's thesis [GAS 00] is used for the modeling of temperature field in the solid conveying process.

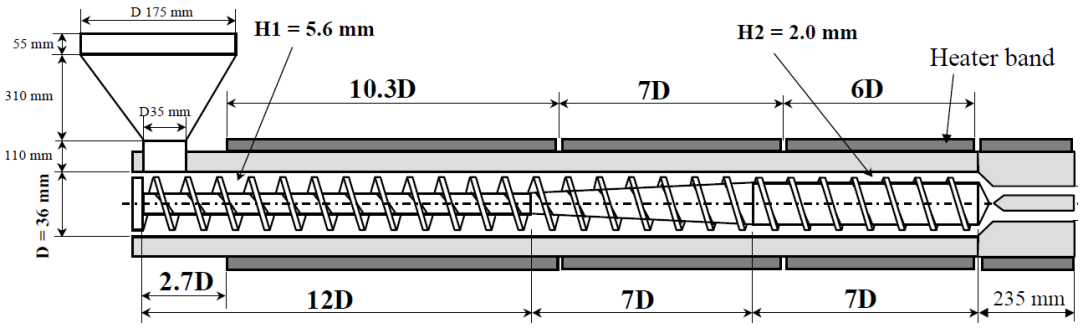

Figure 2.3: Geometry of the extruder used in the modeling of temperature field in solid conveying [GAS 00]

Fig. 2.3 illustrates the configuration of Gaspar-Cunha's extruder. The polymer properties and processing parameters for modeling are given in Table 2.1.

Tableau 2.1: Polymer properties and processing parameters taken from [GAS 00].

HDPE Polymer properties	Values
Power-law consistency, K	3E4 Pa/s^n
Solids thermal conductivity, k_s	0.186 W/(m*°C)
Power-law index, n	0.345
Temperature sensitivity, a	6.8E-3 1/°C
Solid specific heat, C_p	1317 J/kg
Solid density, ρ_s	806 kg/m^3
Melt temperature	119.6 °C
Frictional coefficients	
Polymer-barrel, f_b	0.45
Polymer-screw, f_s	0.25
Operating conditions	
Screw speed, N_s	50 rpm
Temperature set in feed zone(from 2.7D to 12D), T_1	150°C
Temperature set in compression zone(from 12D to 19D), T_2	160°C
Temperature set in metering zone(from 19D to 26D), T_3	170°C
Back pressure	130 bar
Screw geometry	
Internal barrel diameter, D_b	36 mm
External screw diameter, D_s	36 mm
Screw pitch	36 mm
Feed zone depth, H_f	5.6 mm
Metering zone depth, H	2.0 mm
Screw channel width, W	32.4 mm
Screw turns in the feed zone	9.3
Screw turns in the compression zone	7
Screw turns in the metering zone	7

2.3 Solid bed conveying

We looked at what could be the reasons for temperature fluctuations during the solid bed conveying process of the plastication. In this section, a combination of Tadmor's melting mechanism and Gaspar-Cunha's operation parameters [GAS 00] is carried out to compute the temperature field in the solid conveying process. Then, the effect of solid bed velocity and the solid bed voidage on the thermal fluctuations are studied.

2.3.1 Formation of the temperature field

The modeling of the temperature profile in the plastication process was conducted in extensive works. The analytical methods [AGA 96][BRO 72] produce results rapidly but with less accuracy, on account of some crucial assumptions and simplifications are made. Conversely, the finite elements numerical methods [GHO 96][CHA 95][KIM 95] can devise a more persuasive result but with large time consuming problems. Therefore, the finite differences numerical method [ELB 84] [GAS 00] [LIN 85b], by which the computation time is much lower than the finite element method, is treated as a compromise, and get used in this work.

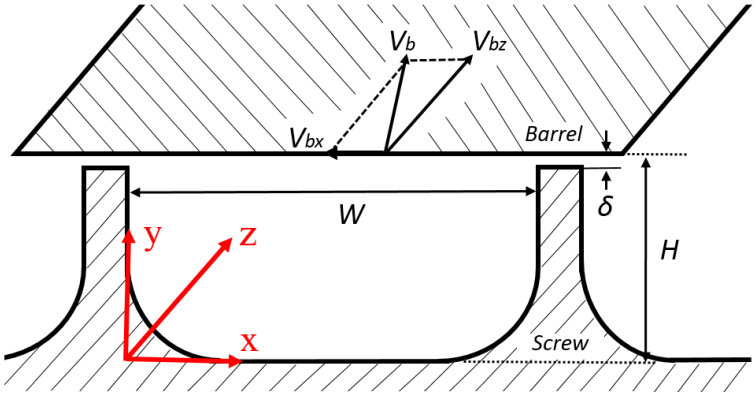

Figure 2.4: Sketch of the barrel-screw configuration.

When modelling this process, it is commonplace to consider a rotating barrel to make part of the plastication stationary, and, because the channel depth is much less than the barrel diameter, to define the screw channel as a rectangular flat channel [TAD 79a][STE 12], so that Cartesian coordinates can be used. Therefore there are three orthogonal directions of interest: the first is down-channel z (along the screw flights), the second is cross-channel x (normal to the flights) and the last one is along the channel depth y, as shown in Fig. 2.4. The origin in y direction is taken at the screw root, while the origin in z direction is under the hopper. The other assumptions and simplifications considered in this section are as follows:

1. The mechanical power dissipated on the flights are neglected;

2. The flight clearance is neglected;

3. The various friction coefficients are constant;

4. Gravitational and inertial forces are neglected.

The advection-diffusion equation is used to describe the temperature profile in the screw channel, as outlined in Eq.(2.1), the left term refers to the thermal advection in z direction, and the right term represents the thermal diffusion in x,y,z directions:

$$\rho_s C_p V_{sz} \frac{\partial T}{\partial z} = k_s \frac{\partial^2 T}{\partial x^2} + k_s \frac{\partial^2 T}{\partial y^2} + k_s \frac{\partial^2 T}{\partial z^2} \tag{2.1}$$

where ρ_s is the solid polymer density, C_p its heat capacity, V_{sz} is the solid bed velocity in the down-channel direction, and k_s its thermal conductivity.

The dimensionless values are given as:

$$\theta' = \frac{T - T_i}{T_w - T_i}, \quad z' = \frac{z}{L}, \quad x' = \frac{x}{W}, \quad y' = \frac{y}{H} \tag{2.2}$$

where L, W, H is the length, width, and depth of the screw channel, respectively, and T_i, T_w is the inlet temperature and wall (barrel) temperature, respectively.

Substituting Eq.(2.2) into Eq.(2.1) yields:

$$\frac{\partial \theta'}{\partial z'} = \frac{1}{G_z}\left(\frac{H^2}{W^2}\frac{\partial^2 \theta'}{\partial x'^2} + \frac{\partial^2 \theta'}{\partial y'^2} + \frac{H^2}{L^2}\frac{\partial^2 \theta'}{\partial z'^2}\right) \tag{2.3}$$

where G_z is the Graetz number, and

$$G_z = \frac{\rho_s C_p V_{sz} H^2}{k_s L} \tag{2.4}$$

Knowing that $H << W << L$, we have $\frac{H}{L} << \frac{H}{W} << 1$, therefore, compared with heat conduction in the radial direction, the other two can be neglected.

Therefore, Eq.(2.1) can be simplified as

$$\rho_s C_p V_{sz} \frac{\partial T}{\partial z} = k_s \frac{\partial^2 T}{\partial y^2} \tag{2.5}$$

The room temperature is used as the inlet condition for the calculation, and the boundary conditions are provided by the friction between the screw root and polymer, the friction between the barrel inner surface and polymer, and the heater wrapped outside of the barrel.

The mechanical power dissipated on the barrel inner surface and on the screw root are formulated by Gaspar-Cunha [GAS 00]. Here a simplified model is used:

$$E_s = \pi N_s D_s f_s W_s P_m Z_{feed} \frac{1}{2} \tag{2.6}$$

$$E_b = \pi N_s D_b f_b W_b P_m Z_{feed} \frac{1}{2} \tag{2.7}$$

where E_s and E_b is the the mechanical power dissipated on the barrel surface, and on the screw root, respectively. N_s is the screw rotation speed; D_s is the external screw diameter; D_b is the internal barrel diameter; f_s is the frictional coefficient between screw and polymer; f_b is the frictional coefficient between barrel and polymer; W_s is the channel width at the root of screw; W_b is the channel width at the barrel surface, which is considered as the same value of W_s; P_m is the pressure ratio cited from Gaspar-Cunha's thesis [GAS 00]; Z_{feed} is the length of the feed section of the screw channel.

Therefore, the heat fluxes through the barrel inner surface and screw root (per unit surface) can be obtained by E_s and E_b divided by the surface where they act, respectively,

$$q_s = \pi N_s D_s f_s P_m \frac{1}{2} \tag{2.8}$$

$$q_b = \pi N_s D_b f_b P_m \frac{1}{2} \tag{2.9}$$

The heat generated at the barrel inner surface is dissipated in both direction of the solids and of the barrel [TAD 79b]:

$$q_b = -k_s \left.\frac{\partial T(y)}{\partial y}\right|_{y=H} + k_b \left.\frac{\partial T(y)}{\partial y}\right|_{barrel} \tag{2.10}$$

where k_b and k_s is the thermal conductivity of the steel barrel and of the solid polymer, respectively.

Imagine that the thermal sensor inside the barrel is at the distance of d' from the interface of the barrel, assume that a linear temperature profile exists in the barrel, the thermal gradient in the barrel can be obtained:

$$\left.\frac{\partial T(y)}{\partial y}\right|_{barrel} \approx \frac{T_b - T}{d'} \tag{2.11}$$

where T_b is the detected barrel temperature value, and T is the barrel interface temperature.

The screw temperature is unknown. To describe the heat flux on the screw surface, the screw is assumed to be adiabatic, then it follows that

$$q_s = k_s \left.\frac{\partial T(y)}{\partial y}\right|_{y=0} \tag{2.12}$$

Fig. 2.5 shows the finite difference grid with lines parallel to the y and z axes. the screw channel is filled with the grid, which means the top line of the grid is the barrel surface, the lowest line is the screw surface, and the most left vertical line is the beginning of the screw channel. The point labeled i, j corresponds to $(z, y) = (z_i, y_j)$, etc. The 4 red points involved in these approximations for an explicit numerical scheme of calculating

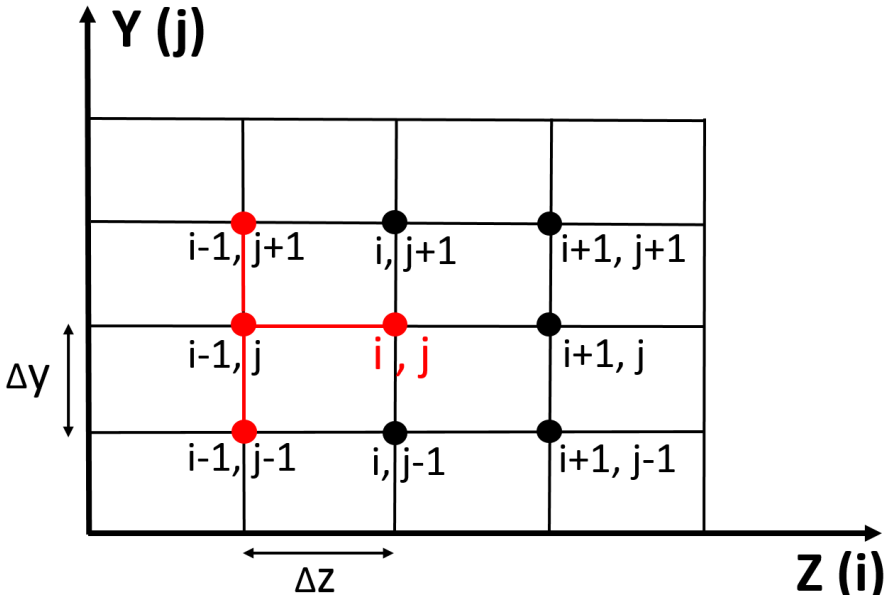

Figure 2.5: Grid for the explicit scheme of finite difference approximations.

the temperature at the point (i, j) are demonstrated. Δy and Δz are the differential elements in the y and z directions, respectively.

The backward difference approximation is used for the first order derivative in the z direction for the discretisation of Eq.(2.5), and the explicit scheme is used for the second order derivatives in the y direction:

$$\left.\frac{\partial T(y)}{\partial z}\right|_{i,j} = \frac{T_{i,j} - T_{i-1,j}}{\Delta z} \tag{2.13}$$

$$\left.\frac{\partial^2 T(y)}{\partial y^2}\right|_{i,j} = \frac{T_{i-1,j-1} - 2T_{i-1,j} + T_{i-1,j+1}}{\Delta y^2} \tag{2.14}$$

Substituting Eqs.(2.13) and (2.14) into Eq.(2.5) yields:

$$\rho_s C_p V_{sz} \frac{T_{i,j} - T_{i-1,j}}{\Delta Z} = k_s \frac{T_{i-1,j-1} - 2T_{i-1,j} + T_{i-1,j+1}}{\Delta y^2} \tag{2.15}$$

Rearrange this equation can we obtain:

$$r\,T_{i-1,j-1} + r'\,T_{i-1,j} + r\,T_{i-1,j+1} = T_{i,j} \tag{2.16}$$

where

$$r = \frac{k_s \Delta z}{\rho_s C_p V_{sz} \Delta y^2} \tag{2.17}$$

$$r' = 1 - 2r \tag{2.18}$$

Eq.(2.16) shows that the temperatures on the right term can be obtained from the temperatures on left term, which could be calculated in the previous step, and the very beginning step is corresponding to the initial temperature for $z = 0(i = 0)$. A matrix is formed with replacing j by 1, 2, ..., N-1:

$$A\,T = B \tag{2.19}$$

where

$$A = \begin{bmatrix} r & r' & r & \dots & 0 & 0 \\ 0 & r & r' & r & \dots & 0 \\ \dots & \dots & \ddots & \ddots & \ddots & \dots \\ 0 & 0 & \dots & r & r' & r \end{bmatrix} \tag{2.20}$$

$$T^T = \begin{bmatrix} T_{i-1,1} & T_{i-1,1} & \dots & T_{i-1,N-1} & T_{i-1,N} \end{bmatrix} \tag{2.21}$$

$$B^T = \begin{bmatrix} T_{i,2} & T_{i,3} & \dots & T_{i,N-2} & T_{i,N-1} \end{bmatrix} \tag{2.22}$$

By solving this matrix, the value of $T_{i,2}$, $T_{i,3}$,...,$T_{i,N-2}$, $T_{i,N-1}$ can be obtained.

The second order of Neumann boundary condition is used to calculate the value of $T_{i,1}$ and $T_{i,N}$. Write Taylor series on the two penultimate points, and neglect the remainder:

$$T_{i,N-1} = T_{i,N} - \Delta y \frac{\partial T(y)}{\partial y}\bigg|_N + \frac{\Delta y^2}{2}\frac{\partial^2 T(y)}{\partial y^2}\bigg|_N \tag{2.23}$$

$$T_{i,N-2} = T_{i,N} - 2\Delta y \frac{\partial T(y)}{\partial y}\bigg|_N + \frac{2^2\Delta y^2}{2}\frac{\partial^2 T(y)}{\partial y^2}\bigg|_N \tag{2.24}$$

Combining the two equations yields:

$$4T_{i,N-1} - T_{i,N-2} = 3T_{i,N} - 2\Delta y \frac{\partial T(y)}{\partial y}\bigg|_{barrel} \tag{2.25}$$

By the same way, it can be obtained:

$$4T_{i,2} - T_{i,3} = 3T_{i,1} - 2\Delta y \frac{\partial T(y)}{\partial y}\bigg|_{y=0} \tag{2.26}$$

Substituting Eq.(2.10) into Eq.(2.25) and Eq.(2.12) into (2.26), the value of $T_{i,1}$ and $T_{i,N-1}$ can be obtained, and then the following line of $T_{i+1,1}$ to $T_{i+1,N}$ can be calculated in the same way, to move forward, the whole temperature field profile along the screw channel can be obtained.

Results of the models are shown in Fig. 2.6. The temperature curve changes with the different length of screw channel and different positions in the height. The green line is at the beginning of the solid bed conveying zone, the boundary conditions of friction heat from both screw and barrel side heat up the polymer pallets and the temperature of the

barrel side is lower because of the cooling system. The blue line gives the temperature profile at the end of solid conveying zone, i.e., the start of the delay zone, we can find that the temperature at the barrel side reaches the melting point. The red line shows the temperature profile at the end of delay zone, i.e., the start of melting zone, we can find the barrel side has already had a melt layer, which is consistent with the plastication theory. The location of these three lines are demonstrated in Fig. 2.7.

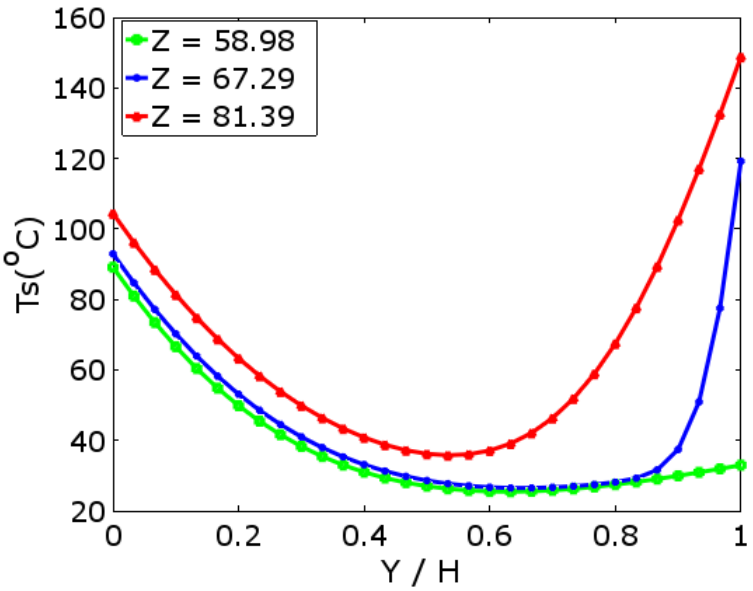

Figure 2.6: Solid bed temperature across the channel at different down-channel location. Solid green line: beginning of solid bed conveying. Solid blue line: end of solid conveying/ start of delay zone. Solid red line: end of delay zone / start of melting. Screw side (Y = 0) and barrel side (Y = 0.056 m).

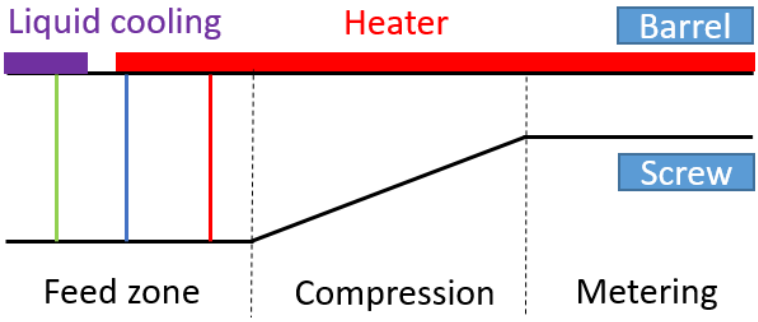

Figure 2.7: Sketch of the unrolled screw channel and the locations of the temperature lines.

2.3.2 The effect of solid bed velocity on thermal fluctuations

In the injection molding process, the reciprocating screw experiences the cycle of injection, holding pressure and rotation backward, which leads to a considerable variation of solid bed velocity. In extrusion, the solid bed deformation and acceleration can also produce a variation of the solid bed velocity [DON 71b]. The effect of solid bed velocity on thermal fluctuations is explored based on the temperature field model formulated in the previous section.

As shown in the Table 2.2, solid bed velocity changes have a large influence on the delay zone lengths and further effect on the plastication lengths. This is because a higher solid bed velocity means a shorter conduction time and therefore a longer plastication length is required to completely melt the polymer. Moreover, temperature field calculations performed with a small change of $\pm 10\%$ on the solid bed velocity resulted in changes of about $\mp$ 3°C in the temperature field at the end of the delay zone. Therefore, fluctuations in the solid bed velocity could well be a source of subsequent temperature fluctuations in the process.

Tableau 2.2: The effect of solid bed velocity on the average temperature at the end of delay zone(T_d).

Velocity	T_d /°C
0.21	72.3
0.27	68.8
0.32	66.3

2.3.3 The effect of solid bed voidage on thermal fluctuations

The solid bed is actually compaction of polymer pellets, with a compaction level depending on the processing parameter and channel geometry. Therefore, it could be viewed as a porous solid, with a varying volume fraction of air in a solid polymer matrix. As achieved in a classic experiment conducted by Scott and Kilgour [SCO 14], the maximum value of random close packing is about 0.637. Thus, the volume fraction of air in the initial solid bed may reach 0.363 or even higher when bridging and lacking of polymer pellets happen. With increasing pressure on the solid bed, the volume fraction of air decreases fast along the screw channel. Therefore, it is relevant to investigate if, by varying the air volume fraction, the conductivity would change enough to change the temperature field significantly, and thus constitutes a potential source of fluctuation.

As a first approximation, the effective thermal conductivity k_{eff} of a porous solid bed with spherical inclusions, in the dilute regime is given by [DEE 13]:

$$k_{\text{eff}} = k_s \left(1 + 3 \frac{k_{\text{air}} - k_s}{k_{\text{air}} + 2k_s} \phi \right) \tag{2.27}$$

where ϕ is the volume fraction of air, k_{air} and k_s are the thermal conductivity of air and the polymer pellets.

Tableau 2.3: Variation of air volume fraction effect on the average temperature at the end of delay zone (T_d).

Voidage	k_{eff} /W/(m°C)	T_d /°C
0	0.19	66.7
0.15	0.15	68.8
0.30	0.12	72.3

As shown in Table 2.3, the variation of the solid bed voidage influences the effective thermal conductivity of the solid bed, and then leads to a thermal fluctuation at the end of the delay zone. When the air volume fraction varies from 0 to 0.3, a higher mean temperature of 5.5°C at the end of the delay zone is calculated. It is not conceivable that such a high volume fraction could occur, therefore we deduce that temperature fluctuations coming from solid bed porosity are much less than this value.

2.4 Melt conveying

2.4.1 Formation of the throughput and peak pressure

Throughput in the conveying zone is the combination of two factors: one is screw rotation which provides a drag flow, the other is the pressure gradient in the screw channel. When the pressure gradient is positive it hinders the drag flow, while it promotes the flow when negative. Throughput is constant along the channel, while pressure development (Fig. 2.8) starts from atmospheric pressure and ends at backpressure imposed on the screw in the case of injection moulding, or at atmospheric pressure at the die exit in the case of extrusion. In extrusion, the level of back pressure is the result of the combination of die and screw, so it cannot be set at will, while in injection moulding it is a freely adjustable processing parameter.

The model used in this work hinges on the idea of viewing the entire screw as a melt pump. By combining the screw geometry, the polymer rheology with the processing parameters, overall operating conditions of the process such as the throughput and peak pressure can be quantified. The assumptions and the equations of the model were previously described by Béreaux *et al.* [BÉR 09] and are briefly presented as follows:

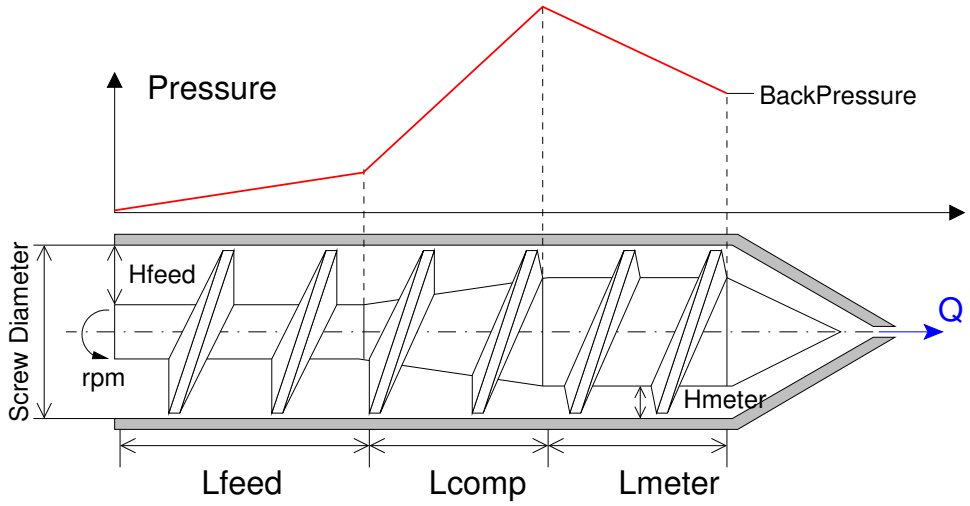

Figure 2.8: Pressure development of standard three zones screw

$$\eta = K\exp[-a(T-T_{\text{ref}})]\,\gamma^{(n-1)} \tag{2.28}$$

$$G = \frac{H^{(n+1)}}{6KV_0{}^n}\frac{\partial P}{\partial Z} \tag{2.29}$$

$$s = \frac{1}{n} \tag{2.30}$$

$$Q = V_0HW\frac{\text{sign}(G)|6G|^s}{(s+1)(s+2)}f(y_0) \tag{2.31}$$

$$f(y_0) = (1-y_0)|1-y_0|^{(s+1)} + y_0|y_0|^{(s+1)} - (s+2)|y_0|^{(s+1)} \tag{2.32}$$

$$0 = |y_0|^{(s+1)} - |1-y_0|^{(s+1)} + \frac{1+s}{|6G|^s\text{sign}(G)} \tag{2.33}$$

where η is the viscosity; K is the consistency factor, which is a function of the barrel temperature T setting along the screw; γ is the shear rate and n is the power-law index; G is a dimensionless pressure gradient in the screw channel, H is the channel depth and V_0 is the constant velocity of barrel in the Z direction, Z is a coordinate taken along the length of the unwound screw channel; $\frac{\partial P}{\partial Z}$ is the local pressure gradient; Q is the throughput, W is the width of the screw channel, y_0 is the dimensionless depth at which the shear rate of flow vanishes.

Depending on the configurations of drag and pressure flow, different velocity (V_z) profiles are available, which generate different values of y_0, as shown in Fig. 2.9.

Eq.(2.28) describes the rheological behavior of a molten polymer in a shear flow at a given temperature, which is the simplest way to take into account the shear thinning properties of thermoplastics materials. The dimensionless pressure gradient G can be given by the local pressure gradient $\frac{\partial P}{\partial Z}$ in Eq.(2.29). The relationship of throughput Q,

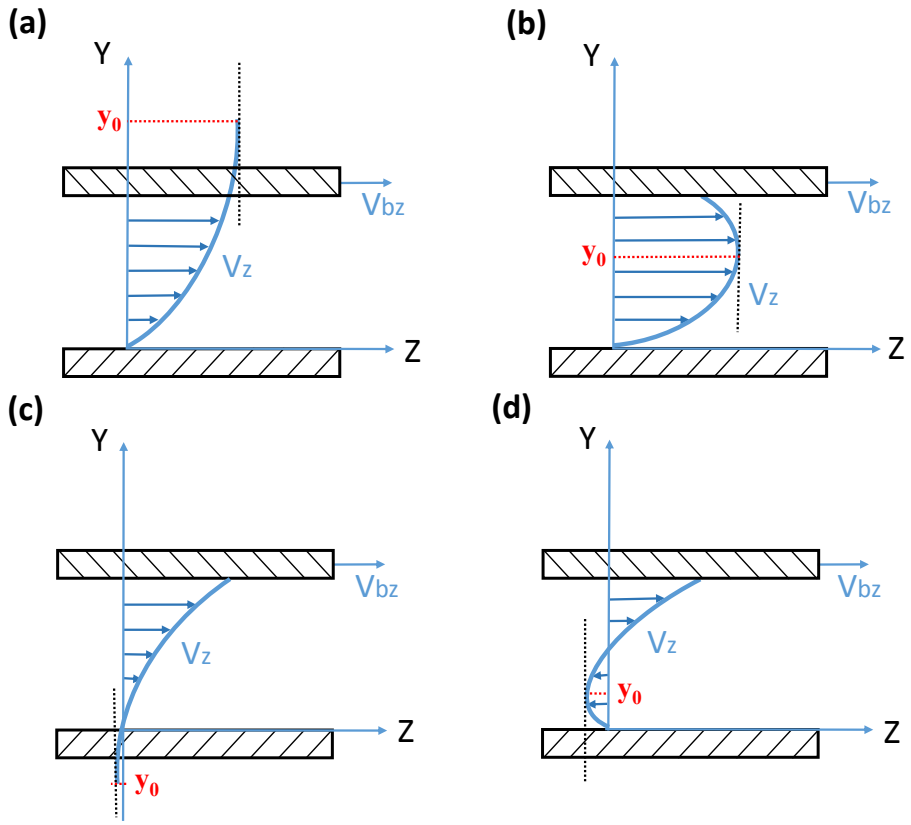

Figure 2.9: The values of y_0 in different flow velocity profiles. (a) and (b) are drag and pressure drop flow with different pressure gradients, (c) and (d) are drag and back pressure flow with different pressure gradients.

pressure gradient G, and parameter y_0 are built by Eqs.(2.31), (2.32) and (2.33). The solutions (Q, G, y_0) of this non-linear system are obtained numerically, which require an iterative procedure with a well-defined starting point. Depending on the sign of the pressure gradient, the parameter y_0 can reach very different values.

A three-step procedure has been designed by Béreaux et al. [BÉR 09] to find a starting point as close as possible to the solution.

(1) A starting flow rate value Q_0 is assigned by the analysis of approximation for closed discharge, whereby the pressure gradient is at its maximum, entirely counteracting the drag flow;

(2) The coefficient of interpolation found in (1) is then applied to estimate the pressure gradient G_0;

(3) An initial guess for parameter y_0 is found as the root of Eq.(2.33) using the preset value of G_0. This finally gives a couple of initial values (G_0, y_0) which can be fed into the full system of equations where Q is also unknown.

The calculation is conducted by using the injection molding machine "Billion 40", the geometry parameters of the screw are listed in Table 2.4. The polymer properties and operating parameters keep the same with the previous section, as shown in Table 2.1.

Tableau 2.4: Screw geometry of the machine Billion 40.

Screw geometry	Values
Internal barrel diameter, D_b	40 mm
External screw diameter, D_s	40 mm
Screw pitch	40 mm
Feed zone depth , H_f	7.0 mm
Metering zone depth, H	2.75 mm
Flight width, W	4.0 mm
Screw turns in the feed zone	10
Screw turns in the compression zone	7
Screw turns in the metering zone	6.5

2.4.2 The effect of polymer properties on thermal fluctuations

By using Béreaux's model and the operating parameters described above, the throughput and pressure profile along the screw channel can be calculated. A 20% variation of the power-law index, flow consistency factor, and activation energy, respectively, of the polymer, is conducted to investigate the fluctuations of throughput and peak pressure, of which the original values are calculated as 8.87 Kg/h and 31.7 MPa, respectively.

Fig. 2.10 displays how variations of polymer rheology (flow consistency factor, shear thinning index and activation energy) could change the throughput and the peak pressure. Clearly, the throughput presents non-neglected fluctuations with the variations of polymer rheology whether through the polymer consistency or the shear thinning index. And the peak pressure near the end of the compression zone is remarkably sensitive to a change in the power-law index, making this variable very interesting for monitoring any variability in polymer material properties in practice. The reason of this phenomenon could be that the viscosity expresses the magnitude of internal friction in a fluid, the improvement of viscosity brings on a stronger connection force or stress between polymer molecules, results to a higher pressure profile. This can also explain some research [WIL 99] that ignored the shear thinning property achieved a systematic overestimate of the pressure prediction. It is worth noting that a 20% change in the consistency is quite modest and could easily happen in the case of recycled material or a change in drying conditions of the material. The polymer HDPE used in this work is not very thermo-dependent, thus the energy activation is expected to have less influence on the fluctuations of both throughput and peak pressure, which corresponding to the results showed in the Fig. 2.10.

According to the law of conservation of mass, the throughput equal to the mass flow rate through the cross-section of each zone of plastication. Therefore, the throughput value Q_t can be related to the solid bed velocity with Eq.(2.34):

$$Q_t = V_{sz} W_s H_f \rho_s \tag{2.34}$$

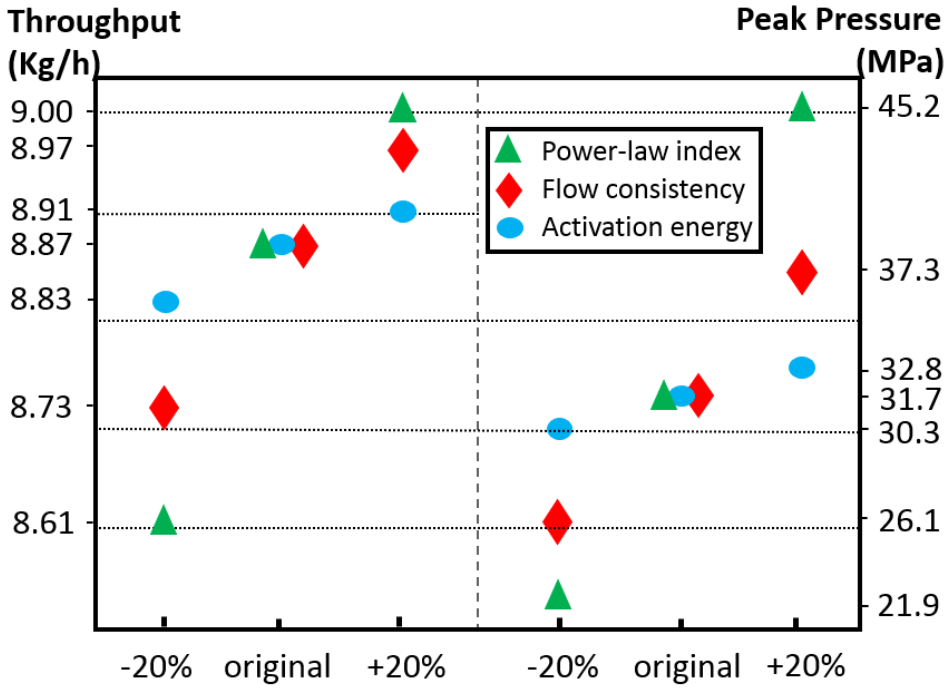

Figure 2.10: The effect of 20% variations of flow consistency, power-law index, and activation energy on the fluctuations of throughput and peak pressure of plastication process

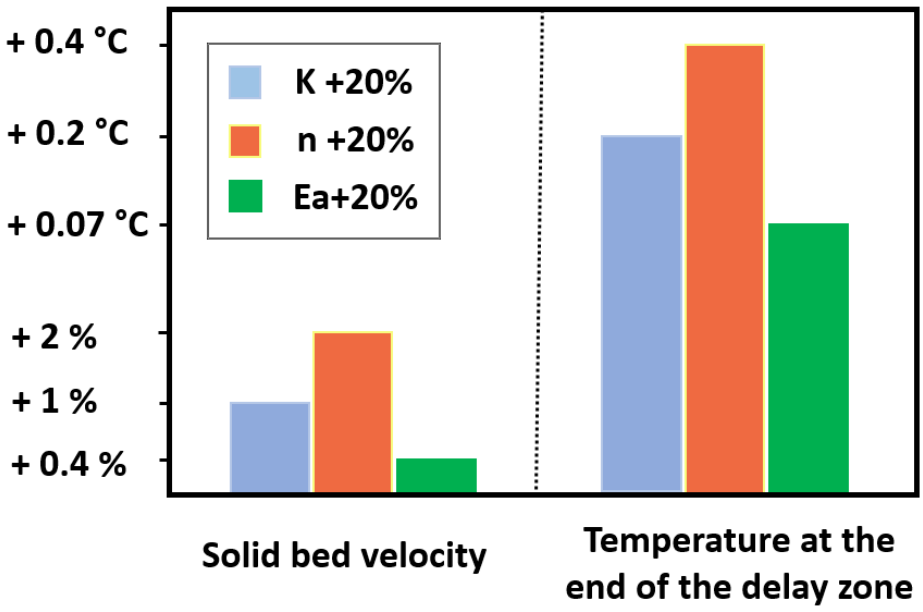

Figure 2.11: The effect of 20% variations of polymer properties on the fluctuations of solid bed velocity, and temperature at the end of the delay zone. K: flow consistency; n: power-law index; E_a: activation energy

Then, the fluctuations of throughput caused by polymer properties can be transferred to the fluctuations of solid bed velocity and the temperature at the end of the delay zone, by using the temperature field profile calculated in the previous section. As shown in Fig. 2.11, with 20% changes of polymer properties, the solid bed velocity and temperature at the end of the delay zone have corresponding variations, and the power-law index has the most responsive influence, which is in agreement with the throughput variations.

The mechanical pressure fluctuations can lead to the thermal fluctuations in the plastication process, if the leakage flow through the clearance between the screw flight and barrel is considered in the practical forming process. The variable pressure could cause the change of flow rate through the clearances. The melt from the former screw pitch has a higher temperature and is heated up again when going through the flight clearances, then lead to thermal fluctuations in the latter screw pitch. Moreover, pressure fluctuations could affect the frictional heat produced by the polymer and surfaces of barrel and screw surface. Therefore, the pressure fluctuations can also be related to temperature fluctuations in the plastication process.

2.5 Conclusions

In this chapter, Tadmor's melting mechanism is combined with Gaspar-Cunha's operating conditions to calculate the temperature field profile in the solid conveying process. Moreover, a simple model of throughput calculation formulated by Béreaux et al. is used to relate the screw geometry, the polymer rheology and the processing parameters to get a good estimate of the mass flow rate and pressure profile along the screw channel. Two factors in solid bed conveying process and three factors of polymer properties in the melt conveying process are drawn up that could cause thermal fluctuations in the plastication process. It can be found that:

(1) A change of $\pm 10\%$ on the solid bed velocity results in changes of about $\mp$ 3°C in the temperature field at the end of the delay zone, which means that fluctuations in the solid bed velocity could well be a source of subsequent temperature fluctuations in the process.

(2) A variation from 0 to 0.3 of the air volume fraction can induce a higher mean temperature of 5.5°C at the end of the delay zone, which gives hint that the variation of solid bed voidage can lead to temperature fluctuations.

(3) Variations of the polymer consistency and power-law index could lead to non-neglected fluctuations of the throughput, which can be further related to the thermal fluctuations.

(4) Small changes in the power-law index could lead to very large changes in the peak pressure. The mechanical pressure fluctuations can also be a source of thermal fluctuations as it influences the frictional heat and leakage flow volume through the screw flight clearances.

Chapter 3

Laminar dispersion of initial thermal fluctuations

In this chapter, the laminar dispersion of initial thermal fluctuations in Newtonian fluid and non-Newtonian fluid are studied analytically and numerically. New models are developed to investigate the laminar dispersion behavior of thermal fluctuations in the metering section of the screw channel, and the influence of slug length and flow pressure to the dispersion behavior are discussed. The results are confirmed numerically with ANSYS Polyflow.

Contents

3.1 Introduction

Laminar dispersion refers to the phenomenon which diffusion is enhanced by flow velocity. Diffusion, characterized by the molecules behaving as "random walkers", is the spreading out of particles that occurs due to the random thermal motion of molecules. In the flow that velocity is uniform everywhere, like plug flow, molecules at different positions of the flow move with the same advection velocity and it is only diffusion flux that differentiates between them. However, the laminar flow in the screw channel, a combination of pressure flow with drag flow, has different flow velocities in different layers, as shown in Fig. 3.1. Diffusion in the direction transverse to the flow makes molecules jump over from one layer to the next, and thereby these molecules can be transported over different distances as the results of the difference in velocities. This smearing out phenomenon generated indirectly from diffusion is here defined as laminar dispersion.

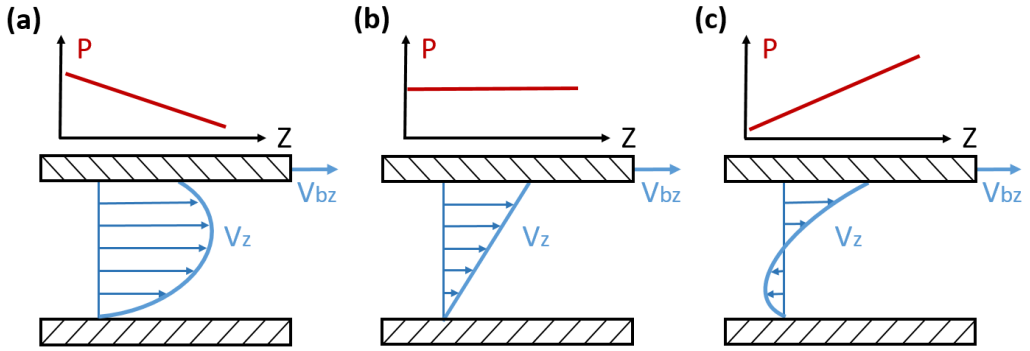

Figure 3.1: Sketch of the three different possible flow configurations: (a) drag and pressure flow, (b) drag flow and (c) drag and backpressure flow.

The dispersion behavior of a soluble matter in flow was investigated in extensive works, following the initial study by Taylor [SIR 53], who studied a nonreactive solute in an incompressible laminar flow through a circular tube by both theory and experiments and proposed an effective dispersion coefficient. Afterward, Gill et al. [GIL 70a] proposed a generalized dispersion with a time-dependent dispersion coefficient that is valid for all time scale. Xu et al. [XU 10] analyzed the effect of thermal dispersion on heat transfer across parallel plates. Diverse situations in a number of subjects are studied with various practical applications, like catheter flow [SAR 04], environmental protection [PIN 15], estuarine mixing [CHA 85], and energy exploitation [DEN 03].

Here in this study, we developed a new model, with drag and pressure laminar flow in a rectangular cross-section channel, to study the dispersion behavior of an initial thermal fluctuation in the metering section of the plastication process. It is found that the average residence time in the metering section L/V_{ave} (L is the length of the metering zone) is about a tenth of the diffusion time scale H^2/D. This is particularly important because it means that this residence time is too short for the dispersion coefficient to reach a steady-state, but too long to be able to neglect radial thermal diffusion and resort to a purely

convective solution. Therefore, the use of Gill's model [GIL 70a], considered a time-dependent dispersion coefficient, for computing the time evolution of the temperature fluctuation, averaged over the channel depth, is relevant.

The polymer melts are assumed for simplicity to be an inelastic liquid in our analysis of the single-screw plastication process, which means that the polymer melt has no memory effect and the stress in the fluid at a given place and time depends only on the deformation rate at that place and time.

3.2 Laminar dispersion of thermal fluctuations in Newtonian fluid

An initial thermal fluctuation is assumed at the beginning of the metering section of the screw channel. The evolution of the thermal fluctuation with dimensionless time at the end of the metering section is studied analytically and numerically in this section. The effect of thermal slug length and pressure in the flow on the dispersion behavior of the thermal fluctuation are discussed. The polymer melt, in this section, is assumed to be a Newtonian fluid.

3.2.1 Mathematical model

In this part, a mathematical model is formulated to study the laminar dispersion of thermal fluctuations in a Newtonian fluid, based on the assumptions mentioned above.

Assume a thermal slug at the beginning of the metering zone, with a length of Z_s and a dimensionless strength of 1, as shown in Fig.3.2.

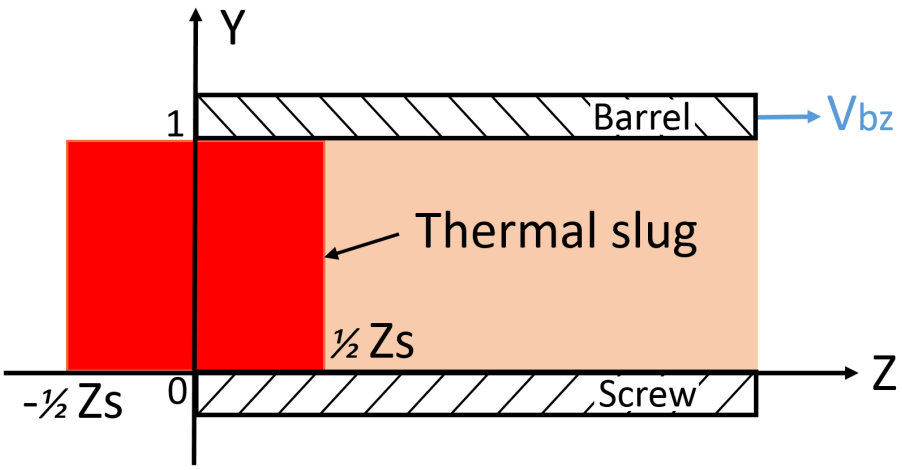

Figure 3.2: Sketch of a thermal slug at the beginning of metering zone.

The volumetric flow rate Q of the drag and pressure flow of a Newtonian fluid through

a rectangular cross-section channel can be described as:

$$Q = -\frac{GWH^3}{12\eta} + \frac{V_{bz}HW}{2} \tag{3.1}$$

where G is pressure gradient along the screw channel, W and H are the channel width and depth in the metering zone, respectively, η is the polymer viscosity as mentioned above, V_{bz} is the barrel velocity along the down-channel direction. Thus, the average velocity V_{ave} in the z-direction can be obtained as

$$V_{ave} = \frac{V_{bz}(3-p_g)}{6} \tag{3.2}$$

where p_g is a dimensionless pressure gradient coefficient,

$$p_g = \frac{GH^2}{2\eta V_{bz}} \tag{3.3}$$

when p_g is zero we have plain drag flow (simple shear or plane Couette flow), while positive value of p_g signals a backpressure flow and negative value of p_g signals a pressure drop flow.

The axial velocity v(y) in the down-channel direction (Z) can be represented as a dimensionless form

$$v(y) = \frac{V_z}{V_{bz}} \tag{3.4}$$

$$v(y) = p_g(y^2 - y) + y \tag{3.5}$$

where y is a dimensionless coefficient of depth, derived from the laminar flow depth Y divided by the channel depth H in the metering zone, and V_z is the corresponding laminar flow velocity in the Z-direction.

The dispersion of a dimensionless temperature fluctuation θ along the channel in the metering zone of a plastication screw could be described with the classic advection/diffusion equation:

$$\frac{\partial\theta}{\partial\tau} + v(y)\frac{\partial\theta}{\partial z} = \frac{1}{{P_e}^2}\frac{\partial^2\theta}{\partial z^2} + \frac{\partial^2\theta}{\partial y^2} \tag{3.6}$$

with boundary conditions:

$$\left.\begin{array}{l} \theta(0,y,z) = 1 \quad (|x| <= \frac{1}{2}z_s) \\ \theta(0,y,z) = 0 \quad (|x| > \frac{1}{2}z_s) \\ \frac{\partial\theta}{\partial y}(t,0,z) = \frac{\partial\theta}{\partial y}(t,1,z) = 0 \end{array}\right\} \tag{3.7}$$

where $v(y)$ is the stationary velocity field from Eq.(3.5), τ is a dimensionless time, z_s is the initial thermal slug length and P_e is the dimensionless Peclet number.

The time scale and length scale for this problem are built on the polymer thermal diffusion coefficient D so that

$$z = \frac{DZ}{H^2 V_{\mathrm{bz}}}, \quad \tau = \frac{Dt}{H^2}, \quad P_e = \frac{HV_{\mathrm{bz}}}{D}, \quad D = \frac{k}{\rho C_p} \tag{3.8}$$

where Z is the length along the down-channel direction and t is the time.

Define a new axial coordinate moving with the average velocity of flow as

$$Z_1 = Z - V_{ave} t \tag{3.9}$$

In dimensionless form, writing

$$z_1 = z - V_{ave}\tau \tag{3.10}$$

Substitution of (3.10) in (3.6) yields

$$\frac{\partial \theta}{\partial \tau} + u(y)\frac{\partial \theta}{\partial z_1} = \frac{1}{{P_e}^2}\frac{\partial^2 \theta}{\partial z_1^2} + \frac{\partial^2 \theta}{\partial y^2} \tag{3.11}$$

where

$$u(y) = v(y) - \frac{3 - p_g}{6} = v(y) - V_{\mathrm{ave}} \tag{3.12}$$

The solution of Eq.3.11 is formulated as a series expansion in $\frac{\partial^k \Theta_m}{\partial z_1^k}$ [GIL 70a]

$$\Theta = \Theta_m + \sum_{k=1}^{\infty} f_k(\tau, y)\frac{\partial^k \Theta_m}{\partial z_1^k} \tag{3.13}$$

where

$$\Theta_m(z_1, \tau) = \int_0^1 \theta dy \tag{3.14}$$

Substituting Eq.(3.13) into Eq.(3.11) yields

$$\frac{\partial \theta_m}{\partial \tau} + u(y)\frac{\partial \theta_m}{\partial z_1} - \frac{1}{{P_e}^2}\frac{\partial^2 \theta_m}{\partial z_1^2} + \sum_{k=1}^{\infty}\Big[\frac{\partial f_k}{\partial \tau}\frac{\partial^k \theta_m}{\partial z_1^k} + f_k\frac{\partial \theta_m}{\partial \tau}\frac{\partial^k \theta_m}{\partial z_1^k}$$

$$+ u(y) f_k \frac{\partial^{k+1}\theta_m}{\partial z_1^{k+1}} - \frac{1}{{P_e}^2} f_k \frac{\partial^{k+2}\theta_m}{\partial z_1^{k+2}} - \frac{\partial^2 f_k}{\partial y^2}\frac{\partial^k \theta_m}{\partial z_1^k}\Big] = 0 \tag{3.15}$$

As mentioned before, the average residence time in the metering section L/V_{ave} (L is the length of the metering zone) is about a tenth of the diffusion time scale H^2/D, which means this residence time is too short for the dispersion coefficient to reach a steady-state, but too long to be able to neglect radial thermal diffusion and resort to a purely convective solution. Therefore, Gill's model [GIL 70a], considered a time-dependent dispersion

coefficient, is adopted in this work. Assume that the generalized dispersion model of the process of distributing Θ_m has a time-dependent dispersion coefficient as

$$\frac{\partial \theta_m}{\partial \tau} = \sum_{i=1}^{\infty} K_i(\tau) \frac{\partial^i \theta_m}{\partial z_1^i} \tag{3.16}$$

Here, we should note that the K_i are functions of τ, even though the velocity field is independent of τ. Besides, we have also

$$\frac{\partial}{\partial \tau}\left(\frac{\partial^k \theta_m}{\partial z_1^k}\right) = \sum_{k=1}^{\infty} K_i(\tau) \frac{\partial^{i+k} \theta_m}{\partial z_1^{i+k}} \tag{3.17}$$

Substitute Eqs.(3.16) and (3.17) into (3.15), and equate the coefficients of $\partial^k \Theta_m / \partial z_1^k$ to zero can yield

$$\frac{\partial f_1}{\partial \tau} = \frac{\partial^2 f_1}{\partial y^2} - K_1 - u(y) \tag{3.18}$$

$$\frac{\partial f_2}{\partial \tau} = \frac{\partial^2 f_2}{\partial y^2} - K_2 + \frac{1}{{P_e}^2} - f_1 K_1 - u(y) f_1 \tag{3.19}$$

...

It can be easily obtained from the initial and boundary conditions on $f_k(\tau, y)$

$$\frac{\partial f_i}{\partial y}(\tau, 0) = \frac{\partial f_i}{\partial y}(\tau, 1) = 0 \tag{3.20}$$

$$f_i(0, y) = 0 \tag{3.21}$$

$$\int_0^1 f_i(y) dy = 0 \tag{3.22}$$

thus

$$\int_0^1 \frac{\partial f_i}{\partial \tau} dy = 0 = \int_0^1 \left[\frac{\partial^2 f_i}{\partial y^2} - K_1 - u(y)\right] dy = K_1 \tag{3.23}$$

$$K_2 = \frac{1}{{P_e}^2} - \int_0^1 u(y) f_1 dy \tag{3.24}$$

To get K_2, we need obtain the value of f_1, which can be seperated by two parts

$$f_1(\tau, y) = f_{1a}(\tau, y) + f_{1b}(y) \tag{3.25}$$

where $f_{1a}(\tau, y)$ is the part that takes the effect of τ and y, and $f_{1b}(y)$ is only the function of y. Substitute (3.25) into (3.18), we can obtain

$$\frac{\partial f_{1a}}{\partial \tau} = \frac{\partial^2 f_{1a}}{\partial y^2} + \frac{\partial^2 f_{1b}}{\partial y^2} - u(y) \tag{3.26}$$

let

$$\frac{\partial^2 f_{1b}}{\partial y^2} - u(y) = 0 \tag{3.27}$$

$$\frac{\partial f_{1a}}{\partial \tau} = \frac{\partial^2 f_{1a}}{\partial y^2} \tag{3.28}$$

By integating Eq.(3.27), and combine with the boundary conditions, it can easily obtain

$$f_{1b} = p_g(\frac{y^4}{12} - \frac{y^3}{6} + \frac{y^2}{12} - \frac{1}{360}) + \frac{y^3}{6} - \frac{y^2}{4} + \frac{1}{24} \tag{3.29}$$

By using a variable separation, f_{1a} can be obtained,

$$f_{1a} = F(\tau)G(y) \tag{3.30}$$

Substituting Eq.(3.30) into Eq.(3.28) yields

$$F'G = FG'' \tag{3.31}$$

let

$$\frac{F'}{F} = \frac{G''}{G} = -{\lambda_n}^2 \tag{3.32}$$

thus

$$F' + {\lambda_n}^2 F = G'' + {\lambda_n}^2 G = 0 \tag{3.33}$$

Finally

$$F = \exp(-{\lambda_n}^2 \tau), \tag{3.34}$$

$$G = A_n \cos(\lambda_n y) + B_n \sin(\lambda_n y) \tag{3.35}$$

The boundary condition gives

$$\frac{\partial f_{1a}}{\partial y}(0) = \frac{\partial f_{1a}}{\partial y}(1) = 0$$

Thus,

$$f_{1a} = \sum_0^\infty A_k \exp[-(k\pi)^2 \tau] \cos(k\pi y) \tag{3.36}$$

From Eq.(3.22), the following equation can be given by:

$$\int_0^1 f_{1a} dy = 0 \quad \text{thus} \quad A_0 = 0 \tag{3.37}$$

$$f_{1a}(\tau, y) = \sum_1^\infty A_k \exp[-(k\pi)^2 \tau] \cos(k\pi y) \tag{3.38}$$

Eq.(3.21) gives $f_1(0,y)=0$, thus

$$\sum_1^\infty A_k \cos(k\pi y) = -f_{1b} = -p_g(\frac{y^4}{12}-\frac{y^3}{6}+\frac{y^2}{12}-\frac{1}{360})+\frac{y^3}{6}-\frac{y^2}{4}+\frac{1}{24} \tag{3.39}$$

Based on

$$\int_0^1 cos(k\pi y)cos(n\pi y)dy = \frac{1}{2}\delta_{kn}$$

, multiply both sides of the Eq.(3.39) by

$$\int_0^1 cos(n\pi y)dy$$

A_k can be expressed by

$$A_k = -2\int_0^1 f_{1b}cos(k\pi y)dy \tag{3.40}$$

To simplify the calculation, let

$$I_1 = \int_0^1 ycos(k\pi y)dy = \frac{(-1)^k}{k^2\pi^2}-\frac{1}{k^2\pi^2} \tag{3.41}$$

$$I_2 = \int_0^1 y^2cos(k\pi y)dy = \frac{2(-1)^k}{k^2\pi^2} \tag{3.42}$$

$$I_3 = \int_0^1 y^3cos(k\pi y)dy = \frac{6+(3k^2\pi^2-6)(-1)^k}{k^4\pi^4} \tag{3.43}$$

$$I_4 = \int_0^1 y^4cos(k\pi y)dy = \frac{(4k^2\pi^2-24)(-1)^k}{k^4\pi^4} \tag{3.44}$$

Thus, it can be obtained

$$A_k = -2\left[\frac{p_g}{12}(I_4-2I_3+I_2)+\frac{1}{6}I_3-\frac{1}{4}I_2\right] \tag{3.45}$$

Substituting Eq.(3.29) and Eq.(3.38) into Eq.(3.25) yields f_1

$$f_1 = \sum_1^\infty A_k \exp(-k^2\pi^2\tau)\cos(k\pi y) + p_g(\frac{y^4}{12}-\frac{y^3}{6}+\frac{y^2}{12}-\frac{1}{360}) + \frac{y^3}{6}-\frac{y^2}{4}+\frac{1}{24} \tag{3.46}$$

To get $K_2(\tau)$, it can be separated as two parts:

$$K_2(\tau) = K_{2a}(\tau)+K_{2\infty} \tag{3.47}$$

where

$$K_{2a}(\tau) = -\int_0^1 u(y) f_{1a} dy = \sum_1^\infty A_k \exp(-k^2\pi^2\tau)[-I_1 - p_g(I_2 - I_1)] \tag{3.48}$$

$$K_{2\infty} = \frac{1}{{P_e}^2} - \int_0^1 u(y) f_{1b}(y) dy = \frac{1}{P_e^2} + \frac{p_g^2}{7560} + \frac{1}{120} \tag{3.49}$$

By calculating A_k, it is easy to notice the value decreases magnitude fast with the increase of k. Therefore, only the first five value from A_1 to A_5 are considered in this calculation:

$$K_{2a}(\tau) = -\sum_{k=1}^{5} A_k \exp[-(k\pi)^2\tau] \int_0^1 u(y)\cos(k\pi y) dy \tag{3.50}$$

Connect Eqs.(3.49) and (3.50), $K_2(\tau)$ can be obtained finally. The similar method can be used to find out $K_3(\tau)$ and higher order dispersion coefficients with analysis of lengthy and awkward integrals. Also, several previous research [GIL 70b] [ANN 79] [ANN 81] [DUT 88] have been mentioned that $K_3(\tau)$ and higher order coefficients decrease in order of magnitude further. Therefore, we only consider the $K_1(\tau)$ and $K_2(\tau)$ in this work. From Eq.(3.23), $K_1(\tau)$ = 0, thus

$$\frac{\partial \theta_m}{\partial \tau} = K_2(\tau) \frac{\partial^2 \theta_m}{\partial z_1^2} \tag{3.51}$$

Since a thermal slug is considered as the initial thermal fluctuation, $\theta_m(\tau, z)$ should satisfy

$$\left.\begin{array}{ll} \theta_m(0, z_1) = 1 & (|z| <= \frac{1}{2} z_s) \\ \theta_m(0, z_1) = 0 & (|z| > \frac{1}{2} z_s) \\ \theta_m(\tau, \infty) = 0 & \end{array}\right\} \tag{3.52}$$

The solution for $\theta_m(\tau, z)$ can be described as

$$\theta_m(\tau, z) = \frac{1}{2}\left[erf(\frac{\frac{1}{2}z_s + z_1}{2\sqrt{\xi}}) + erf(\frac{\frac{1}{2}z_s - z_1}{2\sqrt{\xi}})\right] \tag{3.53}$$

where

$$\xi = \int_0^\tau K_2(r) dr \tag{3.54}$$

Finally, θ_m(3.53) can be plotted by using Matlab.

3.2.2 Results and discussion of the model

It is interesting to get how thermal fluctuations disperse at the end of the metering zone with time, and the effect of different length of thermal slugs on the dispersion behavior. From Fig. 3.3, it can be found that the thermal fluctuations propagate like a non-symmetric parabola with the residence time as a reference axis. It is also easy to find

in the figure that, the peaks of thermal fluctuations presented at the end of the metering section increases with the enhancement of slug length. Besides, with a slug length of 800 dimensionless value, the blue curve begins with a full slug as the half-length of the slug is longer than the metering section, a dimensionless length of 336. This result gives us a hint of the dispersion behavior of thermal fluctuations with infinite length, which can happen in case of changing of processing parameter, like barrel heater temperature.

We choose two different process settings leading to the same throughput and thus to the same average residence time: one with a low screw frequency but a negative pressure gradient corresponding to the left of Fig. 3.1, the other with a higher screw frequency but a positive pressure gradient or backpressure, corresponding to the right of Fig. 3.1. The results are showed in Fig. 3.4, we can notice that the blue curve, with backpressure in the flow, starts earlier and has a lower peak, while the peak of the red curve, with a pressure drop in the flow, has a more clear peak. It shows that a step change in temperature at the beginning of the metering zone is much more efficiently dispersed when backpressure is applied to the flow in the channel.

3.2.3 Numerical simulation with ANSYS Polyflow

The dispersion behavior of thermal fluctuations in the metering zone of the single-screw plastication process was computed with ANSYS Polyflow. Based on Finite Element Method calculations, ANSYS Polyflow is a powerful Computational Fluid Dynamics (CFD) simulation tool for polymer processing within single-screw extruders, predicting the heat and momentum transfer behavior of viscous and viscoelastic fluids. In this work, the results of Section 3.2.1 are compared with the simulation results of Polyflow.

Problem definition and computational domain A 2-D model was created to calculate the dispersion behavior of thermal fluctuations in the screw channel of the metering zone. Based on the screw configuration of "Billion 40"(described in Table 2.4), the value of screw channel depth (H) is treated dimensionless as 1, and the ratio of length and height is set as 400. The dimensionless length of the metering zone of the screw is computed to be 336. Thus, in order to obtain the dispersion behavior of thermal fluctuations at the end of the metering zone, the position at $z = 336$ of this model will be studied.

Mesh resolution In order to combine sufficient precision and acceptable computational time, the mesh has 48 divisions on the height, and 400 divisions along the length. The mesh result is shown in Fig. 3.5.

Material data The polymer melt in the Polyflow simulation is treated as a Newtonian fluid, with a constant viscosity η of 1 with no temperature dependence. The melt density ρ is set dimensionless as 1, and inertia is taken into account for numerical purposes. The flow is assumed to be incompressible. The average temperature is set as a multi-ramp function of Z coordinate, the temperature is set as 1 from 0 to 50 of the coordinate, which is the thermal slug, the temperature of the other part of the coordinate is set as default 0. The coefficient of thermal expansion is set as 0, the thermal conductivity is 1.8222 E-04, the heat capacity per unit mass C_p is set as 1, viscous heating and gravity are neglected. The explanation of setting these dimensionless values in Polyflow simulation and the

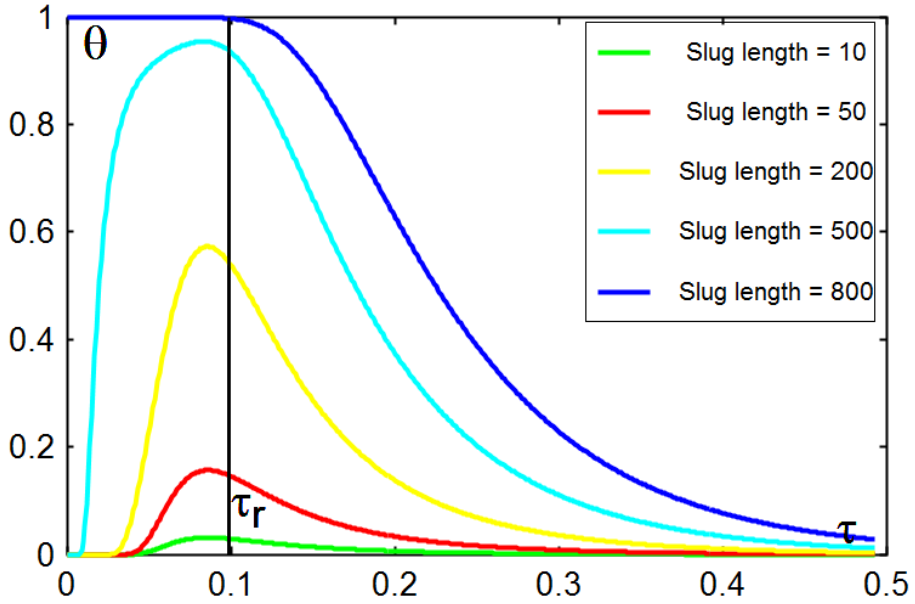

Figure 3.3: Evolution of different slug-length of the temperature fluctuation θ with dimensionless time τ at the end of metering section of a single screw. Time τ_r marks the average residence time from the edge of the thermal slug to the end of metering section.

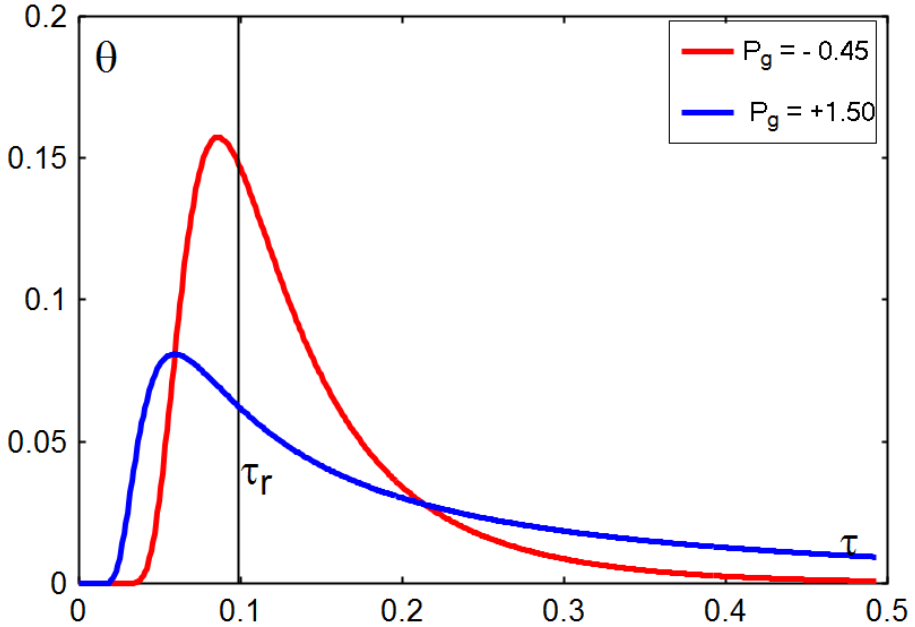

Figure 3.4: Evolution of the temperature fluctuation θ with dimensionless time τ at the end of metering section of a single screw. Time τ_r marks the average residence time. Red curve is when a negative pressure gradient P_g is considered, while blue curve is when a backpressure is considered.

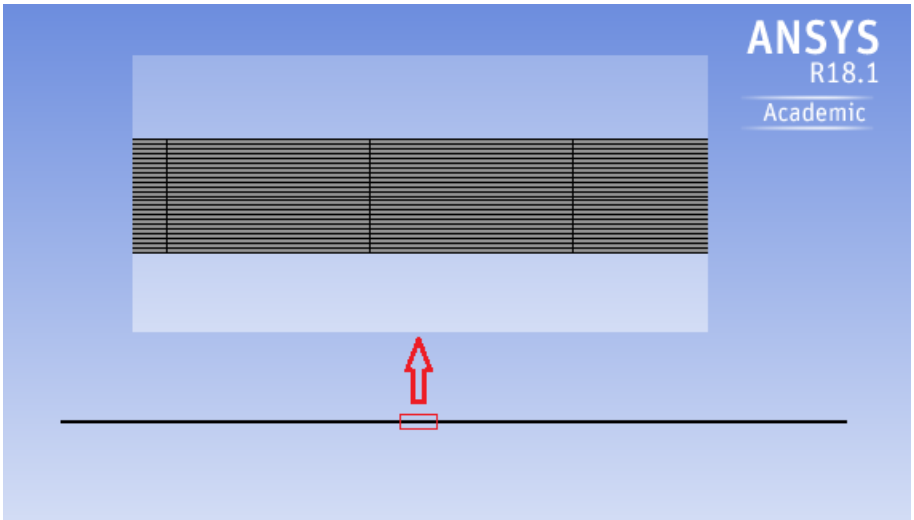

Figure 3.5: Mesh of model in Polyflow

comparison with the dimensionless values in our mathematical model is stated as follows.

In this 2-D model, the advection-diffusion equation can be expressed as

$$\rho C_p \left[\frac{\partial T}{\partial t} + V_z(y)\frac{\partial T}{\partial z}\right] = k\left(\frac{\partial^2 T}{\partial y^2} + \frac{\partial^2 T}{\partial z^2}\right) \tag{3.55}$$

where ρ is the polymer melt density, C_p its heat capacity, k its thermal conductivity, and $V_z(y)$ is the flow velocity in the down-channel direction.

As mentioned before, H (screw channel depth) is set as reference length in all directions, and V_{bz} (barrel velocity in Z direction) as reference velocity. Hence, the reference time is forced to set as t_{ref} = H / V_{bz}. Choosing ΔT as a temperature scale, we have now:

$$\rho C_p \left[\frac{\Delta T}{t_{\text{ref}}}\frac{\partial \theta}{\partial t_{\text{sim}}} + V_{z-sim}(y)V_{bz}\frac{\Delta T}{H}\frac{\partial \theta}{\partial z_{\text{sim}}}\right] = k\left(\frac{\Delta T}{H^2}\frac{\partial^2 T}{\partial y_{\text{sim}}^2} + \frac{\Delta T}{H^2}\frac{\partial^2 T}{\partial z_{\text{sim}}^2}\right) \tag{3.56}$$

Then, it is easy to obtain:

$$\frac{\partial \theta}{\partial t_{\text{sim}}} + V_{z-sim}(y)\frac{\partial \theta}{\partial z_{\text{sim}}} = \frac{k}{\rho C_p H V_{\text{bz}}}\left(\frac{\partial^2 \theta}{\partial y_{\text{sim}}^2} + \frac{\partial^2 \theta}{\partial z_{\text{sim}}^2}\right) = \frac{1}{P_e}\left(\frac{\partial^2 \theta}{\partial y_{\text{sim}}^2} + \frac{\partial^2 \theta}{\partial z_{\text{sim}}^2}\right) \tag{3.57}$$

The corresponding dimensionless material data in Polyflow simulation, therefore, be set as

$$\eta = 1, \quad \rho = 1, \quad C_p = 1, \quad k_{\text{sim}} = \frac{1}{P_e} \tag{3.58}$$

where

$$P_e = \frac{H V_{\text{bz}}}{D}, \quad D = \frac{k}{\rho C_p} \tag{3.59}$$

Now the correspondence between dimensionless variables defined for the numerical simulation with the dimensionless variables defined in the mathematical model, is as follows:

$$\tau = \frac{Dt}{H^2} = \frac{tV_{bz}}{H}\frac{D}{HV_{\mathrm{bz}}} = \frac{t_{\mathrm{sim}}}{P_e} \tag{3.60}$$

whereas

$$z = \frac{DZ}{H^2 V_{\mathrm{bz}}} = \frac{Z}{H}\frac{D}{HV_{\mathrm{bz}}} = \frac{z_{\mathrm{sim}}}{P_e} \tag{3.61}$$

Flow boundary conditions As the assumptions claimed in Chapter 2, the screw is considered idle and the barrel rotates in a converse direction. Therefore, the velocity of the top, which is the barrel velocity, is set as a dimensionless value of 1 with pressure drop flow and is set as a dimensionless value of 2.30 with backpressure flow. This is in order to keep the same average residence time between two different pressure flows. The bottom velocity is zero. With the mathematical calculation in the previous section, the inflow rate is set 0.58. The outflow is set along outlet.

Thermal boundary conditions To study the laminar dispersion of thermal fluctuations along the metering zone of the screw channel, the thermal transition and the frictional heating from the barrel and screw are treated as a reference, and an adiabatic environment should be provided. Thus, the thermal boundary conditions are zero flux density imposed along top and bottom. The temperature imposed along inlet is a slug with a dimensionless length of 50, and to keep the flow consistency, outflow is set along outlet.

Numerical methods The Crank-Nicolson method, a second-order time-marching scheme, used for numerically solving transient ordinary differential equations (ode), is adopted in this work.

Results and discussion Length average temperature and mixing cup temperature are commonly used in Polyflow and work as important roles to give hints on temperature field character. In this work, the length average temperature is the average temperature along the depth at a specific point, and the mixing cup temperature is the bulk temperature. They can be expressed by Eqs.(3.62,3.63):

$$T_{\mathrm{Length\,ave}} = \int_0^1 T_{(y)}\,dy \tag{3.62}$$

$$T_{\mathrm{Mixing\,cup}} = \frac{\int_0^1 T_{(y)} V_z\,dy}{\int_0^1 V_z\,dy} \tag{3.63}$$

Fig. 3.6 shows the simulation results of length average temperature (a) and mixing cup temperature (b) with ANSYS Polyflow. In both figures, with backpressure in the flow, the blue curve starts earlier and have a lower peak, while the red curve has a higher breakthrough with a pressure drop in the flow. It confirms the conclusion obtained from the mathematical model that flow with backpressure have a more efficient dispersion process for initial thermal fluctuations.

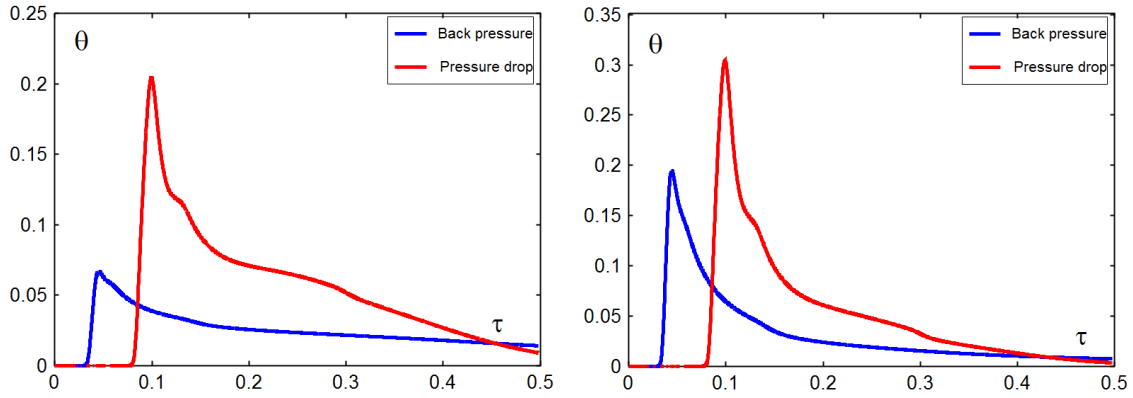

(a) Length average temperature (b) Mixing cup temperature

Figure 3.6: Length average temperature and mixing cup temperature with ”Billion 40” and slug-length 50. Red curve is when a pressure drop is considered, while blue curve is when a back pressure is considered.

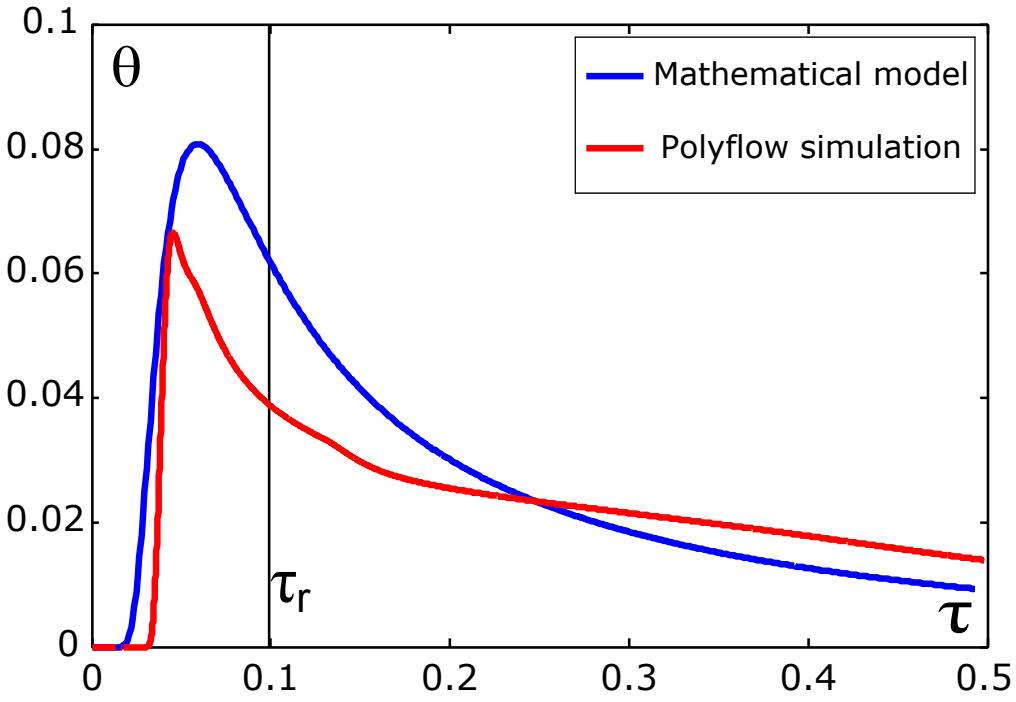

Figure 3.7: Dispersion behavior of thermal fluctuation in backpressure flow calculated separately by Mathematical model (blue curve) and Polyflow simulation (red curve), with the same dimensionless flow rate $q_m = 0.58$, and same dimensionless top wall velocity $V_{bz} = 2.30$.

3.2.4 Comparison of results from mathematical model and Polyflow

A 2-D model has been built in Polyflow, with a width/length ratio of 400 and a typical fine-meshed unit cell. The simulation result is compared with the result from the mathematical model, and the same conclusion can be drawn that thermal fluctuations in flow with a back pressure can disperse more efficiently. Besides, some differences, as shown in Fig. 3.7, between the results of Polyflow and the mathematical model can be observed. The main reason for the differences between the two curves is that our mathematical model, considered the time-dependent of thermal conductivity, are more diffusive. Therefore, we can find from the figure that the fluctuation in the blue curve begins earlier, that is because the thermal fluctuation reaches earlier with a stronger diffusion influence. The peak of the green curve is lower than the blue curve, which means the mathematical model predicts a larger thermal fluctuation at the end of the metering zone. General speaking, the results of our model have a similar prediction of thermal fluctuation with the result of Polyflow, at least, qualitatively. It is known in the literature [YU 81] that Gill's model over predicts the diffusion, but Gill's model gives a good estimate on how the initial slug length and the backpressure will play in the laminar dispersion.

3.3 Laminar dispersion of thermal fluctuations in Non-newtonian fluid

The laminar dispersion behavior of thermal fluctuations in a Newtonian fluid is studied in the previous section. An interesting phenomenon is discovered that thermal fluctuations in a flow with back pressure disperse more efficiently than in a flow with pressure drop. In practice, the polymer melt in the metering zone of plastication process is always non-Newtonian fluid. In this section, therefore, the previous model is extended to include the power-law index to study the laminar dispersion of thermal fluctuations in a non-Newtonian fluid in the metering zone of the plastication process.

3.3.1 Mathematical model

In the rectangular cross-section channel of the metering zone of the plastication process, the volumetric flow rate Q of a power-law fluid can be described as [BÉR 09]

$$\begin{aligned} Q &= V_0 HW \frac{\text{sign}(G)|6G|^s}{(s+1)(s+2)}(1-y_0)|1-y_0|^{(s+1)} + y_0|y_0|^{(s+1)} - (s+2)|y_0|^{(s+1)} \\ &= V_0 HW C_1 \end{aligned} \tag{3.64}$$

where

$$s = 1/n \tag{3.65}$$

$$G = \frac{H^{(n+1)}}{6KV_0{}^n}\frac{\partial p}{\partial x} \tag{3.66}$$

$$C_1 = \frac{\text{sign}(G)|6G|^s}{(s+1)(s+2)}[(1-y_0)|1-y_0|^{(s+1)} + y_0|y_0|^{(s+1)} - (s+2)|y_0|^{(s+1)}] \tag{3.67}$$

In these equations above, V_0 is the barrel velocity along the down-channel(Z) direction, H and W are the channel depth and width in the metering zone, respectively, G is the pressure gradient along the screw channel, K is the consistency factor, n is the power-law index, y_0 is the point in the y axis where the velocity gradient of V_z along y direction is zero. C_i (i = 1,2,3,...,8) are constants, which help to brief the equations.

The axial velocity $v(y)$ of flow in the down-channel direction (Z) can be represented as a dimensionless form:

$$v(y) = \frac{V_z}{V_0} \tag{3.68}$$

$$v(y) = \frac{|y-y_0|^{(s+1)} - |y_0|^{(s+1)}}{|1-y_0|^{(s+1)} - |y_0|^{(s+1)}} = C_2|y-y_0|^{(s+1)} + C_3 \tag{3.69}$$

where V_z is the corresponding laminar flow velocity in the Z-direction, y is a dimensionless coefficient of depth, derived from the laminar flow depth Y divided by the channel depth H in the metering zone. The average velocity V_{ave} in the z-direction can be obtained as

$$V_{ave} = \frac{Q}{HW} = V_0 C_1 \tag{3.70}$$

The dispersion of a dimensionless temperature fluctuation θ along the channel in the metering zone of a plastication screw could be described with the classic advection/diffusion equation:

$$\frac{\partial \theta}{\partial \tau} + v(y)\frac{\partial \theta}{\partial z} = \frac{1}{{P_e}^2}\frac{\partial^2 \theta}{\partial z^2} + \frac{\partial^2 \theta}{\partial y^2} \tag{3.71}$$

with the boundary conditions:

$$\left.\begin{array}{l} \theta(0,y,z) = 1 \quad (|x| \le \frac{1}{2}z_s) \\ \theta(0,y,z) = 0 \quad (|x| > \frac{1}{2}z_s) \\ \frac{\partial \theta}{\partial y}(t,0,z) = \frac{\partial \theta}{\partial y}(t,1,z) = 0 \end{array}\right\} \tag{3.72}$$

where $v(y)$ is the stationary velocity field from Eq. 3.69, τ is a dimensionless time, z_s is the initial thermal slug length and P_e is the dimensionless Peclet number.

The time scale and length scale for this problem are built on the polymer thermal diffusion coefficient D so that

$$z = \frac{DZ}{H^2 V_{\text{bz}}}, \quad \tau = \frac{Dt}{H^2}, \quad P_e = \frac{HV_{\text{bz}}}{D} \tag{3.73}$$

where Z is the length along the down-channel direction and t is the time.

Define a new axial coordinate moving with the average velocity of flow as

$$Z_1 = Z - V_{ave}t \tag{3.74}$$

In dimensionless form, writing

$$z_1 = z - V_{ave}\tau \tag{3.75}$$

Substitution of (3.75) in (3.71) yields

$$\frac{\partial\theta}{\partial\tau} + u(y)\frac{\partial\theta}{\partial z_1} = \frac{1}{{P_e}^2}\frac{\partial^2\theta}{\partial z_1^2} + \frac{\partial^2\theta}{\partial y^2} \tag{3.76}$$

where

$$u(y) = v(y) - C_1 = C_2|y - y_0|^{(s+1)} + C_4 \tag{3.77}$$

$$C_4 = C_3 - C_1 \tag{3.78}$$

The solution of Eq.(3.76) is formulated as a series expansion in $\partial^k\Theta_m/\partial z_1^k$

$$\Theta = \Theta_m + \sum_{k=1}^{\infty} f_k(\tau, y)\frac{\partial^k\Theta_m}{\partial z_1^k} \tag{3.79}$$

where

$$\Theta_m(z_1, \tau) = \int_0^1 \theta dy \tag{3.80}$$

Substituting Eq.(3.79) into (3.76) yields

$$\frac{\partial\theta_m}{\partial\tau} + u(y)\frac{\partial\theta_m}{\partial z_1} - \frac{1}{{P_e}^2}\frac{\partial^2\theta_m}{\partial z_1^2} + \sum_{k=1}^{\infty}[\frac{\partial f_k}{\partial\tau}\frac{\partial^k\theta_m}{\partial z_1^k} + f_k\frac{\partial\theta_m}{\partial\tau}\frac{\partial^k\theta_m}{\partial z_1^k}$$

$$+ u(y)f_k\frac{\partial^{k+1}\theta_m}{\partial z_1^{k+1}} - \frac{1}{{P_e}^2}f_k\frac{\partial^{k+2}\theta_m}{\partial z_1^{k+2}} - \frac{\partial^2 f_k}{\partial y^2}\frac{\partial^k\theta_m}{\partial z_1^k}] = 0 \tag{3.81}$$

Then, Gill's model with a time-dependent dispersion coefficient is used to compute the time evolution of the temperature fluctuation, which assumes:

$$\frac{\partial\theta_m}{\partial\tau} = \sum_{i=1}^{\infty} K_i(\tau)\frac{\partial^i\theta_m}{\partial z_1^i} \tag{3.82}$$

Here, we should note that the K_i are functions of τ, even though the velocity field is independent of τ. Besides, we have also

$$\frac{\partial}{\partial\tau}\left(\frac{\partial^k\theta_m}{\partial z_1^k}\right) = \sum_{k=1}^{\infty} K_i(\tau)\frac{\partial^{i+k}\theta_m}{\partial z_1^{i+k}} \tag{3.83}$$

Substitute Eq.(3.82) and (3.83) into (3.81), and equate the coefficients of $\frac{\partial^k \Theta_m}{\partial z_1^k}$ to zero can yield

$$\frac{\partial f_1}{\partial \tau} = \frac{\partial^2 f_1}{\partial y^2} - K_1 - u(y) \tag{3.84}$$

$$\frac{\partial f_2}{\partial \tau} = \frac{\partial^2 f_2}{\partial y^2} - K_2 + \frac{1}{{P_e}^2} - f_1 K_1 - u(y) f_1 \tag{3.85}$$

...

It can be easily obtained from the initial and boundary conditions on $f_k(\tau, y)$

$$\frac{\partial f_i}{\partial y}(\tau, 0) = \frac{\partial f_i}{\partial y}(\tau, 1) = 0 \tag{3.86}$$

$$f_i(0, y) = 0 \tag{3.87}$$

$$\int_0^1 f_i(y) dy = 0 \tag{3.88}$$

thus

$$\int_0^1 \frac{\partial f_i}{\partial \tau} dy = 0 = \int_0^1 \left[\frac{\partial^2 f_i}{\partial y^2} - K_1 - u(y) \right] dy = K_1 \tag{3.89}$$

$$K_2 = \frac{1}{{P_e}^2} - \int_0^1 u(y) f_1 dy \tag{3.90}$$

To get K_2, we need obtain the value of f_1, which can be seperated by two parts

$$f_1(\tau, y) = f_{1a}(\tau, y) + f_{1b}(y) \tag{3.91}$$

where $f_{1a}(\tau, y)$ is the part takes the effect of τ and y, and $f_{1b}(y)$ is only the function of y. Substitute (3.91) into (3.84), we can obtain

$$\frac{\partial f_{1a}}{\partial \tau} = \frac{\partial^2 f_{1a}}{\partial y^2} + \frac{\partial^2 f_{1b}}{\partial y^2} - u(y) \tag{3.92}$$

let

$$\frac{\partial^2 f_{1b}}{\partial y^2} - u(y) = 0 \tag{3.93}$$

$$\frac{\partial f_{1a}}{\partial \tau} = \frac{\partial^2 f_{1a}}{\partial y^2} \tag{3.94}$$

By integating Eq.(3.93), it can easily obtain

$$\frac{\partial f_{1b}}{\partial y} = C_5 |y - y_0|^{(2+s)} + C_4 y + C_6 \tag{3.95}$$

where

$$C_5 = -\frac{C_2}{2+s} \tag{3.96}$$

combine with the boundary conditions Eq.(3.86), C_6 can be obtained.

$$\frac{\partial f_{1b}}{\partial y}(0) = \frac{\partial f_{1b}}{\partial y}(1) = 0 \tag{3.97}$$

By integating Eq.3.95, f_{1b} can be expressed as

$$f_{1b} = C_7|y-y_0|^{(3+s)} + \frac{1}{2}C_4y^2 + C_6y + C_8 \tag{3.98}$$

where

$$C_7 = -\frac{C_5}{3+s} \tag{3.99}$$

and with the boundary condition Eq.(3.88), C_8 can be obtained.

f_{1a} can be obtained by using separate variable method/ Fourier method elucidated in the previous subsection,

$$f_{1a} = \sum_0^\infty A_k \exp(-k^2\pi^2\tau)\cos(k\pi y) \tag{3.100}$$

From Eq.(3.88), the following equation can be given by:

$$\int_0^1 f_{1a}dy = 0 \quad \text{thus} \quad A_0 = 0 \tag{3.101}$$

$$f_{1a}(\tau,y) = \sum_1^\infty A_k \exp(-k^2\pi^2\tau)\cos(k\pi y) \tag{3.102}$$

Eq.(3.87) gives $f_1(0,y) = 0$, thus

$$\sum_1^\infty A_k \cos(k\pi y) = -f_{1b} \tag{3.103}$$

Based on

$$\int_0^1 cos(k\pi y)cos(n\pi y)dy = \frac{1}{2}\delta kn$$

, multiply both sides of Eq.(3.103) by

$$\int_0^1 cos(n\pi y)dy$$

A_k can be expressed by

$$A_k = -2\int_0^1 f_{1b}cos(k\pi y)dy \tag{3.104}$$

Substituting Eq.(3.98) and Eq.(3.102) into Eq.(3.91) yields f_1

$$f_1 = \sum_1^{\infty} A_k \exp[-(k\pi)^2\tau]\cos(k\pi y) + C_7|y-y_0|^{(3+s)} + \frac{1}{2}C_4 y^2 + C_6 y + C_8 \tag{3.105}$$

To get $K_2(\tau)$, it can be separated as two parts:

$$K_2(\tau) = K_{2a}(\tau) + K_{2\infty} \tag{3.106}$$

where

$$K_{2a}(\tau) = -\int_0^1 u(y) f_{1a} dy \tag{3.107}$$

$$K_{2\infty} = \frac{1}{{P_e}^2} - \int_0^1 u(y) f_{1b}(y) dy \tag{3.108}$$

By calculating A_k, it is easy to notice the value decreases magnitude fast with the increase of k. Therefore, only the first five value from A_1 to A_5 are considered in this calculation:

$$K_{2a}(\tau) = -\sum_{k=1}^{5} A_k \exp[-(k\pi)^2\tau] \int_0^1 u(y)\cos(k\pi y) dy \tag{3.109}$$

Connect Eqs.(3.108) and (3.109), $K_2(\tau)$ can be obtained finally. As mentioned before, $K_3(\tau)$ and higher order dispersion coefficients can be neglected for a decrease in order of magnitude further. From Eq.(3.89), $K_1(\tau) = 0$, thus

$$\frac{\partial \theta_m}{\partial \tau} = K_2 \frac{\partial^2 \theta_m}{\partial z_1^2} \tag{3.110}$$

Since a thermal slug is considered as the initial thermal fluctuation, $\theta_m(\tau, z)$ should satisfy

$$\left.\begin{array}{ll} \theta_m(0, z_1) = 1 & (|z| <= \frac{1}{2} z_s) \\ \theta_m(0, z_1) = 0 & (|z| > \frac{1}{2} z_s) \\ \theta_m(\tau, \infty) = 0 & \end{array}\right\} \tag{3.111}$$

The solution for $\theta_m(\tau, z)$ can be described as

$$\theta_m(\tau, z) = \frac{1}{2}[erf(\frac{\frac{1}{2}z_s + z_1}{2\sqrt{\xi}}) + erf(\frac{\frac{1}{2}z_s - z_1}{2\sqrt{\xi}})] \tag{3.112}$$

where

$$\xi = \int_0^{\tau} K_2(r) dr$$

The polymer properties and screw geometry used in this model come from Gaspar-Cunha's thesis [GAS 00], as listed in Table 2.1.

To keep the same average residence time of melting polymer, the same flow rate along the screw channel is necessary. Therefore, a fixed flow rate $Q = 2.0\,\mathrm{cm}^3/\mathrm{s}$ is set according to the previous calculation with the model formulated by Béreaux et al. [BÉR 09], which is introduced in Chapter 2. It is easy to understand that a higher back pressure should combine with a higher screw rotation frequency in order to keep the same flow rate. Three cases, as listed in Table 3.1, are obtained. The corresponding parameters, calculated by wxMaxima, a fairly complete computer algebra system with an emphasis on symbolic computation, are displayed in the Table 3.2.

Tableau 3.1: 3 cases of processing parameters to keep same flow rate.

Case	Flow rate	RPM	Back pressure
Case1	2.0	30	0
Case2	2.0	50	912 E5
Case3	2.0	80	1860.65 E5

Tableau 3.2: 3 cases of processing parameters to keep same flow rate and the corresponding specific parameters C1-C8.

Parameters	Case1	Case2	Case3
C1	0.61755	0.37055	0.23159
C2	-0.034385	-0.046288	0.60961
C3	1.1506	-0.11448	-2.5126e-04
C4	0.53309	-0.48503	-0.23184
C5	0.0070194	0.0094493	0.12445
C6	-0.578	-0.039481	-6.9471e-06
C7	-0.00119	0.001602	0.021098
C8	0.28381	0.032058	0.031298

With all the values of screw geometry, polymer properties and processing parameters, Eq.(3.112) can be calculated numerically with Matlab. The evolution of thermal fluctuations with dimensionless time at the end of the metering zone are demonstrated in the following section.

3.3.2 Results and discussion of the model

Fig. 3.8 illustrates the evolution of thermal fluctuations with dimensionless time at the end of the metering zone of a screw channel, in the cases of three different operating conditions with the same throughput, i.e., the same average residence time. The red line case has a rotation frequency of 30 rpm and zero backpressure, which means a pressure drop flow in the channel of the metering zone, because the peak pressure near the beginning of the metering zone is about 23.5 MPa, calculated by the model of Béreaux et al. mentioned before. The green line case has a rotation frequency of 50 rpm and backpressure of 91.2

MPa, and the blue line, 80 rpm with 186 MPa backpressure. A higher screw rotation frequency makes the thermal slug take a shorter time to reach the end of the metering zone, therefore, the blue line first presents the thermal fluctuation in the dimensionless time axis. At the average residence time, it can be easy to find that, the flow with a pressure drop (the red line) has the most distinct thermal fluctuation, while the flow with a higher back pressure (the blue line) presents the lowest thermal peak, which means the thermal fluctuation disperses more efficiently in a higher back pressure power-law fluid, just as the conclusion in Newtonian fluid.

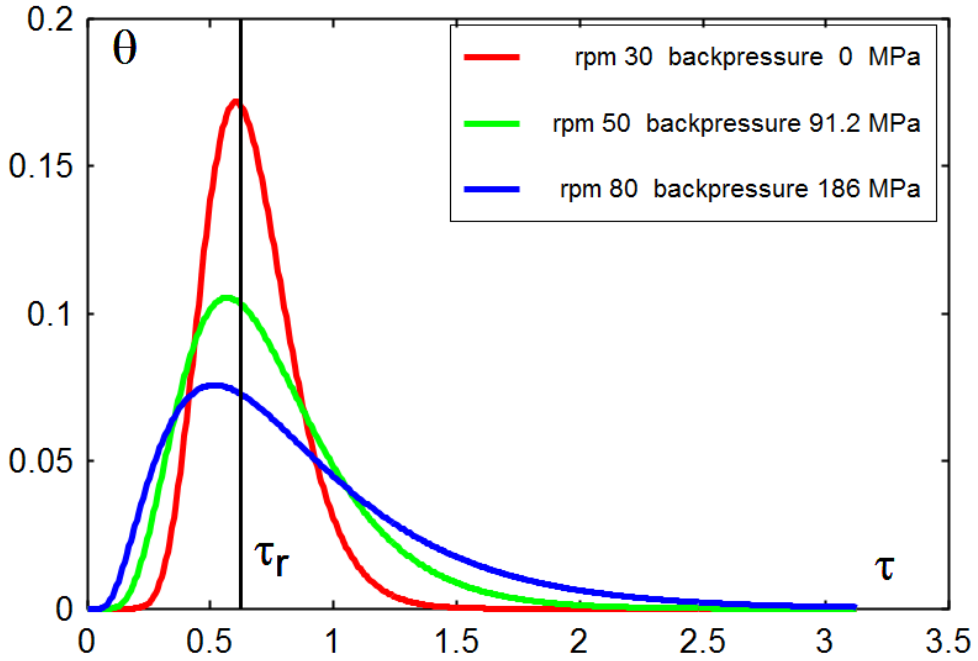

Figure 3.8: Evolution of the temperature fluctuation with dimensionless time at the end of the metering section. τ_r marks the average residence time from the edge of the temperature step to the end of the metering zone. Three cases with the same throughput but different operating conditions.

Fig. 3.9 demonstrates the effect of the power-law index on the dispersion behavior of thermal fluctuations at the end of the metering section. Two cases are calculated with the same throughput of 2.0 cm^3/s and same back pressure of 91.2 MPa but different power-law index: the red curve case n = 1 with 33.316 rpm screw rotation frequency, blue curve case n = 0.345 with 50 rpm. It can be observed that the wave of the red line starts later, as for a lower screw rotation frequency, but has a larger peak compared with the blue one. The result indicates that with the same throughput, temperature and backpressure, a fluid with the lower power-law index can make the thermal fluctuation disperse more evenly than with higher power-law index. Besides, it is interesting to find that, compared with Fig. 3.8, in which cases own the same throughput, the two red lines have a very similar shape, which the former outlines a non-Newtonian fluid with free backpressure and the latter presents the Newtonian with quite high backpressure.

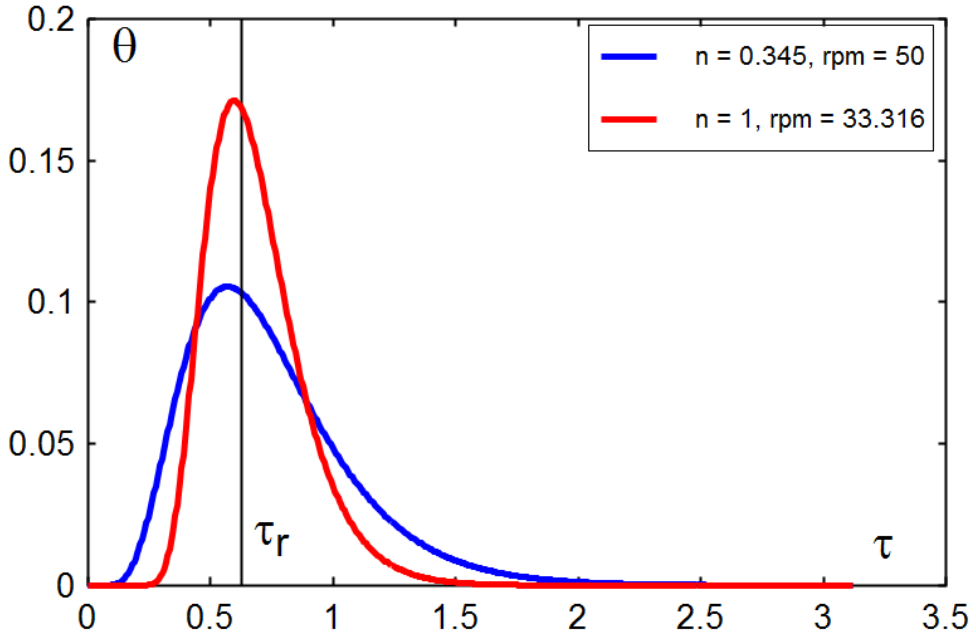

Figure 3.9: Comparison of dispersion behavior of thermal fluctuations with different power-law index of fluid. Two cases with same throughput of 2.0 cm^3/s and same back pressure of 91.2 MPa but different power-law index: Red curve case n = 1 with 33.316 rpm screw rotation frequency, blue curve case n = 0.345 with 50 rpm.

3.3.3 Results and discussion of Numerical simulation

Numerical simulations were conducted with ANSYS Polyflow, to calculate the dispersion behavior of thermal fluctuations in a non-Newtonian fluid. A 2-D model was created and the meshing, boundary conditions and numerical methods are kept the same with the numerical model described in Newtonian section. The material set in the simulation is HDPE, its properties have been listed in Table 2.1.

Fig.3.10 shows the evolution of thermal fluctuations with dimensionless time at different positions of the metering section of the screw channel. The blue line presents the dispersion behavior of thermal fluctuation at dimensionless position $z_{\text{sim}} = 10$, because the slug length of the thermal fluctuation is set as 25, the peak temperature in the blue line starts from the dimensionless 1, which equals to the value of the initial thermal slug. It can be found from this figure, a sharper peak is presented at the former position, like at $z_{\text{sim}} = 25$, which represents a more concentrated thermal slug at the residence time of the corresponding position, while the peak at the latter position, like at $z_{\text{sim}} = 100$, becomes wider, which contributes to the work of thermal diffusion. Moreover, the value of the peak temperature of thermal fluctuation decreases exponentially along the position of the metering zone, which indicates a longer metering zone in plastication process could help achieve a better thermal homogeneity in the melt flow.

The length average temperature and mixing cup temperature are shown in Fig.3.11. It can be found that thermal fluctuations of both length average temperature and mixing

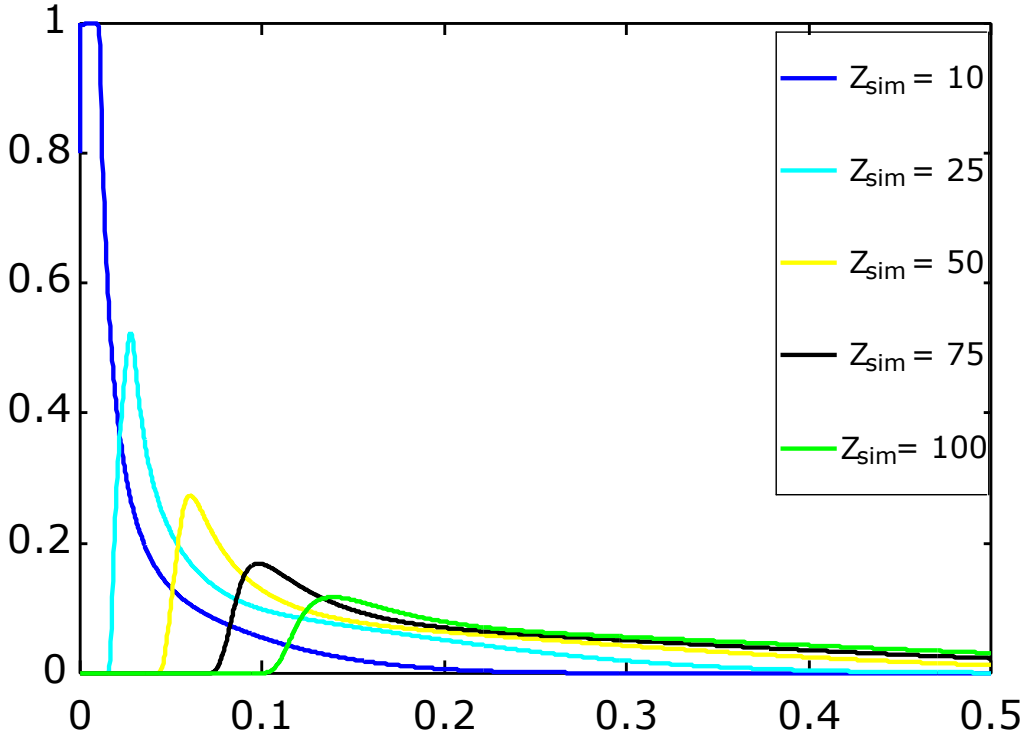

Figure 3.10: Dispersion behavior of thermal fluctuations at different position in non-Newtonian fluid.

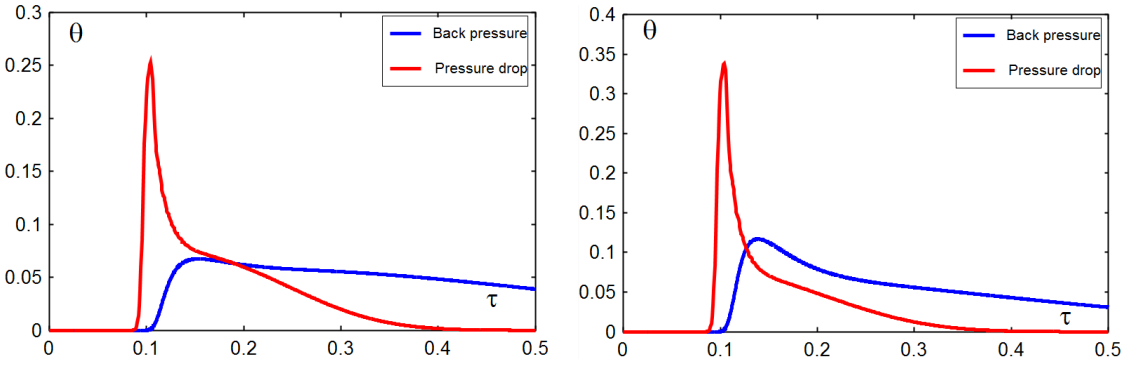

(a) Length average temperature (b) Mixing cup temperature

Figure 3.11: Evolution of thermal fluctuations with dimensionless time at $z_{\text{sim}} = 100$ in non-Newtonian fluid

cup temperature have a higher peak value in flow with a pressure drop than in flow with backpressure. This result supports the conclusion that thermal fluctuations can disperse more efficiently in a flow with higher back pressure, which can give suggestions to the set of operating conditions in the practical polymer forming process. Besides, the peak value of mixing cup temperature is higher than the corresponding length average temperature. This is because the mixing cup temperature defines the average temperature in a given bulk, which results in an equilibrium temperature that accurately reflects the average temperature of the moving fluid, more so than a simple average like the length average temperature, which calculates the average temperature along the depth at a specific position.

3.4 Conclusions

In this chapter, an initial thermal fluctuation is assumed to present at the beginning of the metering section of the screw channel. The advection-diffusion equation is used to study the dispersion behavior of the thermal fluctuation at the end of the metering section. It is found that the typical residence time in a single screw is around one-tenth of the thermal diffusion time scale. This residence time is too short for the dispersion coefficient to reach a steady-state, but too long to neglect radial thermal diffusion and to resort to a purely convective solution. Therefore, a mathematical model with a time-dependent dispersion coefficient is developed to demonstrate the laminar dispersion behavior of thermal fluctuations. The primary model is formulated in Newtonian fluid and then it was developed to a non-Newtonian fluid situation. Numerical simulations are conducted with ANSYS Polyflow to make a comparison with the results from the mathematical models. Several conclusions are listed as follows:

(1) The peak of thermal fluctuation presented at the end of the metering zone increases with the enhancement of slug length in a Newtonian fluid.

(2) The results from ANSYS Polyflow and our mathematical model are similar to the tendency of the dispersion behavior of thermal fluctuations. And the differences of the results could because that our mathematical model, considering the time-dependent of thermal conductivity, are more diffusive than the numerical results, based on the finite element method.

(3) The value of the peak temperature of thermal fluctuation decreases exponentially along the position of the metering zone, which indicates a longer metering zone in plastication process could help achieve a better thermal homogeneity in the melt flow.

(4) In simulation results, the mixing cup temperature defines the average temperature in a given bulk of the moving fluid, presents a higher peak temperature than the length average temperature, which calculates the average temperature along the depth at a specific position.

(5) The power-law behavior of fluid affects the dispersion behavior of thermal fluctuations. With the same throughput, temperature and backpressure, a fluid with lower power-law index can make the thermal fluctuation disperse more evenly than with higher

power-law index.

(6) In both Newtonian and non-Newtonian fluid, concluded by both mathematical model and numerical simulation: temperature fluctuations disperse more evenly with time in a flow with high backpressure, whereas a pressure drop in the flow results in a break-through curve which presents a larger peak of fluctuation. It gives hints that through an increase of backpressure, to some degree, in practical polymer processing can expect a better thermal homogeneity at the end of the metering section of the screw channel.

Chapter 4

Laminar dispersion of inlet thermal fluctuations

In this chapter, the capacity of this particular drag and pressure flow to dampen inlet temperature disturbances occurring at the beginning of the metering zone of the screw channel is studied. The integral transform method is applied to the transient energy conservation equation with the laminar velocity profile of a Newtonian fluid. It is found that a higher level of backpressure is indeed improving the thermal homogeneity in the flow. Moreover, for any given flow, the high-frequency disturbances are dampened more efficiently than the low-frequency disturbances.

Contents

4.1 Introduction

Single-screw plastication, used in extrusion and in injection moulding, is a major way of processing commodity thermoplastics. During the plastication phase, the polymeric material is melted by the combined effects of shear-induced self-heating (viscous dissipation) and heat conduction coming from the barrel. Once the polymer is completely melted, a combined drag and pressure difference flow is imparted onto the molten polymer along the last zone of the screw channel, the so-called metering zone. The very high viscosity of molten polymers insures that the flow must be laminar and that the Reynolds number is negligible. The low thermal diffusivity of molten polymers implies that convection is dominant over diffusion and leads to large Peclet numbers. However, the screw channel length is large enough for the flow to present significant diffusion effects. Indeed, calculations for frequently encountered polymer processes show that the residence time is one-tenth of the thermal diffusion time, owing to the very low thermal diffusion of polymers.

In these polymer shaping processes, a high level of reliability is usually achieved that makes this process ideally suited to mass market production. Nonetheless, process fluctuations still appear that make part quality control an everyday issue. Among the possible processes fluctuations, thermal fluctuations occurring at the plastication stage, which is early on in the polymer shaping process, could well be the cause for a temperature perturbation that will be carried to the part all the way through the die in extrusion or through the mould in injection moulding, because of the low thermal diffusivity of the polymer. Therefore, the main objective of this chapter is to study the capacity of this particular class of flows to dampen any transient inlet temperature disturbances occurring at the beginning of the metering zone of the screw channel. In particular, in this class of flows, the level of backpressure is a process parameter that can be set to a chosen value, in order to change the flow configuration. It is well known in polymer processing that a higher level of backpressure will increase the level of shear rate inside the flow, thus enhancing the mechanical mixing capacity of the flow. However, if it is relatively easy to scale this improvement for purely mechanical mixing, there is nothing in the polymer processing literature on the consequences of a change in a drag and pressure driven flow configuration when combined convection-diffusion physics are taking place in this flow.

Knowing that the flow velocity profile is central to the laminar dispersion problem, which is close to the subject studied here, we envisage that changing the screw channel flow configuration will have profound repercussions on the heat transfer taking place in this channel and that it is a matter of interest to thoroughly investigate the forced convection heat transfer for a drag and pressure driven flow, in the same fashion as the pressure driven flows (Poiseuille flow) in cylindrical tube or between parallel plates have been studied before.

In the first section, the characteristic lengths, times and relevant dimensionless numbers are established to set the framework for the forced convection heat transfer problem.

In the second section, the integral transform method used throughout this work is reviewed. The integral transform method is a well established analytical method in the field

of forced convection heat transfer and has found numerous applications in steady state and transient heat transfer, particularly in heat exchangers [KAK 90b][FAK 14]. Integral transform method gives a much clearer view of the structure of the solution in one or two-dimensional convection-diffusion flows than any of the classical approximate methods like finite element, finite difference, or finite volume methods. An appealing feature of this method is that it computes a set of eigenvalues and associated eigenfunctions, unique to a given problem. These eigenvalues reveal how the solution propagates and dampens along the flow direction. Moreover, because these eigenvalues are invariant scalars, they can be used to compare different flows unambiguously.

The integral transform method is applied to the transient energy conservation equation with the laminar velocity profile obtained for drag and pressure driven flows of a Newtonian fluid. First, the steady-state laminar heat transfer problem is solved and extended to the transient case with a periodic single frequency transient inlet temperature. In this later part, we exactly follow the procedure established by Cotta [COT 86b]. The steady-state eigenvalues are required to build the transient solution.

4.2 Integral transform method for forced convection in metering zone

4.2.1 Characteristic lengths, times and dimensionless numbers

A standard screw channel in the metering zone can be modelled as a shallow rectangular duct of infinite width, with the barrel wall moving relative to the screw wall [BU 18], hence reducing the complexity of a tridimensional transient flow to a two-dimensional steady-state flow. Selecting the channel depth in the metering zone as reference length H and the circumferential screw velocity V_{bz} as reference velocity, we have the velocity profile:

$$u(y) = p_g(y^2 - y) + y \tag{4.1}$$

$$p_g = \frac{\Delta P}{L}\frac{H^2}{2\eta_0 V_{\mathrm{bz}}} \tag{4.2}$$

$$y = \frac{Y}{H} \tag{4.3}$$

where y is the dimensionless depth and p_g is a dimensionless pressure gradient which value can be selected at will, and which changes the flow configuration as seen in Fig. 4.1, η_0 a viscosity and ΔP a pressure difference. This dimensionless pressure gradient is built on the ratio between the actual pressure gradient and the shear stress in the channel. The Reynolds number is always very low for polymer melt flows, with the consequence that the flow is always fully developed.

The advection-diffusion equation is used to describe the temperature profile in the screw channel, as outlined in Eq. 4.4 the left term refers to the thermal advection in the flow direction (z) and the right term represents the thermal diffusion in (y) direction:

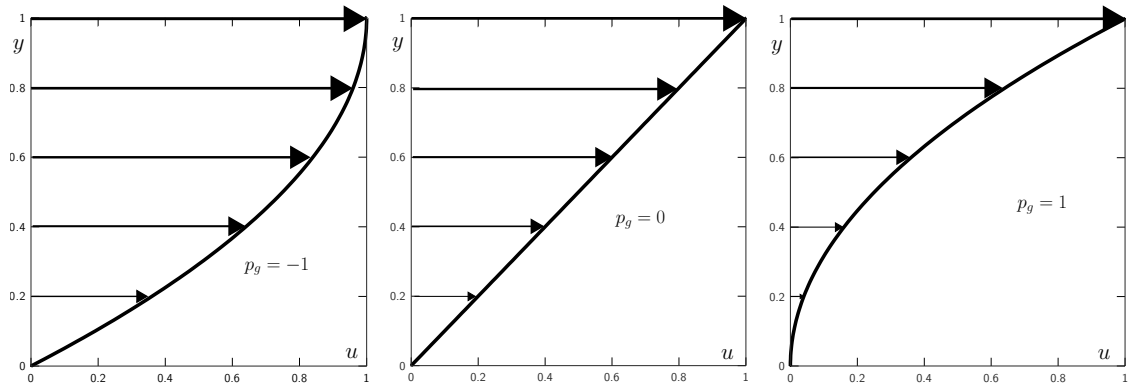

Figure 4.1: Velocity profiles $u(y)$ for different levels of pressure gradient $p_g : -1, 0, 1$ of drag and pressure driven flows

$$\frac{\partial \theta}{\partial \tau} + u(y)\frac{\partial \theta}{\partial z} = \frac{\partial^2 \theta}{\partial y^2} \tag{4.4}$$

with:

$$z = \frac{DZ}{H^2 V_{\mathrm{bz}}},\ \tau = \frac{Dt}{H^2},\ P_e = \frac{HV_{\mathrm{bz}}}{D} \tag{4.5}$$

In the preceding equations, D is the thermal diffusivity, z the dimensionless space variable in the flow direction and τ the dimensionless time. The Peclet number P_e usually reaches value of a 1000 and more, making the case for a convection dominated problem analysis.

4.2.2 Steady-state solution

The steady-state forced convection problem is viewed as a class I problem in the classification given by Mikhailkov [MIK 84] with homogeneous boundary condtions.

$$u(y)\frac{\partial \theta}{\partial z} = \frac{\partial^2 \theta}{\partial y^2} \tag{4.6}$$

$$\mu_k^2 u(y) Y_k + \frac{d^2 Y_k}{dy^2} = 0 \tag{4.7}$$

$$Y_k = 0 \text{ at } y = 0 \text{ and } y = 1$$

where finding the temperature field $\theta(y,z)$ is the main problem and finding the eigenvalues μ_k and the corresponding eigenfunctions $Y_k(y)$ with homogeneous boundary conditions is the auxiliary problem. The customary integral transform pair is therefore defined

as:

$$\bar{\theta}_k(z) = \int_0^1 \frac{1}{N_k} u(y)\theta(y,z)Y_k(y)dy \tag{4.8}$$

$$\theta(y,z) = \sum_{k=1}^{\infty} \frac{1}{N_k}\bar{\theta}_k Y_k(y) \tag{4.9}$$

$$N_k^2 = \int_0^1 Y_k(y)Y_k(y)dy \tag{4.10}$$

where N_k is the norm of the eigenfunction.

The upstream boundary condition at $z = 0$ can be any function of y:

$$\theta(y,0) = f(y) \tag{4.11}$$

The integral transfom of the temperature field obeys the ordinary differential equation:

$$\frac{d\bar{\theta}_k}{dz} + \mu_k^2\bar{\theta}_k = 0 \tag{4.12}$$

which readily admits the solution:

$$\bar{\theta}_k = \bar{f}_k \exp\left(-\mu_k^2 z\right) \tag{4.13}$$

where $\bar{f}_k$ is the integral transform of the upstream boundary condition Eq. 4.11.

Compounding calculations above, we can express the temperature field solution as

$$\theta(y,z) = \sum_{k=1}^{\infty} \frac{1}{N_k}\bar{f}_k \exp\left(-\mu_k^2 z\right) Y_k(y) \tag{4.14}$$

4.2.3 Transient solution

The transient heat transfer problem is defined in Eq. 4.15.

$$\frac{\partial\theta}{\partial\tau} + u(y)\frac{\partial\theta}{\partial z} = \frac{\partial^2\theta}{\partial y^2} \tag{4.15}$$

$$\theta(0,z,\tau) = 0 \tag{4.16}$$

$$\theta(1,z,\tau) = 0 \tag{4.17}$$

$$\theta(y,0,\tau) = \cos(\Omega\tau) \tag{4.18}$$

where the same thermal boundary conditions applied as before except for the inlet temperature which is now periodic. Cotta's work states that a periodic solution is to be found as the real part of the following complex solution:

$$\theta(y,z,\tau) = Re\left(\tilde{\theta}(y,z)\exp(i\Omega\tau)\right) \tag{4.19}$$

The unknown temperature field $\tilde{\theta}$ is put into the previous differential equation Eq. 4.15 to form a new set of problems:

$$i\Omega\tilde{\theta} + u(y)\frac{\partial\tilde{\theta}}{\partial z} = \frac{\partial^2\tilde{\theta}}{\partial y^2} \tag{4.20}$$

while keeping the same auxiliary problem given in Eq. 4.7. This departs from the integral transform method, but permits avoiding to solve a eigenvalue problem in the complex space.

The integral tansform pair is now defined as:

$$\bar{\tilde{\theta}}_j(z) = \int_0^1 \frac{1}{N_j} u(y) Y_j(y) \tilde{\theta}(y,z) dy \tag{4.21}$$

$$\tilde{\theta}(y,z) = \sum_{j=1}^{\infty} \frac{1}{N_j} Y_j(y) \bar{\tilde{\theta}}_j(z) \tag{4.22}$$

Following the integral transform method, the integral of the partial differential equations Eq. 4.19 and Eq. 4.7 are performed over the interval $y = [0,1]$. Integrating by part the second derivatives in each equation, an infinite linear set of coupled ordinary differentials equations is obtained:

$$\frac{d\bar{\tilde{\theta}}_k}{dz} + \mu_k^2 \bar{\tilde{\theta}}_k + i\Omega \sum_{j=1}^{\infty} a_{kj} \bar{\tilde{\theta}}_j = 0 \tag{4.23}$$

$$a_{kj} = \frac{1}{N_k N j} \int_0^1 Y_j Y_k dy \tag{4.24}$$

This system of coupled differential equations has to be truncated to the same number of computed eigenvalues in order to be solved in practice. Introducing the vector X of unknown transformed temperature:

$$\underline{X}(z) = \left(\bar{\tilde{\theta}}_1(z), \ldots, \bar{\tilde{\theta}}_k(z), \ldots, \bar{\tilde{\theta}}_N(z)\right) \tag{4.25}$$

The vector $\underline{X}$ is now the solution of a symmetric finite linear set of differential equations :

$$\dot{\underline{X}} = -\underline{\underline{A}} \cdot \underline{X} \tag{4.26}$$

$$= -\left(\underline{\mu}.\underline{\underline{1}} + i\Omega\underline{\underline{B}}\right) \tag{4.27}$$

$$A_{kj} = \mu_k^2 \delta_{kj} + i\Omega b_{kj} \tag{4.28}$$

with the real positive eigenvalues μ_k^2 positioned on the diagonal of the complex matrix $\underline{\underline{A}}$. Cotta and Özişik [COT 86a] chose to solve this system by computing the eigenvalues λ_k and eigenvectors $\underline{v}^k$ of $\underline{\underline{A}}$. Hence, the solutions vector $\underline{X}$ is expressed in the eigenvectors basis as :

$$\underline{X}(z) = \sum_{k=1}^{N} C_k \exp(-\lambda_k z)\, \underline{v}^k \tag{4.29}$$

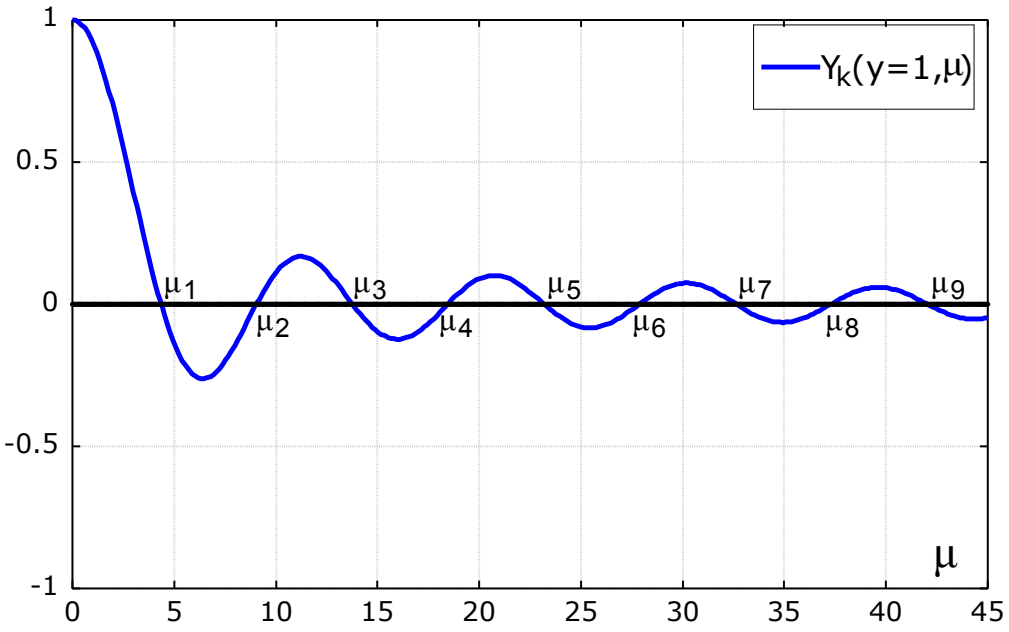

Figure 4.2: Eigenvalues (μ_k) at y = 1.

where the coefficient C_k can be found by expressing also the initial condition vector $\underline{x}(0)$ in the eigenvector basis.

4.3 Results and discussion

4.3.1 Eigenvalues and eigenfunctions calculation

The eigenvalue problem described in Eq. 4.7 and Eq. 4.8 is solved in a straightforward fashion following the procedure described by [BRO 60]. The unknown eigenfunction is expanded in a series of increasing power of the variable y:

$$Y_k(y) = \sum_{i=1}^{i=n} b_{ki} y^i \tag{4.30}$$

where b_{ki} are now unknown coefficient to be determined by a recurrence relation. This recurrence relation is readily established by applying the differential equation to the polynomial expression of Y_k in Eq. 4.30. The choice to express the eigenfunctions as polynomials is adopted because the velocity profile $u(y)$ is itself a polynomial in y. Finally, the homogeneous boundary condition at $y = 1$ is used as a non-linear equation of which the eigenvalues μ_k are the roots as shown in Fig. 4.2.

It is worth recalling that a particular eigenvalue problem is attached to a velocity profile defined in Eq. 4.1 by the chosen value of the parameter p_g. In this work, three different values of p_g are chosen to be representative of the different flow configurations:

p_g	-1	0	1
μ_1	3.6723	4.35388	5.5618
μ_2	7.6688	9.04912	11.8123
μ_3	11.6679	13.7558	18.0848
μ_4	15.6675	18.4653	24.3627
μ_5	19.6673	23.1760	30.6427
μ_6	23.6671	27.8872	36.9239
μ_7	27.6670	32.5988	43.2056
$\Delta\mu_{k,k+1}$	4	4.71	6.28

Tableau 4.1: Seven first eigenvalues computed for the three different cases of pressure gradient p_g

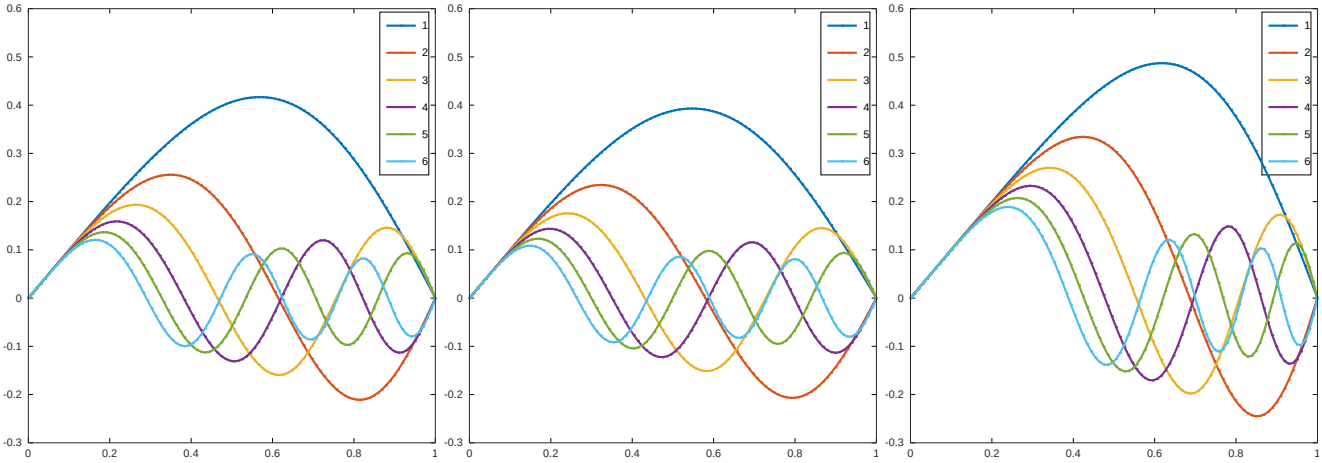

Figure 4.3: Six eigenfunctions for the three different cases of pressure gradient p_g: $p_g = -1$ left; $p_g = 0$, center; $p_g = +1$, right.

$p_g = 0$ for pure drag flow, $p_g = -1$ for pressure loss and drag flow, and $p_g = 1$ for backpressure flow.

In Table 4.1 the first seven eigenvalues are given: It can be seen that these eigenvalues tend to be evenly spaced, with the average difference between two consecutive eigenvalue given in the last line of Table 4.1.

The corresponding eigenfunctions are drawn in Fig. 4.3, for the three different pressure gradients p_g.

4.3.2 Periodic inlet temperature solution

The most important question that this model was built to answer is how an inlet temperature fluctuation with a given frequency Ω is transported at the other end of the screw channel, how this signal is distorted and to what extent its amplitude and phase lag are affected by the precise velocity profile in use. A straightforward mean to assess this, is to

follow the temperature over time at a given location downstream from the inlet boundary. Therfore, we define the mixing cup average temperature and the length average temperature over the channel depth as:

$$\theta_{\mathrm{mxcp}}(z,\tau) = \frac{1}{q}\int_0^1 u(y)\theta(y,z,\tau)dy \tag{4.31}$$

$$\theta_{\mathrm{lav}}(z,\tau) = \int_0^1 \theta(y,z,\tau)dy \tag{4.32}$$

where q is the dimensionless flow rate.

Comparisons between the mixing cup average temperature computed from the model and from Finite Element Method (FEM) simulation results are shown in Fig. 4.4 at two different locations $z = 0.05, 0.1$ for the three different level of pressure difference $p_g = -1, 0, +1$ and three different dimensionless frequencies $\Omega = 5$, 10, 50. The fully transient FEM simulations were carried out with $P_e = 1000$ and with axial conduction taken into account in the energy conservation equation. A number of insights can be obtained from the results. First, once the temperature wave has reached the chosen location in the screw channel it can be seen that the match between the periodic solution given by the model and the fully transient FEM solution is perfect, whether for the amplitude or the phase, for all inlet temperature frequencies ($\Omega = 5$, 10, 50) and for all pressure gradients ($p_g = -1$, 0, $+1$).

The case of the backpressure flow $p_g = +1$ with inlet temperature frequency $\Omega = 50$ in Fig. 4.4 is particularly interesting: In the FEM simulation results, once the temperature wave has reached the location at $z = 0.1$, the transient temperature exhibits first an amplitude undershoot, followed by an overshoot and then matches the periodic solution.

The accuracy of the temperature solution given by the integral transform model is on display again in Fig. 4.5 where the comparison between the mixing cup, length averaged temperature and FEM simulation results are plotted. Because the velocity profiles differs from a slug flow, there are differences between the mixing cup and the length averaged temperatures, though they are quite small. Nevertheless, there is still a perfect match between each type of average temperature and the corresponding FEM calculations.

This validates completely Cotta and Özişik's approach for a larger dimensionless frequency Ω and for a different velocity profile from the pressure driven flow they considered in [COT 86a] for instance.

Second, we can clearly see in Fig. 4.4 the extent of the dampening of the inlet temperature signal when a higher backpressure is employed. The higher the backpressure p_g, the higher the amplitude dampening of the inlet temperature.

Turning now to the effect of the inlet disturbance frequency on the temperature field, it is of interest to notice in Fig. 4.4 that a larger dampening of the temperature signal is observed when a higher frequency Ω is considered.

This has, to our best knowledge, never been reported in the literature [COT 86a, SPA 68, KAK 90a, KAK 73, CHE 99] before, because the frequencies these authors considered where smaller than those we considered here.

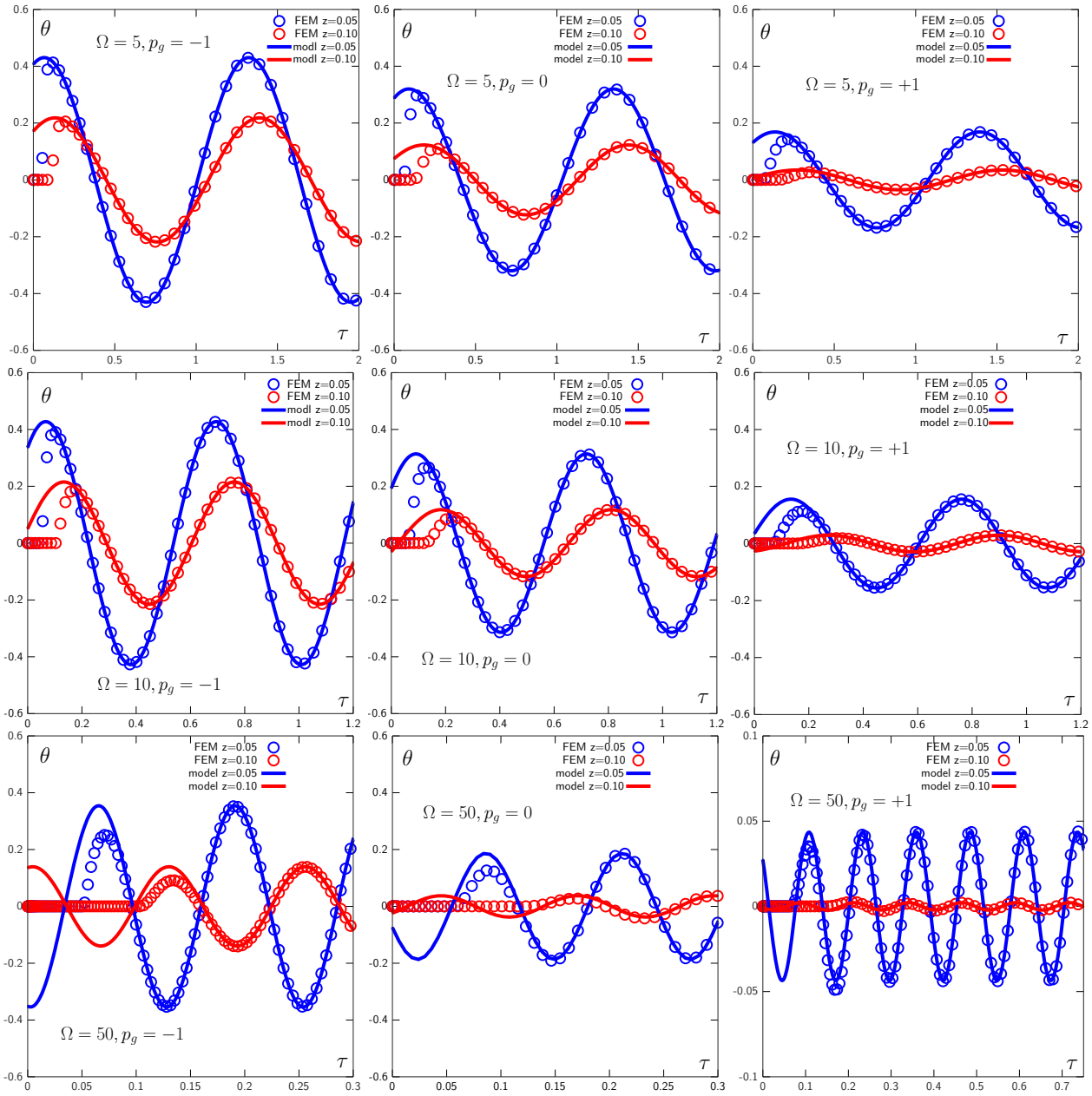

Figure 4.4: Mixing cup average temperature along dimensionless time τ for the three different value of dimensionless pressure gradient : $p_g = -1$ left column ; $p_g = 0$, centre column; $p_g = +1$, right column. Inlet temperature frequency $\Omega = 5$, top row; $\Omega = 10$, centre row, $\Omega = 50$, bottom row. Comparison between model predictions (solid blue line $z = 0.05$, solid red line $z = 0.1$) and FEM simulation results (circle) at $P_e = 1000$.

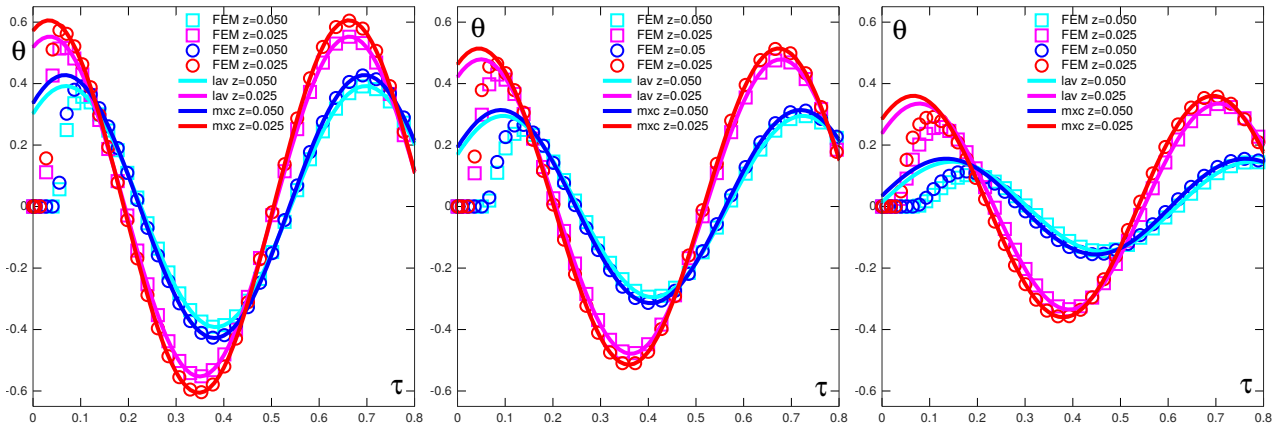

Figure 4.5: Length average ("lav") and mixing cup ("mxc") average temperatures along dimensionless time τ at locations $z = 0.025$ and $z = 0.05$ for the three different values of dimensionless pressure gradient : $p_g = -1$ left; $p_g = 0$, centre; $p_g = +1$, right. Comparison between model predictions and FEM simulation results at $P_e = 1000$. Inlet temperature frequency $\Omega = 10$.

We recast the mixing cup average of the complex temperature solution $\tilde{\theta}_{\text{mxcp}}$ as :

$$\tilde{\theta}_{\text{mxcp}} = A(z)\exp\left(i\Omega\tau + \phi(z)\right) \tag{4.33}$$

where $A(z)$ and $\phi(z)$ stand for the amplitude and the phase lag of the periodic temperature solution.

The evolution of the mixing cup average temperature amplitude along z, given both by the model and the FEM simulation results, are displayed in Fig. 4.6. The temperature decay is very well predicted by the model, up to nearly three decades in magnitude in the case of $p_g = +1$ and $\Omega = 50$, as proved by the match with the FEM simulation results. Only seven eigenvalues were needed to get to this level of accuracy.

Inspection of the differential equations system in matrix form Eq. 4.27 and Eq. 4.29 suggests that the amplitude $A(z)$ should scale with the real part of the lowest complex matrix eigenvalue λ_1, whereas the phase lag $\phi(z)$ should scale with its imaginary part. This is indeed the case for the amplitude plotted on Fig. 4.6 where the exponential dampening is obvious in the semi-logarithmic plot scale. Also undoubtedly clear is the fact that the long range behaviour of the amplitude is given by the real part of eigenvalue λ_1s and follows the relation:

$$A(z) = A_0\exp\left(-\text{Re}(\lambda_1)z\right) \tag{4.34}$$

When the frequency Ω is small, the eigenvalue λ_1 do not differ much from its real counterpart μ_1, because the complex part of the solution scales with Ω.

The evolution of the phase lag normalised by the frequency Ω along the flow direction z is plotted on Fig. 4.7 for the three different pressure gradients $p_g = -1, 0, +1$ and for two different dimensionless frequencies $\Omega = 5, 50$. The phase lag evolution is linear with z, showing a continuously increasing delay between the inlet temperature signal and its measurement at any point z.

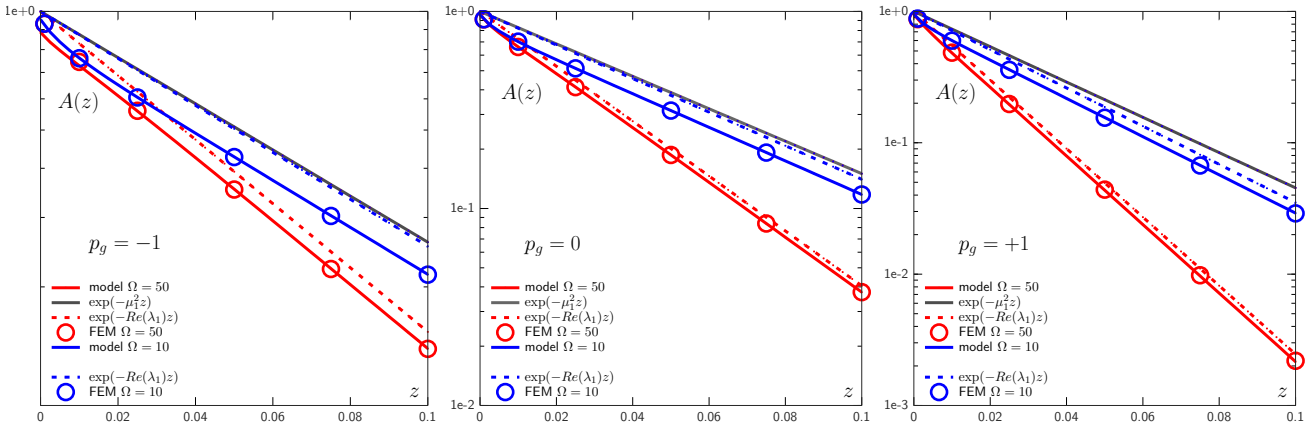

Figure 4.6: Amplitude of mixing cup average temperature (solid line) along dimensionless space z, at dimensionless pressure gradient $p_g = -1$ left; $p_g = 0$, centre; $p_g = +1$, right, at dimensionless frequency $\Omega = 10$ (blue colour) and $\Omega = 50$ (red colour). Comparison between model (solid blue or red lines) and exponential dampenings with μ_1^2 (solid gray line) and $\mathrm{Re}(\lambda_1)$ (dashed blue or red line) factors, and FEM simulation results at $P_e = 1000$ (circle).

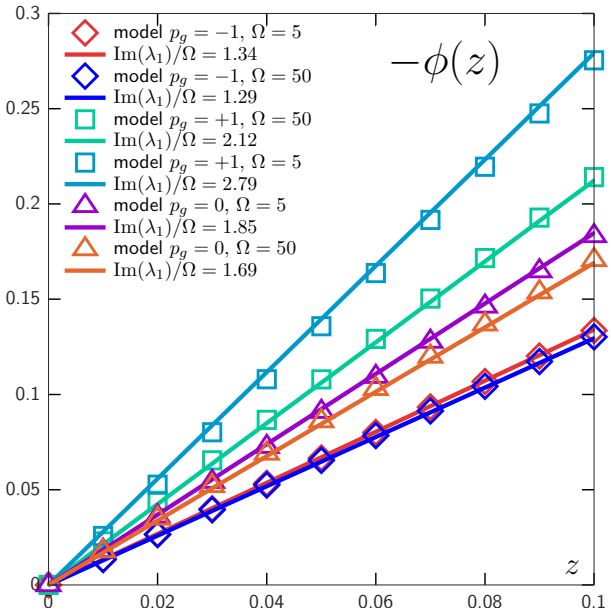

Figure 4.7: Evolution of phase lag of the mixing cup average temperature $\phi(z)$ along flow direction z. Values are normalised by inlet temperature dimensionless frequency Ω. Comparison between model solution (symbols) and linear relation (solid lines) Eq. 4.35.

The phase lag is much larger when a positive pressure difference (backpressure) is used as evidenced by the results for $p_g = +1$ in Fig. 4.7.

Moreover, in all cases this linear evolution is well captured by the linear relation :

$$\phi(z) = -\mathrm{Im}(\lambda_1)\Omega z \tag{4.35}$$

However, the imaginary part of the lowest eigenvalue λ_1 depends itself on Ω as indicated by the difference of slopes between the cases at $\Omega = 5$ and $\Omega = 50$ for the flow with pressure gradient $p_g = +1$.

4.4 Conclusions

In this chapter, the capacity of the drag and pressure driven flow to dampen transient inlet temperature disturbances occurring at the beginning of the metering zone of the screw channel is explored. The integral transform method for heat transfer in polymer melt flow with transient inlet temperature has been successfully used for the drag and pressure driven flow in a rectangular single screw channel. It is found that:

(1) The knowledge of the lowest eigenvalue is sufficient to characterize the dampening efficiency of a flow, and the knowledge of the first six eigenvalues are sufficient to describe the laminar dispersion behavior of the inlet periodic thermal fluctuations.

(2) Both the amplitude and the phase lag have been quantitatively related to the lowest complex matrix eigenvalue of the integral transform problem. Moreover, there is a large influence of the inlet temperature frequency on the amplitude dampening of the temperature wave and a linear dependence on its phase lag. For any given flow, the high-frequency disturbances are dampened more efficiently than the low-frequency disturbances.

(3) The most important result is that a higher level of backpressure (positive pressure gradient) in the flow will result in a much more efficient dampening of the inlet temperature fluctuation.

Chapter 5

Numerical analysis of a visual barrel with transparent windows

In this chapter, a visual barrel with transparent windows are created with ANSYS Workbench, the failure theory of this visual barrel is built, the effect of contact types, length of glass windows, temperature, pressure, and material properties on the safety factor of the glass blocks are discussed.

Contents

5.1 Introduction

The plastication process plays a key role in the polymer processing industry and the accomplishment of the project SAPRISTI requires a better understanding of the plastication process. One of the best ways to study the plastication process is to design a barrel with transparent windows, in order to have an in-line visualization of the polymer status in the barrel through photography or video recording. As a number of studies reviewed in Chapter 1, several research groups have designed and manufactured their unique barrels with transparent windows. With the experimental results of the innovative equipment, new theories like the non-plug solid conveying theory [FAN 91] are validated and new phenomena, e.g. solid bed breakage [GAO 00] is observed to promote the explanation on the polymer melting behavior.

An industry-sized metallic barrel with transparent glass windows designed and realized by Pham *et al.*, who have worked in INSA-Lyon (Site de Plasturgie) as well, possesses 3 optical glass blocks and 9 windows to be able to observe the state transformation of polymer in the system, from the solid state to the molten state, and be able to track and control the dispersion of the charged Nano-fluorescent in the polymer [PHA 13]. The optical glass blocks were not robust enough in the common working conditions, however, despite an extremely meticulous and careful procedure for warming up the barrel before any experiment and cooling it down after, cracks were appearing in the glass windows. The reasons for the breakage of the glass windows are still unclear.

Based on Finite Element Analysis, ANSYS Workbench is a simulation platform, aims to conduct modelling and solving of a wide range of engineering problems. ANSYS is a suite of advanced engineering simulation technology, and the Workbench platform combines access to ANSYS applications with utilities that manage the product workflow and improve productivity and maneuverability among engineering teams. To date, ANSYS Workbench is used in a number of fields of study with diverse engineering applications, such as heat transfer (helical heat exchangers [HUM 11], combustion engine heat-transfer analysis [KUM 17]), structural and solid mechanics (automotive bumper simulation [JOH 14], wind turbine blade design optimization [SON 11]). It provides reliable results or solutions for complicated engineering problems.

In this chapter, ANSYS Workbench is used to simulate the working status of the "visual barrel" designed by Pham *et al.* to analyze the failure reasons of the glass windows, which were initially designed by ANSYS Workbench and we have taken the step to perform the simulation on the entire barrel. Pham's model [PHA 13] of the visual barrel is recreated with some simplifications in ANSYS DesignModeler. The Mohr-Coulomb stress safety tool is used to evaluate the durability of the system, and the minimum value of the safety factor of the glass blocks is expected to be 3. The influence of several processing parameters, e.g. the temperature value, the boundary conditions, the pressure field, and the material mechanical properties, and the length of the glass windows on the safety factor of the glass blocks are studied. Some conclusions based on these results are obtained to build a more robust visual barrel.

5.2 Failure theory

To study the failure reasons of the visual barrel designed by Pham *et al.*, the criterion of safety must be confirmed. Safety factor principle based on failure theories has been used as a judge of the reliability of structural design since the 18th century. A number of failure theories have been drawn up to achieve predictions of safety factor for different materials and situations.

A failure theory is a criterion to predict the failure of a specific solid material under a complex stress condition. According to the material properties and practical situations (such as pressure, temperature, and loading rate), the failure of a material is generally categorized as ductile failure (yield) and brittle failure (fracture).

For brittle materials, some popular failure criteria are: criteria based on invariants of the Cauchy stress tensor; the Tresca or maximum shear stress failure criterion, the Mohr-Coulomb failure criterion, the Drucker-Prager failure criterion, the Bresler-Pister failure criterion, and other criteria used for specific materials and conditions.

Mohr-Coulomb stress safety tool, based on the Mohr-Coulomb failure criterion, takes direct account of the tensile strength of the materials, are always used in brittle materials such as cast iron, concrete, and glass. The independent distributions of minimum and maximum principal stress are used to the calculations, in order to provide a distribution of safety factor throughout the simulation objects. Typically speaking, the minimum value of safety factor appeared in the distribution is taken into account for the failure analysis. The safety factor can be calculated by

$$\text{Safety Factor} = [\frac{\sigma_1}{S_{tensile\,limit}} + \frac{\sigma_3}{S_{compressive\,limit}}]^{(-1)} \tag{5.1}$$

where σ_1 is the maximum tensile principal stress and σ_3 is the minimum compressive principal stress, $S_{tensile\,limit}$ is the material's tensile limit, $S_{compressive\,limit}$ is the material's compressive limit.

Criteria used to predict the failure of ductile materials are usually called yield criteria. Commonly used failure criteria for ductile materials are: the Tresca or maximum shear stress criterion, the von Mises yield criterion (maximum equivalent stress failure theory), the Gurson yield criterion, the Hosford yield criterion, the Hill yield criteria and various criteria based on the invariants of the Cauchy stress tensor.

Of the four failure theories supported by the Mechanical application in ANSYS Workbench, von Mises-Hencky theory is generally considered as the most appropriate for ductile materials such as aluminum, brass, and steel. Von Mises-Hencky theory states that failure by yielding under a combination of stresses occurs when the energy of distortion equals or exceeds the energy of distortion in the tensile test when the yield strength is reached. The safety factor can be calculated by

$$\text{Safety Factor} = \frac{S_{limit}}{\sigma_e} \tag{5.2}$$

where σ_e is the maximum equivalent stress and S_{limit} is a specific stress limit, which could

be the yield strength of the material or the ultimate strength of the material depending on specific situation.

Even though the desiring value of the safety factor has to be material dependent and be specific to a material composition and manufacturing and may also be influenced by the environment, the minimum value of the safety factor for the structural glass is suggested to set as 3, with both the experimental results of Vicat and Tim McFarlane [KHO 04].

In this work, the Equivalent stress safety tool inserted in ANSYS Workbench is used to value the durability of the alley steel barrel, and the Mohr-Coulomb stress safety tool is used to value the durability of the transparent windows. A minimum value of 3 of the safety factor of the glass blocks is expected to satisfy the requirement of the working environment.

5.3 Numerical Simulation

To explore the failure reasons of the "visual barrel" designed by Pham *et al.*, numerical simulations have been conducted with ANSYS Workbench. The modelling process, the material mechanical properties, and the boundary conditions are demonstrated in this section.

5.3.1 Modelling

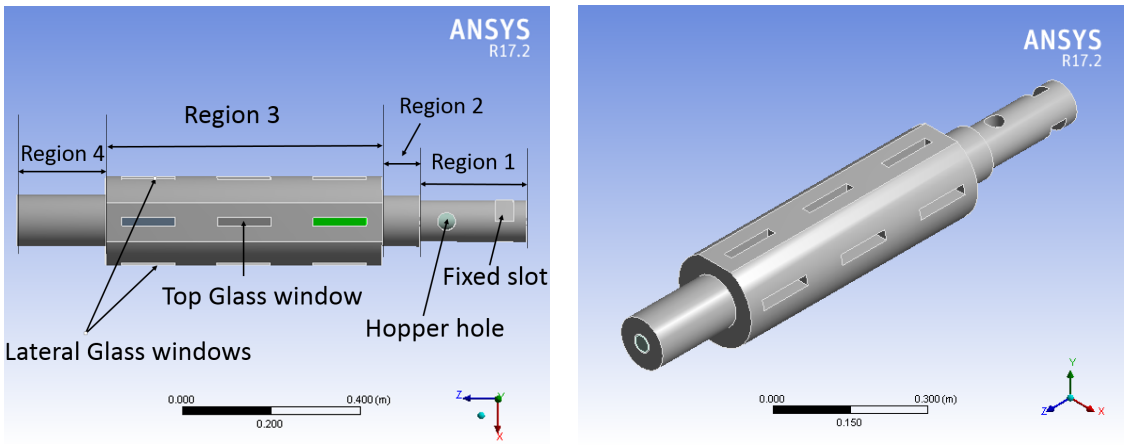

(a) Top view of the barrel

(b) 3D isometric view of the barrel

Figure 5.1: Perspectives of the barrel with transparent windows

A 3D model is built in ANSYS Workbench DesignModeler. The barrel embedded 3 glass blocks has the same dimensions as Pham's model, illustrated in Fig. 1.17 in Chapter 1. But the auxiliary structures like the bases, joints, and wedges, are treated as part of the barrel to simplify the complicated contact problems and reduce the calculation duration. The top view and the 3D isometric view of the barrel are shown in Fig. 5.1. It can be

Tableau 5.1: Dimensions of the different parts of barrel

Dimension(mm)	Value
Length of total barrel	1145
Diameter of barrel bore	40.1
Length of region 1	240
Diameter of region 1	93
Length of region 2	85
Diameter of region 2	115
Length of region 3	620
Diameter of region 3	200
Length of region 4	200
Diameter of region 4	115
Length of glass windows	120
Distance of adjacent blocks	80

found that the barrel has 4 connected regions from the hopper side to the die side. The first region includes 2 slots to fix the barrel and the hopper hole, the second region has a bigger diameter connecting the first region and the visual region, the third region is the main part of the barrel, which has 3 pieces of glass with 9 transparent windows for visualization and will be wrapped with heaters in working situations. The light sources can access through the 3 top windows and cameras can be used to record the plastication process through the 6 lateral windows. The last region has several screw holes to fix the other side of the barrel.

The dimensions of the different regions of the barrel are given in Table 5.1.

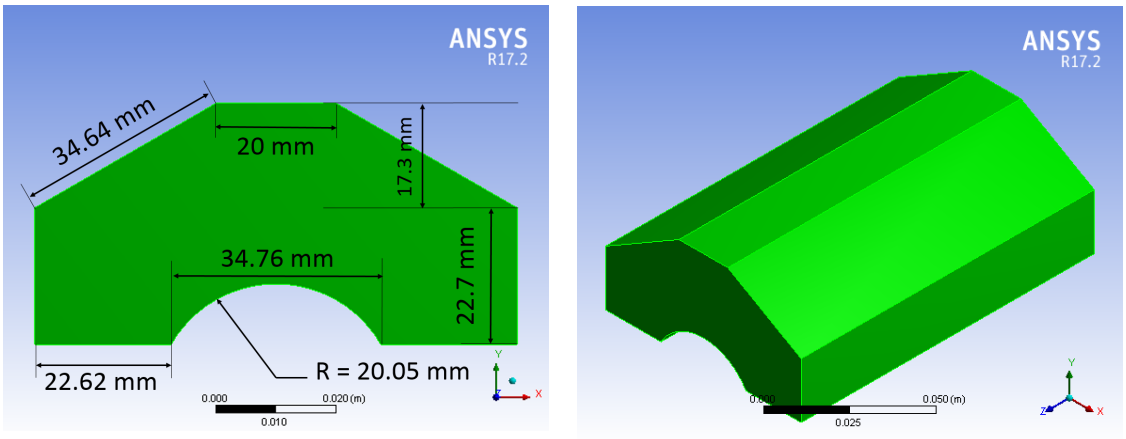

(a) Left view of a glass block

(b) 3D isometric view of a glass block

Figure 5.2: Perspectives of a glass block

Fig. 5.2 (a) and (b) present the dimensions and shape of the glass blocks. As it can be found from the figures, the underside of the glass is cut into a cylindrical shape for

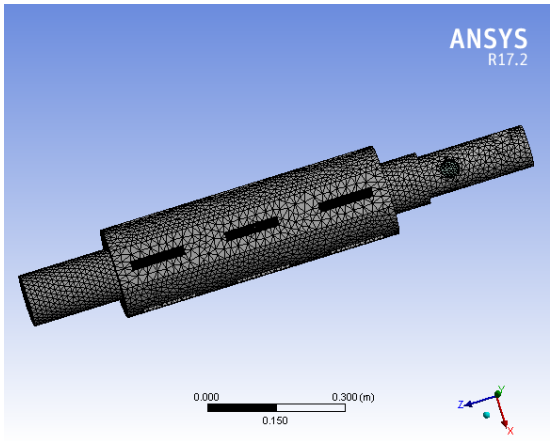

Figure 5.3: Meshing of the barrel

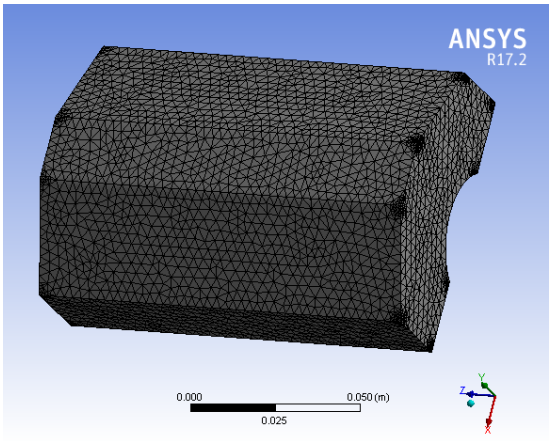

Figure 5.4: Meshing of a glass block

the passage of a screw of 40 mm in diameter. The radius of this arc is 20.05 mm to prevent the screw from touching the glass surface during its deformation due to temperature and pressure. Each glass window is 120 mm in length, 80 mm in width, and 40 mm in thickness. Over the 620 mm (Region 3 in Fig5.1(a)) length of the main part of the barrel, the three glass blocks ensure the observation on the feed zone, compression zone and metering zone of the screw, separately.

5.3.2 Meshing

Meshing is of great importance in FEM simulation, as the calculation duration and analysis accuracy counts on the size and orientations of the mesh. The parametric model created by DesignModeler is divided into numbers of small pieces, which are called mesh elements. The output of the mesh of the barrel and the glass blocks are displayed separately in Fig. 5.3 and Fig. 5.4. The total number of the node is 489572 and the total number of elements is 307144. The type of mesh control used in the present work is Contact Sizing, and a second level of Refinement for the 48 vertices on the 3 glass blocks is inserted to avoid the diverge problems caused by the stress concentration of the glass corners. The total node numbers and total element numbers are six in digit in the current mesh geometry, besides, a finer mesh, which leads to an evident growth of the calculation duration, has been conducted has negligible influence on the simulation results, which indicates that the mesh quality is high enough.

5.3.3 Material mechanical properties

The material used for the main body of the barrel is the alloy steel 41CrAlMo7.10TR. At the beginning of the simulations, the transparent windows are set as glass BK7, utilized in the existing equipment, then Sapphire is set as the transparent windows in the simulation

Tableau 5.2: Material properties

	Unit	Glass BK7	Sapphire	Steel
Young's modulus	Pa	8.2e+11	3.45e+11	2.15e+11
Poisson ratio		0.208	0.28	0.3
Density	kg/m^3	2510	3970	7850
Thermal dilatation	1/°C	8.6e-06	5.3e-07	1.29e-05
Tensile yield strength	Pa	6.9e+07	3.0e+08	9.0e+08
Compressive yield strength	Pa	6.9e+08	2.0e+09	9.0e+08
Thermal conductivity	W/(m*k)	1.114	20	40

to study its competency under the same boundary conditions. The mechanical properties of these materials are presented in Table 5.2.

5.3.4 Boundary conditions

Fixed support is applied to the surface of Region 1, which means that no displacement is allowed in this region. Therefore, the temperature in this region is always set at room temperature to avoid the thermal expansion caused by high-temperature field. In the practical experiment, the working temperature depends on the polymer that been used, but mostly it is lower than 300. In this section, the temperature of main part of the barrel (Region 3) is set as 50°C, 100°C, 150°C and 240°C, separately, to study the effect of temperature on the safety factor of the glass windows.

A pressure is applied perpendicularly to the inner surface of the barrel and the glass where the screw passes through. For the initial calculation, a uniform pressure of 200 bar is utilized. Then, a multi-function pressure profile is adopted to simulate the practical plastication environment.

The film coefficient of convection of the 9 window planes at ambient temperature 22°C is taken as 10 $W/(m^2 * C)$. The heat flow on the inner surface of the barrel is set as 0, it is treated to be perfectly insulated.

The contact types used in ANSYS Workbench include bonded, frictional, frictionless, rough, no separation. In this section, to study the influence of contact type between glass blocks and barrel on the safety factor of the glass windows, bonded, frictionless and frictional contact type are conducted. In air at atmospheric pressure, the friction coefficients between metal and glass are typically from 0.5 to 0.7, depending on the shear properties of the metal involved [BUC 73]. In this work, the friction coefficient between glass BK7 and metal is set as 0.6.

5.4 Results and discussion

In this section, the temperature distribution, safety factor and the total deformation of the steel barrel and glass blocks are demonstrated, under the boundary condition of 240°C in the region 3, 200 bar uniform pressure on the inner surface, and the contact condition of frictional contact type between the steel barrel and glass blocks. Besides, the influence of processing parameters, the material mechanical properties, the length of the glass windows, the pressure profile, and temperature field on the safety factor of the glass windows are discussed.

The overall temperature distribution is illustrated in Fig. 5.5(a). Region 1 (hopper side) has the minimum temperature of about 22°C as expected. The barrel temperature changes uniformly in Region 2. In Region 3 and Region 4, the temperature of the barrel is uniformly 240°C, the temperature of the glass windows have a lower temperature of about 220°C in the center and 240°C in the edge.

The total deformation of the barrel is shown in Fig. 5.5(b), and it can be found that the Region 1 of the barrel has no deformation as for the fixed support boundary condition in this part. Then the total deformation increases uniformly along the barrel, and the end side of the barrel (die side) has the accumulated largest deformation. A series of simulation experiments have been conducted to study the temperature field effect on the total deformation of the barrel, which is expected to increase linearly with the increasing temperature. The results show that: At 22°C, its maximum values is only 7 μm; At 100°C, the maximum value is 845 μm; At 200°C, the maximum value is 1932 μm; At 240°C, which is the simulation in this figure, the maximum value reaches 2367 μm. Therefore, the total deformation of the barrel enlarges with the increase of the temperature field.

The total deformation of a single glass block is shown in the Fig. 5.5(c). With a 100 times enlargement, it can be clearly found that the centered parts of the glass block have a evident displacement as for a bending deformation. This kind of bending deformation could be caused by the decrease of the yield strength of the corresponding top part of the barrel that is subtracted by the glass blocks and top view holes.

The safety factor of the barrel and one glass block are demonstrated in Fig. 5.5(d) and (e).It can be found that the value of safety factor of the barrel is uniformly 15, which is high enough for the working environment. While the minimum value of safety factor of the glass windows is about 1.45, which is lower than the desired value of 3, and corresponding to experimental results that the glass windows have been broken after a period of practical experiment. In Fig. 5.5 (e), the distribution of the value of safety factor of the glass block is corresponding to the total deformation distribution, which the center part of the glass block has a lower value of safety factor. In the following section, as for the sufficient safety factor of the steel barrel, only the safety factor of the glass windows is discussed.

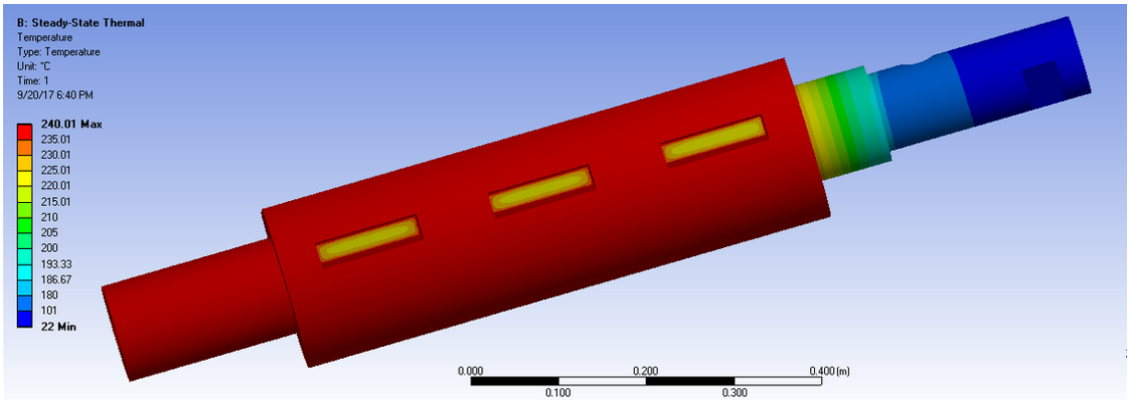

(a) Temperature distribution of the barrel

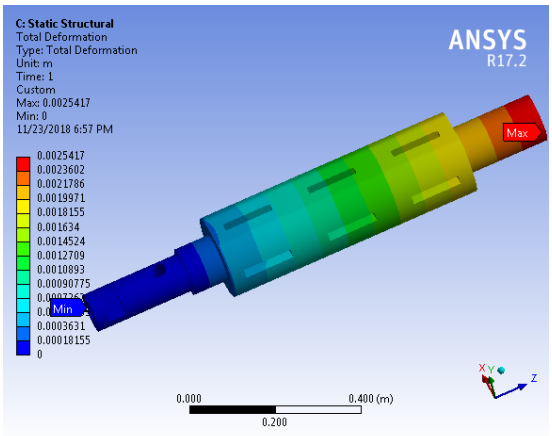

(b) Total deformation of the barrel

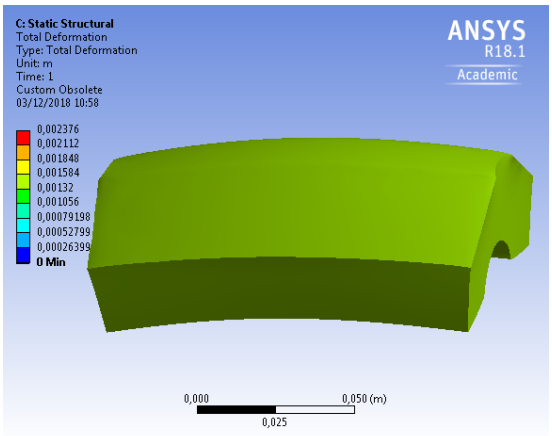

(c) Total deformation(100 times) of a glass block

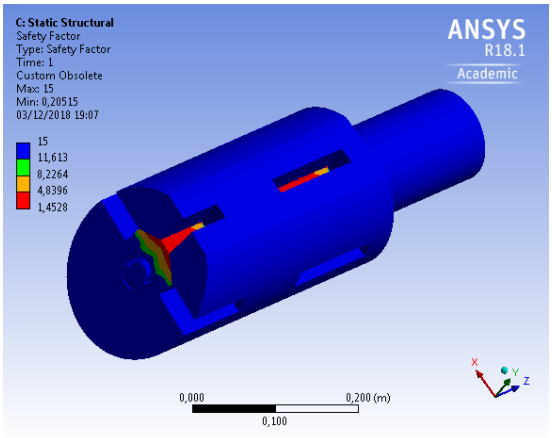

(d) Safety factor of the barrel

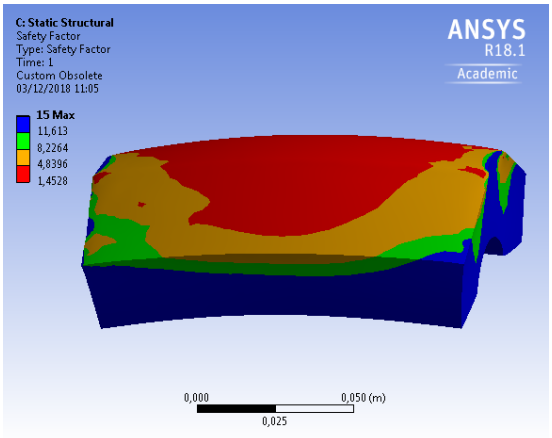

(e) Safety factor of a glass block

Figure 5.5: Simulation results with 200 bar inner pressure and 240°C temperature field and frictional contact type between barrel and glass blocks

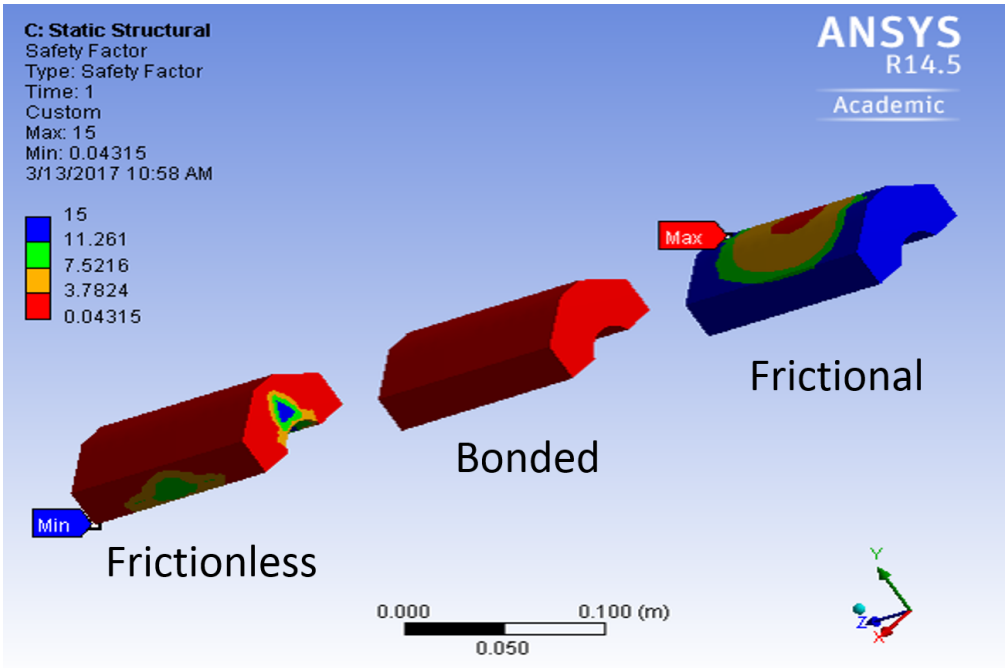

Figure 5.6: The safety factor distribution of the 3 glass blocks with different contact types under a temperature condition of 100°C (Friction coefficient between glass and steel is set as 0.6)

5.4.1 The effect of contact types on the safety factor

To study the influence of the contact type between the glass and the barrel on the safety factor of the glass blocks, a simulation experiment is conducted with 3 different contact types, frictionless, bonded, and frictional, setting for 3 pieces of glass blocks, respectively, under the same other boundary conditions like pressure and temperature field. As shown in Fig. 5.6, the safety factor presents huge difference with the different contact types. The bonded contact condition has the lowest safety factor of about 0.04. The reason could be that the alloy steel barrel has a bigger thermal dilatation coefficient than the glass blocks, as listed in Table 5.2, the bonded contact type leads to a bigger deformation for the glass blocks than it is expected under a temperature field of 240°C. As shown in Fig. 5.5 (e), the pressure field on the inner surface of the barrel leads to a bending deformation on the glass blocks, which is bad for the safety factor of the glass blocks because there is tensile stress produced in bending. For the frictionless contact type, and the edge parts of the glass block could have a larger deformation without the friction with the barrel. Therefore, the middle part of the glass block has a higher safety factor than the corner parts. The frictional contact type typically requires much more calculation time as a non-linear problem to be solved. It shows a gradient circle of the distribution of the safety factor, the middle part has a lower value of about 1.45. To be noted, the frictional contact condition is the real contact condition and the friction factor between glass and steel is set as 0.6 [BUC 73]. To conclude, the type of contact between the glass

window and steel barrel has an obvious influence on the safety factor of glass blocks, and the frictional contact type has a minimum safety factor of 1.45 under corresponding boundary conditions.

5.4.2 The effect of the length of glass windows on the safety factor

The effect of the length of glass windows on the safety factor has been investigated. To ensure the observation of at least one complete screw channel, the shorter window length is set as 45 mm. The simulation on the two models was conducted under the same boundary conditions (Fixed support on Region 1, frictionless support on Region 4). Fig. 5.7 shows the results of the safety factor of glass blocks of the two models under pressure field of 200 bar. The minimum value of the safety factor of the 45 mm windows is 3.5, which is higher than that of 120 mm windows, as is about 2.7. While a further study that with the temperature field of 240°C, the minimum value of safety factor of 45 mm windows displays the same value with the 120 mm windows. In summary, a shorter length of glass windows has a higher safety factor value under room temperature, while the length of the windows has little influence on the Safety Factor of the glass windows under a combined field of high temperature and pressure.

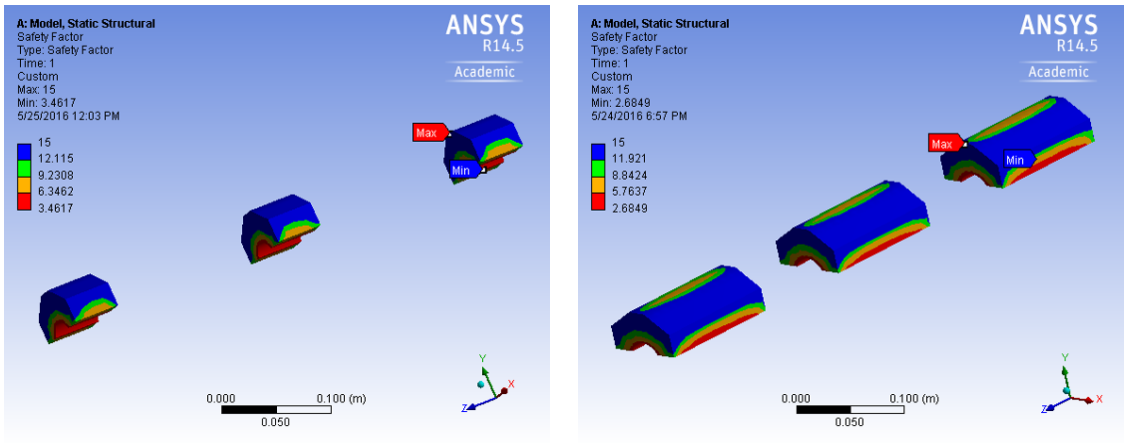

(a) 45 mm length

(b) 120 mm length

Figure 5.7: The safety factor of the glass windows in 2 different length

5.4.3 The effect of temperature on the safety factor

To study the influence of the temperature field on the safety factor of the glass windows, a series of simulation experiments with different temperature field is conducted. As demonstrated in Fig. 5.8, the minimum value of the safety factor of the glass blocks decreases evidently with the increasing of the temperature field. In the simulation with room temperature, the minimum value of the safety factor of the glass blocks is 5.35, which is quite

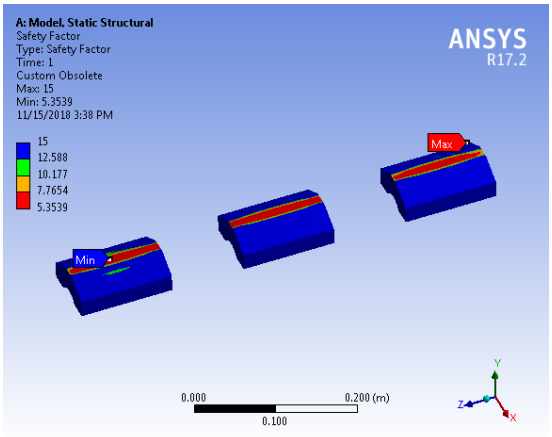

(a) Room temperature

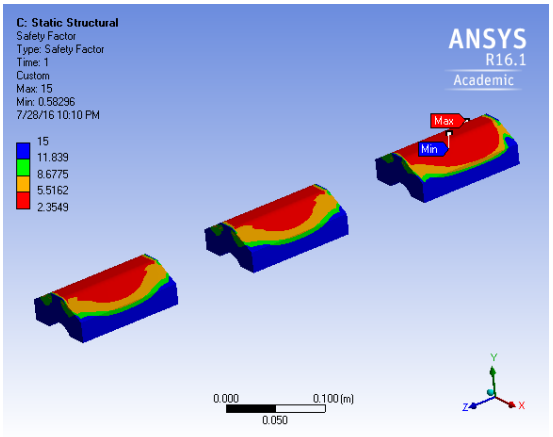

(b) Temperature field 100°C

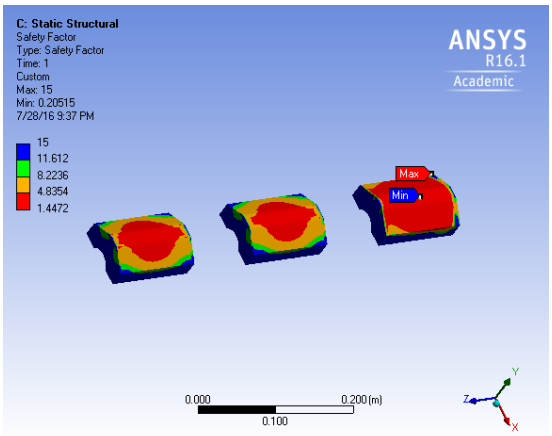

(c) Temperature field 240°C

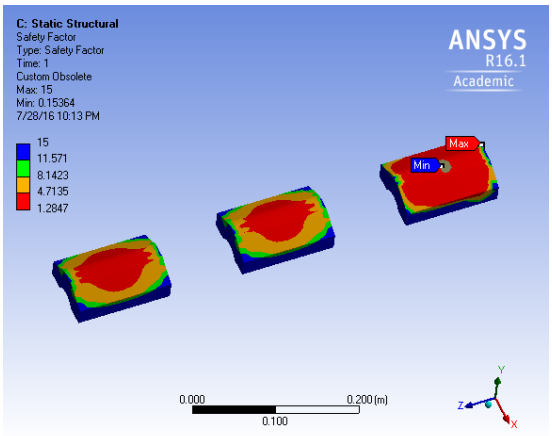

(d) Temperature field 300°C

Figure 5.8: The safety factor of the glass blocks in different temperature fields

robust, and it decreases to 2.35 with a temperature field of 100°C. At the working environment of 240°C, the valid safety factor is about 1.45, and it can continue to decrease to 1.28 when the temperature field reaches 300°C. The distribution of the value of the safety factor also changes in different temperature fields. In the room temperature, the top surface of the glass windows has a lower safety factor than the other parts, the reason could be that the top part has a more evident influence by the inner pressure without the influence of the temperature. While for the high-temperature field like 240°C, the value of the safety factor are lower in the center part. The first glass window is different with the other two glass blocks as for the fixed support is set at the beginning (Region 1) of the barrel. In conclusion, a higher temperature field leads to a lower valid value of the safety factor of the glass blocks, and it explains the breakage of the glass windows in the practical experiments.

5.4.4 The effect of pressure profile on the safety factor

The effect of pressure on the safety factor of glass windows is explored. In the previous simulation experiments, the pressure is always set uniformly as 200 bar along the inner surface of the barrel for simplification. In reality, it is important to note that the pressure along the inner surface is not uniform. Therefore, a piece-wise function of pressure is set in this simulation. The temperature boundary condition is kept as 240°C, and the other boundary conditions are mentioned in the previous section of Boundary conditions.

As shown in Fig. 5.9, which is a cross-section view of the pressure profile inside the barrel, a variable pressure is loaded on the inner face of the barrel. The blue region, which is the hopper side, has the atmosphere pressure, and the peak pressure of the red region locates on the third glass block. From the mathematical model of the previous chapter, the pressure profile can be simplified as a multi-linear function, as described in Fig. 5.10. The pressure begins with 1 bar on the hopper side, and increases along the interior surface of the barrel and reaches the maximum value of 200 bar at the end of the metering zone, then it drops down to a back pressure of 5 bar at the end of melting zone.

The results of the calculation with the variable loaded pressure is shown in Fig.5.10. It can be found that the first and second glass blocks with a low pressure have a higher safety factor, and the third glass window presents a minimal safety factor of 3.03 as for the effect of the peak pressure. Therefore, the pressure field has a pronounced influence on the safety factor of glass windows.

It should be noted that the result of the minimum value of safety factor in this simulation suffers from the limitations that, in polymer processing, where both heat transfer and flow take place, typical temperature variations may reach up to 200°C and pressure variations, 500 bar [TAD 79b]. Under such significant variations, the minimum value of the safety factor of the glass blocks could be lower than this result of 3.03, which explains the broken phenomenon of the glass blocks in the practical experiments.

5.4.5 The effect of material properties on the safety factor

The influence of mechanical properties of the window material on the safety factor of glass blocks is studied. The main mechanical properties of glass BK7, which is used in previous simulation experiment, are listed in the Table 5.2. A verification of 10% of each property is conducted in the simulation process to study its influence under the boundary condition of 240°C and 200 bar inner pressure, and the contact type between glass blocks and steel barrel is set as frictional. As demonstrated in the Table 5.3, the Young's modulus of the glass blocks and the friction coefficient between steel barrel and glass blocks have a negative correlation with the minimum value of safety factor of the glass blocks, the tensile yield strength of the glass blocks has a positive correlation with the valid safety factor of the glass blocks, and the variation of 10% of compressive yield strength have no influence on the safety factor. The reason is probably that the value of compressive strength of glass BK7 is much higher than the value of tensile strength, which becomes a limitation for the minimum value of the safety factor, i.e., the glass blocks can not bear

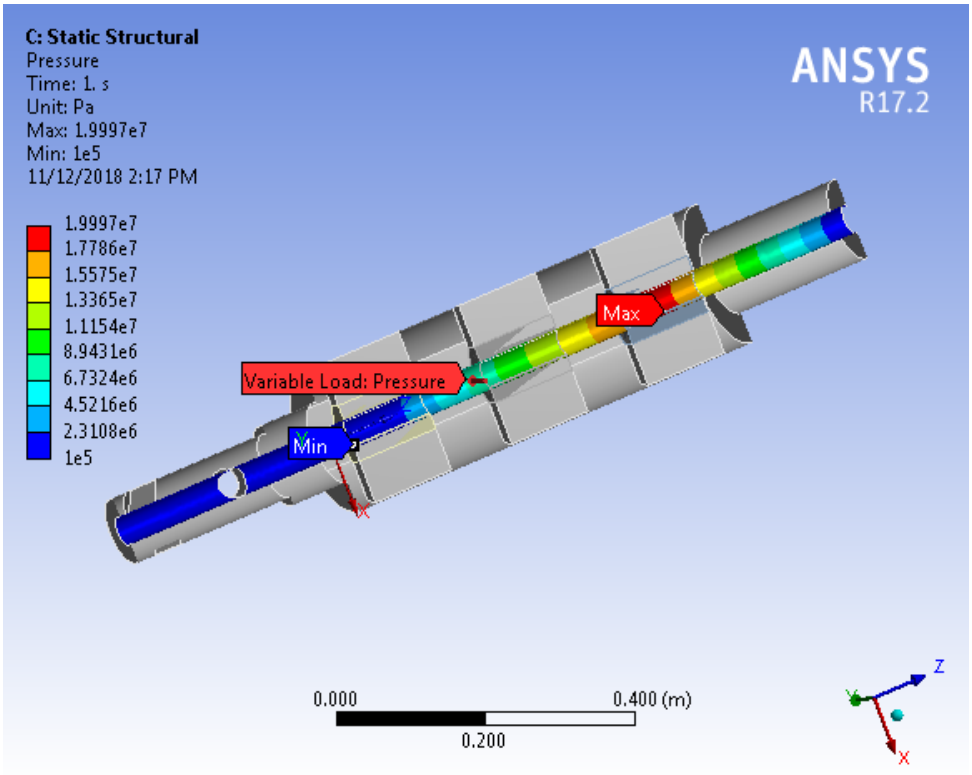

Figure 5.9: Cross-section view of variable load pressure on the inner surface of the barrel

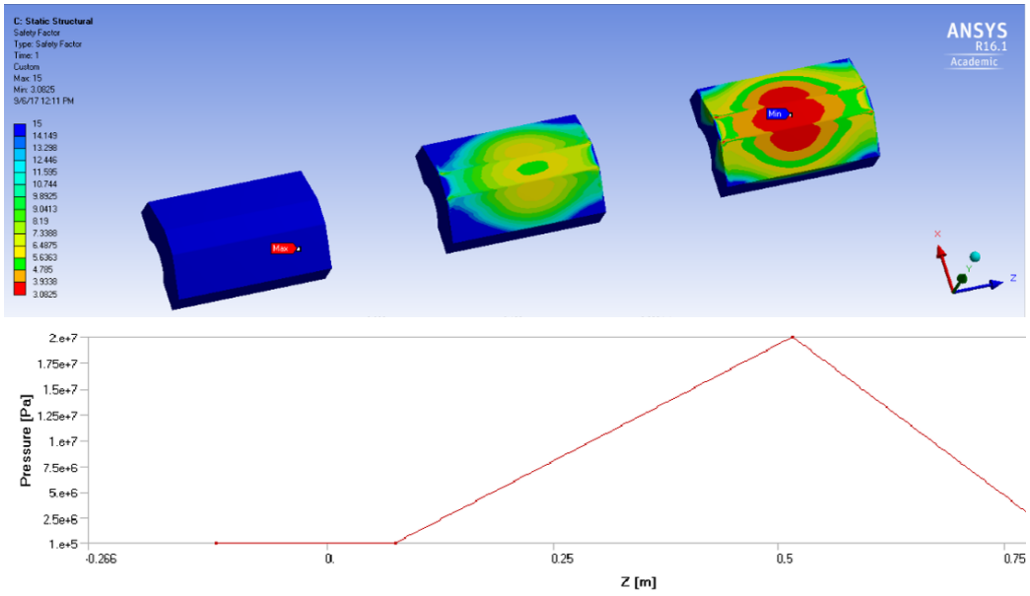

Figure 5.10: Effect of variable pressure profile on the safety factor of the glass blocks. The variable pressure starts with atmospheric pressure at the hopper side, and ends with back pressure at the nozzle side.

Tableau 5.3: The effect of material properties on the safety factor of the glass windows

Variations	Young's Modulus	Compressive yield strength	Tensile yield strength	Friction Coefficient
+10%	1.36	1.45	1.59	1.30
Original		**1.45**		
-10%	1.55	1.45	1.30	1.47

the tensile force of the inner surface pressure under a high temperature environment.

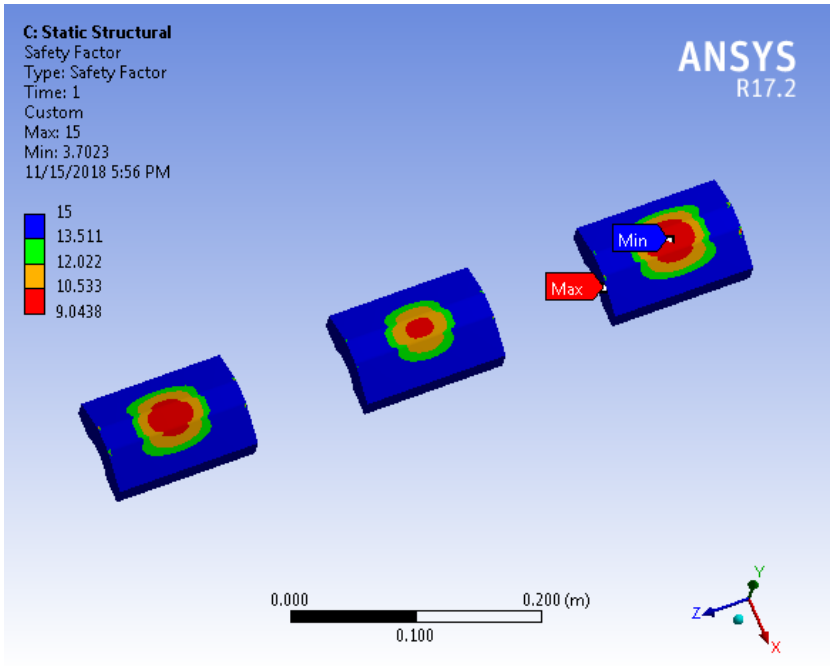

Figure 5.11: Safety factor distribution of sapphire blocks

Thus, transparent material with a higher tensile yield strength is considered to make the visual barrel more robust, and sapphire could be qualified. Besides, sapphire is much more resistant to brittle fracture than are glasses [BUC 73]. As seen from the Table 5.2, the tensile yield strength of sapphire is much higher than glass BK7, and the minimum value of the safety factor of sapphire in this boundary condition reaches to 8.96, as shown in Fig. 5.11, while in the same condition, the safety factor of glass BK7 is about 1.45, as shown in the previous Fig. 5.8(c). Thus, sapphire is of high mechanical performance to satisfy the requirements of the working environment.

5.5 Conclusions

In this chapter, Pham's model of a visual barrel is simplified and rebuilt within ANSYS Workbench to simulate the working environment of the practical experiments to analyze the failure reasons of the visual barrel. The Equivalent stress safety tool is used to value the durability of the steel barrel, the Mohr-coulomb stress tool is used as the criterion of the glass. A minimum value of safety factor of 3 is set as the requirement of reliability and durability. The effects of contact types, length of glass windows, temperature, pressure, and material properties on the safety factor of the glass windows are investigated in detail. It is found that:

(1) The temperature distribution, in the simulation result, is uniformly on the main region of the barrel, and the glass windows have a lower temperature of about 220°C in the center of the windows; The total deformation of the barrel increases with the enhancement of the temperature, at the 240°C, the total deformation reaches about 1.93 mm; The safety factor of the steel barrel is high enough but the glass blocks have an inefficient safety factor of 1.45.

(2) The temperature field has a big influence on the safety factor value of the glass blocks. The higher the temperature, the lower the value of safety factor. Under the frictional contact type, the minimum value of the safety factor of glass blocks is 1.45, which is lower than the expected value of 3.

(3) The contact types of glass blocks and steel barrel effect on the safety factor. The frictionless contact type and bonded contact type have a much lower safety factor than the practical frictional contact type.

(4) The length of glass windows have an influence on the safety factor at room temperature, but the influence disappeared in a high-temperature field.

(5) A higher pressure leads to a lower value of the safety factor of the glass blocks.

(6) The Young's modulus of the glass blocks and the friction coefficient between steel barrel and glass blocks have a negative correlation with the minimum value of the safety factor of the glass blocks, while the tensile yield strength of the glass blocks has a positive correlation. Sapphire is a robust material to satisfy the requirement of the working environment with a high tensile yield strength.

Finally, it should be mentioned that the results of the present study are sensitive to the simulated geometry and boundary conditions, thus it could only provide a gross approximation, with the absence of reliable experimental validation. After all, the presented numerical experiments are dedicated to provide an analysis of the failure theory of the visual barrel and provide suggestions for further study.

General conclusions and perspectives

General conclusion

In this thesis, the thermal homogeneity in single-screw plastication process has been studied. Firstly, thermal fluctuations in solid conveying and melt conveying are analyzed; Secondly, the laminar dispersion behavior of initial thermal fluctuations and inlet transient thermal fluctuations in the melting zone of plastication are investigated; Finally, the design and numerical simulation of an existing industrial sized visual barrel used in injection molding machines are reviewed, with the aim of analyzing the effect of operating conditions on the safety factor of the existing glass windows. The main conclusions drawn from this work are as follows:

In Chapter 2, the effect of solid bed velocity, solid bed voidage, and polymer properties on thermal fluctuations are quantified. Results show that changes in solid bed velocity and solid bed voidage could have a considerable influence on the temperature field at the end of the delay zone. Besides, small changes in the power-law index could lead to very large changes in the peak pressure, and the mechanical pressure fluctuations can also be a source of thermal fluctuations. Variations of the polymer consistency and power-law index could lead to non-neglected fluctuations of the throughput, which can be further related to the thermal fluctuations.

The laminar dispersion of initial thermal fluctuations in the melting zone of plastication is researched in Chapter 3. The peak of thermal fluctuations presented at the end of the metering zone increase with the enhancement of slug length in a Newtonian fluid. The results from ANSYS Polyflow are in agreement with our mathematical model, which showed the same tendency of the dispersion behavior of thermal fluctuations. The power-law behavior of fluid affects the dispersion behavior of thermal fluctuations. With the same throughput, temperature and backpressure, a fluid with the lower power-law index can make the thermal fluctuation disperse more evenly than with higher power-law index. The value of the peak temperature of thermal fluctuation decreases exponentially along the position of the metering section of the screw channel, therefore, a longer metering section in plastication process could help achieve a better thermal homogeneity in the melt flow. In both Newtonian and non-Newtonian fluid, concluded by both mathematical model and numerical simulation: temperature fluctuations disperse more evenly with time in a flow with high backpressure, whereas a pressure drop in the flow results in a breakthrough curve which presents a larger peak of fluctuation. It indicates that through

an increase of backpressure, to some degree, in practical polymer processing can expect a better thermal homogeneity at the end of the metering section of the screw channel.

In Chapter 4, the capacity of the drag and pressure driven flow to dampen transient inlet temperature disturbances occurring at the beginning of the metering zone of the screw channel is explored. The integral transform method for heat transfer in polymer melt flow with transient inlet temperature has been successfully used for the drag and pressure driven flow in a rectangular single screw channel. The steady-state eigenvalues are calculated to build the transient solution, and it was found that the knowledge of the lowest eigenvalue is sufficient to characterize the dampening efficiency of a flow. Besides, for any given flow, the high-frequency disturbances are dampened more efficiently than the low-frequency disturbances. The most important result is that a higher level of backpressure (positive pressure gradient) in the flow indeed result in a much more efficient dampening of the inlet temperature fluctuation.

In the last Chapter, the design and numerical simulation of an industrial-sized transparent barrel used in injection molding machines are conducted by using ANSYS Workbench, with the aim of analyzing the effect of operating conditions on the safety factor of the existing glass windows. The temperature distribution and the total deformation of the barrel under temperature and pressure fields are demonstrated. It was found that the safety factor of the steel barrel is high enough but the glass blocks have an inefficient safety factor of 1.45, compared with the expected value of 3. Furthermore, a contact problem between glass windows and steel barrel was carried out. The frictionless contact type and bonded contact type were found to have a much lower safety factor than the practical frictional contact type. The length of glass windows has a considerable effect on the safety factor at room temperature, but the difference can be neglected in a high-temperature field. Both the temperature field and pressure field have a big influence on the safety factor value of the glass blocks, and the higher the temperature or pressure, the lower the value of safety factor. The Young's modulus of the glass blocks and the friction coefficient between steel barrel and glass blocks have a negative correlation with the value of the safety factor of the glass blocks, while the tensile yield strength of the glass blocks has a positive correlation with the safety factor value. The results of these simulation experiments give a better understanding of the failure of the glass windows in Pham's equipment. If we look for another material that would be able to meet our requirements, it is found that sapphire is a robust material to satisfy the requirement of the working environment with an exceptionally high tensile yield strength.

Perspectives

After this thesis, the future work could be considered in these aspects:

- Mathematical modelings

  On the one hand, in the injection molding cycle, the mechanical time scale of the idles and restarts is a process parameter and it is completely different from the material time scale of the thermoplastic melt, which is a viscoelastic fluid. Therefore,

these relaxation phenomena are a form of fluctuations also. Investigation of the effects of the idle and restart time in the injection molding cycle on thermal fluctuations, from the modeling stand-point, could be very advantageous.

On the other hand, the barrel temperature fluctuation can be used as boundary condition to study the dispersion behavior of thermal fluctuations. Due to the laminar dispersion behavior with the initial condition has already been studied, the model with boundary condition can be formulated by replacing $\theta(x, y, \tau)$ with $\theta(x, y, \tau) - T_{wall}(x, \tau)$, where θ is the dimensionless thermal fluctuation, and T_{wall} is the barrel wall temperature. Besides, We want to extend the mathematical model of laminar dispersion from the metering zone to the compression zone of the screw channel. Due to the channel depth changes slowly in the compression zone, the lubrication theory will be used in this process.

- Numerical simulations

  Further numerical simulations are expected to conduct. Present work only used 2-D models as a simplification for the first calculation, which neglected the influence of the screw flights on the flow. A 3-D model can be developed for the drag and pressure driven flow in the screw channel and calculated with ANSYS Polyflow, in consideration of the circular flow in the cross section of the screw channel, to obtain more persuasive results.

- Experiment validations

  The effect of operating conditions on the safety factor of the existing glass windows, obtained by numerical simulation, are sensitive to the simulated geometry and boundary conditions, thus it could only provide a gross approximation, without the presence of reliable experimental validations. Besides, after solving the transparent window problems, the visual barrel can be further instrumented with temperature measurement sensors, and combined with a temperature-sensitive fluorescent dye, to conduct experiments on the study of thermal homogeneity in the plastication process.

  In addition, the visual barrel injection molding machine can be operated by replacing the glass blocks with metal blocks, and install pressure and temperature sensors at the end of delay zone, at the end of melting zone, and at the end of the metering zone, to conduct experimental measurements of fluctuations to verify the mathematical models on the delay zone temperature, peak pressure, and thermal fluctuations.

Bibliography

[ABE 11] ABEYKOON C., LI K., MCAFEE M., MARTIN P. J., NIU Q., KELLY A. L., DENG J.
A new model based approach for the prediction and optimisation of thermal homogeneity in single screw extrusion. *Control Engineering Practice*, vol. 19, n° 8, 2011, p. 862–874, Elsevier.

[ABE 12] ABEYKOON C., MARTIN P. J., KELLY A. L., BROWN E. C.
A review and evaluation of melt temperature sensors for polymer extrusion. *Sensors and actuators A: Physical*, vol. 182, 2012, p. 16–27, Elsevier.

[ABE 16a] ABEYKOON C.
Single screw extrusion control: A comprehensive review and directions for improvements. *Control Engineering Practice*, vol. 51, 2016, p. 69–80, Elsevier.

[ABE 16b] ABEYKOON C., KELLY A. L., BROWN E. C., COATES P. D.
The effect of materials, process settings and screw geometry on energy consumption and melt temperature in single screw extrusion. *Applied Energy*, vol. 180, 2016, p. 880–894, Elsevier.

[AGA 96] AGASSANT J.-F., AVENAS P., SERGENT J.-P., VERGNES B., VINCENT M.
La mise en forme des matières plastiques. Technique & Documentation-Lavoisier, 1996.

[AMA 88] AMANO O., UTSUGI S.
Temperature measurements of polymer melts in the heating barrel during injection molding. Part I. Temperature distribution along the screw axis in the reservoir. *Polymer Engineering & Science*, vol. 28, n° 23, 1988, p. 1565–1571, Wiley Online Library.

[ANN 79] ANNAPURNA N., GUPTA A.
Exact analysis of unsteady mhd convective diffusion. *Proceedings of the Royal Society of London. A. Mathematical and Physical Sciences*, vol. 367, n° 1729, 1979, p. 281–289, The Royal Society London.

[ANN 81] ANNAPURNA N., GUPTA A.
DISPERSION OF MATTER IN FLOW OF A BINGHAM PLASTIC IN A TUBE. *CHEMICAL ENGINEERING COMMUNICATIONS*, vol. 8, n° 4-6, 1981, p. 281–287, Taylor & Francis.

[BEN 03] BENDADA A., COLE K., LAMONTAGNE M., SIMARD Y.
A hollow waveguide infrared thermometer for polymer temperature measurement during injection moulding. *Journal of Optics A: Pure and Applied Optics*, vol. 5, n° 5, 2003, p. 464, IOP Publishing.

[BEN 04] BENDADA A., LAMONTAGNE M.
A new infrared pyrometer for polymer temperature measurement during extrusion moulding. *Infrared physics & technology*, vol. 46, n° 1-2, 2004, p. 11–15, Elsevier.

[BER 58] BERNHARDT E. C., MCKELVEY J. M.
Polymer Processing - New Engineering Specialty. *Mod. Plast.*, vol. july, n° 35, 1958, p. 154–155.

[BÉR 04] BÉREAUX Y., MOGUEDET M., RAOUL X., CHARMEAU J. Y., BALCAEN J., GRAEBLING D.
Series Solutions for Viscous and Viscoelastic Fluids Flow in the Helical Rectangular Channel of an Extruder Screw. *J. Non-Newtonian Fluid Mech.*, vol. 123, 2004, p. 237.

[BÉR 09] BÉREAUX Y., CHARMEAU J.-Y., MOGUEDET M.
A simple model of throughput and pressure development for single screw. *journal of materials processing technology*, vol. 209, n° 1, 2009, p. 611–618, Elsevier.

[BRO 60] BROWN G. M.
Heat or mass transfer in a fluid in laminar flow in a circular or flat conduit. *AIChE Journal*, vol. 6, n° 2, 1960, p. 179–183, Wiley Online Library.

[BRO 72] BROYER E., TADMOR Z.
Solids conveying in screw extruders part I: A modified isothermal model. *Polymer Engineering & Science*, vol. 12, n° 1, 1972, p. 12–24, Wiley Online Library.

[BRO 00] BROWN E., OLLEY P., COATES P.
In line melt temperature measurement during real time ultrasound monitoring of single screw extrusion. *Plastics, rubber and composites*, vol. 29, n° 1, 2000, p. 3–13, Taylor & Francis.

[BRO 04] BROWN E. C., KELLY A. L., COATES P. D.
Melt temperature field measurement in single screw extrusion using thermocouple meshes. *Review of scientific instruments*, vol. 75, n° 11, 2004, p. 4742–4748, AIP.

[BU 18] BU L., AGBESSI Y., BÉREAUX Y., CHARMEAU J.-Y.
Thermal homogeneity of plastication processes in single-screw extruders. *AIP Conference Proceedings*, vol. 1960 AIP Publishing, 2018, p. 120006.

[BUC 73] BUCKLEY D. H.
Friction behavior of glass and metals in contact with glass in various environments. , 1973.

[BUI 06] BUICK J., COSGROVE J.
Numerical simulation of the flow field in the mixing section of a screw extruder by the lattice Boltzmann model. *Chemical engineering science*, vol. 61, n° 10, 2006, p. 3323–3326, Elsevier.

[BUI 09] BUICK J.
Lattice Boltzmann simulation of power-law fluid flow in the mixing section of a single-screw extruder. *Chemical Engineering Science*, vol. 64, n° 1, 2009, p. 52–58, Elsevier.

[BUR 04] BUR A. J., ROTH S. C., SPALDING M. A., BAUGH D. W., KOPPI K. A., BUZANOWSKI W. C.
Temperature gradients in the channels of a single-screw extruder. *Polymer Engineering & Science*, vol. 44, n° 11, 2004, p. 2148–2157, Wiley Online Library.

[CAM 92] CAMPBELL G. A., SWEENEY P. A., FELTON J. N.
Experimental investigation of the drag flow assumption in extruder analysis. *Polymer Engineering & Science*, vol. 32, n° 23, 1992, p. 1765–1770.

[CEL 10] CELLERE A.
Injection molding of LGF-reinforced thermoplastics: numerical and experimental investigations of fibers breakage. , 2010.

[CHA 85] CHATWIN P., ALLEN C.
Mathematical Models of Dispersion in Rivers and Estuaries. *Chemical Engineering Journal*, vol. 17, n° 1, 1985, p. 119–149.

[CHA 95] CHANG R.-Y., LIN K.-J.
The hybrid FEM/FDM computer model for analysis of themeteirng section of a single-screw extruder. *Polymer Engineering & Science*, vol. 35, n° 22, 1995, p. 1748–1757, Wiley Online Library.

[CHA 97] CHAKRAVORTY S., ALLEN C., BROWN C.
In-line temperature measurement during polymer melt flow. *Polymer testing*, vol. 16, n° 5, 1997, p. 455–460, Elsevier.

[CHE 99] CHEROTO S., MIKHAILOV M., KAKAC S., COTTA R.
Periodic laminar forced convection: solution via symbolic computation and integral transforms. *International journal of thermal sciences*, vol. 38, n° 7, 1999, p. 613-621.

[CHI 95] CHIRUVELLA R. V., JALURIA Y., ABIB A.
Numerical simulation of fluid flow and heat transfer in a single-screw extruder with different dies. *Polymer Engineering & Science*, vol. 35, n° 3, 1995, p. 261–273, Wiley Online Library.

[CHO 80] CHOO K. P., NEELAKANTAN N. R., PITTMAN J. F. T.
Experimental deep-channel velocity profiles and operating characteristics for a single-screw extruder. *Polymer Engineering & Science*, vol. 20, n° 5, 1980, p. 349–356.

[CHU 70] CHUNG C. I.
New ideas about solids conveying in screw extruders. *SPE JOURNAL*, vol. 26, n° 5, 1970, p. 32.

[COT 86a] COTTA R., OZISIK M.
Laminar forced convection inside ducts with periodic variation of inlet temperature. *International Journal of Heat and Mass Transfer*, vol. 29, n° 10, 1986, p. 1495 - 1501.

[COT 86b] COTTA R., ÖZIŞIK M.
Transient forced convection in laminar channel flow with stepwise variations of wall temperature. *The Canadian Journal of Chemical Engineering*, vol. 64, n° 5, 1986, p. 734–742, Wiley Online Library.

[DAR 56] DARNELL W. H., MOL E. A. J.
Solids Conveying in Extruders. *Soc. Plast. Eng. J.*, , n° 12, 1956, p. 20–28, Carl Hanser Verlag.

[DEE 13] DEEN W.
Analysis of Transport Phenomena. Oxford University Press, 2013.

[DEN 03] DENYS K.
Flow of polymer solutions through porous media. Thèse de doctorat, Delft University, 2003.

[DON 71a] DONOVAN R. C., THOMAS D., LEVERSEN L.
An experimental study of plasticating in a reciprocating-screw injection molding machine. *Polymer Engineering & Science*, vol. 11, n° 5, 1971, p. 353–360, Wiley Online Library.

[DON 71b] DONOVAN R.
A theoretical melting model for plasticating extruders. *Polymer Engineering & Science*, vol. 11, n° 3, 1971, p. 247–257, Wiley Online Library.

[DON 74] DONOVAN R. C.
The Plasticating Process in Injection Molding. *Polym. Eng. Sci.*, vol. 14, 1974, p. 101.

[DON 91] DONTULA N., SUKANEK P., DEVANATHAN H., CAMPBELL G.
An experimental and theoretical investigation of transient melt temperature during injection molding. *Polymer Engineering & Science*, vol. 31, n° 23, 1991, p. 1674–1683, Wiley Online Library.

[DUT 88] DUTTA B., RAY P., BARMAN B.
Exact analysis of laminar dispersion in non-Newtonian flowExakte Analyse einer laminaren Dispersion in einer Nicht-Newtonschen Strömung. *Wärme-und Stoffübertragung*, vol. 23, n° 1, 1988, p. 39–43, Springer.

[ECC 58] ECCHER S., VALENTINOTTI A.
Experimental determination of velocity profiles in an extruder screw. *Industrial & Engineering Chemistry*, vol. 50, n° 5, 1958, p. 829–836, ACS Publications.

[ELB 83] ELBIRLI B., LINDT J. T., GOTTGETREU S. R., BABA S. M.
Mathematical modeling of melting of polymers in barrier-screw extruders. *Polymer Engineering & Science*, vol. 23, n° 2, 1983, p. 86–94.

[ELB 84] ELBIRLI B., LINDT J., GOTTGETREU S., BABA S.
Mathematical modeling of melting of polymers in a single-screw extruder. *Polymer Engineering & Science*, vol. 24, n° 12, 1984, p. 988–999, Wiley Online Library.

[ESS 94] ESSEGHIR M., SERNAS V.
On the measurements of the radial temperature distribution in an extruder channel. *Advances in Polymer Technology: Journal of the Polymer Processing Institute*, vol. 13, n° 2, 1994, p. 133–140, Wiley Online Library.

[FAK 14] FAKOOR-PAKDAMAN M., ANDISHEH-TADBIR M., BAHRAMI M.
Unsteady laminar forced-convective tube flow under dynamic time-dependent heat flux. *Journal of Heat Transfer*, vol. 136, n° 4, 2014, p. 041706, American Society of Mechanical Engineers.

[FAN 91] FANG S., CHEN L., ZHU F.
Studies on the theory of single screw plasticating extrusion. Part II: Non-plug flow solid conveying. *Polymer Engineering & Science*, vol. 31, n° 15, 1991, p. 1117–1122.

[FER 14a] FERNANDES C., PONTES A. J., VIANA J. C., NÓBREGA J. M., GASPAR-CUNHA A.
Modeling of Plasticating Injection Molding Experimental Assessment. *International Polymer Processing*, vol. 29, n° 5, 2014, p. 558–569.

[FER 14b] FERNANDES C., PONTES A., VIANA J., NÓBREGA J., GASPAR-CUNHA A.
Modeling of Plasticating Injection Molding–Experimental Assessment. *International Polymer Processing*, vol. 29, n° 5, 2014, p. 558–569, Carl Hanser Verlag.

[FER 18] FERNANDES C., PONTES A. J., VIANA J. C., GASPAR-CUNHA A.
Modeling and Optimization of the Injection-Molding Process: A Review. *Advances in Polymer Technology*, vol. 37, n° 2, 2018, p. 429–449, Wiley Online Library.

[FOU 16] FOUNDATION E. M.
The New Plastics Economy: Rethinking the future of plastics. World Economic Forum, 2016.

[GAO 00] GAO F., JIN Z., CHEN X.
A visual barrel system for study of reciprocating screw injection molding. *Polymer Engineering & Science*, vol. 40, n° 6, 2000, p. 1334–1343.

[GAS 00] GASPAR-CUNHA A.
Optimisation of Single Screw Extrusion. Thèse de doctorat, PhD. Thesis, University of Minho, Guimarães, Portugal, 2000.

[GHO 96] GHOREISHY M., RAFIZADEH M.
Numerical simulation of thermoplastic melt flow in single screw extruder using finite element method. *Plastics rubber and composites processing and applications*, vol. 25, n° 3, 1996, p. 120–125, Institute of Materials.

[GIL 70a] GILL W. N., SANKARASUBRAMANIAN R.
Exact analysis of unsteady convective diffusion. *Proceedings of the Royal Society of London A: Mathematical, Physical and Engineering Sciences*, vol. 316, n° 1526, 1970, p. 341–350, The Royal Society.

[GIL 70b] GILL W., SANKARASUBRAMANIAN R.
Exact analysis of unsteady convective diffusion. *Proceedings of the Royal Society of London. A. Mathematical and Physical Sciences*, vol. 316, n° 1526, 1970, p. 341–350, The Royal Society London.

[HAN 90] HAN C. D., LEE K. Y., WHEELER N. C.
An experimental study on plasticating single-screw extrusion. *Polymer Engineering & Science*, vol. 30, n° 24, 1990, p. 1557–1567, Wiley Online Library.

[HUM 11] HUMINIC G., HUMINIC A.
Heat transfer characteristics in double tube helical heat exchangers using nanofluids. *International Journal of Heat and Mass Transfer*, vol. 54, n° 19-20, 2011, p. 4280–4287, Elsevier.

[IWK 15] IWKO J., STELLER R., WRÓBLEWSKI R., KACZMAR J.
Experimental verification of computer model for polymer plastication process in injection molding. *Polimery*, vol. 60, 2015.

[IWK 18] IWKO J., STELLER R., WRÓBLEWSKI R.
Experimentally Verified Mathematical Model of Polymer Plasticization Process in Injection Molding. *Polymers*, vol. 10, n° 9, 2018, p. 968, Multidisciplinary Digital Publishing Institute.

[JOH 14] JOHN A., NIDHI M.
Modelling and Analysis of an Automotive Bumper Used for a Low Passenger Vehicle. *International Journal Of Engineering Trends And Technology (IJETT)*, vol. 15, n° 7, 2014, p. 344.

[KAC 72] KACIR L., TADMOR Z.
Solids conveying in screw extruders part iii: The delay zone. *Polymer Engineering & Science*, vol. 12, n° 5, 1972, p. 387–395, Wiley Online Library.

[KAK 73] KAKAÃ§ S., YENER Y.
Exact solution of the transient forced convection energy equation for timewise variation of inlet temperature. *International Journal of Heat and Mass Transfer*, vol. 16, n° 12, 1973, p. 2205 - 2214.

[KAK 90a] KAKAC S., LI W., COTTA R. M.
Unsteady Laminar Forced Convection in Ducts With Periodic Variation of Inlet Temperature. *Journal of Heat Transfer*, vol. 112, n° 4, 1990, p. 913–920.

[KAK 90b] KAKAÇ S., LI W., COTTA R.
Unsteady laminar forced convection in ducts with periodic variation of inlet temperature. *Journal of Heat Transfer*, vol. 112, n° 4, 1990, p. 913–920, American Society of Mechanical Engineers.

[KEL 06] KELLY A. L., BROWN E. C., COATES P. D.
The effect of screw geometry on melt temperature profile in single screw extrusion. *Polymer Engineering & Science*, vol. 46, n° 12, 2006, p. 1706–1714, Wiley Online Library.

[KHO 04] KHORASANI N.
Design principles for glass used structurally. Department of Building Science, Univ., 2004.

[KIM 95] KIM S., KWON T.
Development of numerical simulation methods and analysis of extrusion processes of particle-filled plastic materials subject to slip at the wall. *Powder technology*, vol. 85, n° 3, 1995, p. 227–239, Elsevier.

[KLE 68] KLEIN, TADMOR
Operating Characteristics of a Plasticating Extruder, in Computer Programs for Plastics Engineers. Van Nostrand Reinhold Co., 1968.

[KUM 17] KUMAR S., DUBEY N.
Investigation and Thermal Analysis of Heat Dissipation Rate of Single Cylinder SI Engine. , 2017.

[LAU 14] LAUNAY J., ALLANIC N., MOUSSEAU P., DETERRE R., MADEC Y.
Intrusive measurement of polymer flow temperature. *Polymer Engineering & Science*, vol. 54, n° 12, 2014, p. 2806–2814, Wiley Online Library.

[LIN 76] LINDT J. T.
A dynamic melting model for a single-screw extruder. *Polymer Engineering & Science*, vol. 16, n° 4, 1976, p. 284–291.

[LIN 81] LINDT J. T.
Pressure development in the melting zone of a single-screw extruder. *Polymer Engineering & Science*, vol. 21, n° 17, 1981, p. 1162–1166.

[LIN 85a] LINDT J. T.
Mathematical modeling of melting of polymers in a single-screw extruder a critical review. *Polymer Engineering & Science*, vol. 25, n° 10, 1985, p. 585–588.

[LIN 85b] LINDT J., ELBIRLI B.
Effect of the cross-channel flow on the melting performance of a single-screw extruder. *Polymer Engineering & Science*, vol. 25, n° 7, 1985, p. 412–418, Wiley Online Library.

[MAD 59] MADDOCK B. H.
A Visual Analysis of Flow and Mixing in Extruder Screws. *SPE. J.*, vol. 15, n° 383, 1959, p. 9.

[MIA 85] MIAW C., HASSON A., BALCH G.
Melt temperature measurement in a single screw extruder. *43 rd Annual Technical Conference, Society of Plastics Engineers, Inc*, 1985, p. 76–79.

[MIK 84] MIKHAILOV M. D., OZISIK M. N.
Unified analysis and solutions of heat and mass diffusion. , 1984.

[MOG 05] MOGUEDET M.
Développement d'un outil d'aide à la conception et au fonctionnement d'un ensemble vis/fourreau industriel. Thèse de doctorat, INSA de Lyon, 2005.

[MOH 61] MOHR W., CLAPP J., STARR F.
Flow patterns in a non-Newtonian fluid in a single-screw extruder. *Polymer Engineering & Science*, vol. 1, n° 3, 1961, p. 113–120, Wiley Online Library.

[MÜL 09] MÜLLER J., KUMMER S., FISCHER D.
New ultrasonic probes for in-line monitoring of polymer melts. *Measurement Science and Technology*, vol. 20, n° 9, 2009, p. 097002, IOP Publishing.

[NIE 97] NIETSCH T., CASSAGNAU P., MICHEL A.
Melt temperatures and residence times in an extruder by infrared spectroscopy. *International Polymer Processing*, vol. 12, n° 4, 1997, p. 307–315, Carl Hanser Verlag.

[PHA 13] PHAM T. L.
Plastification en injection des polymères fonctionnels et chargés. Thèse de doctorat, INSA de Lyon, 2013.

[PIL 04] DEL PILAR NORIEGA M., OSSWALD T. A., FERRIER N.
In line measurement of the polymer melting behavior in single screw extruders. *Journal of polymer engineering*, vol. 24, n° 6, 2004, p. 557–578, De Gruyter.

[PIN 15] PING W., CHEN G.
Environmental dispersion in a tidal wetland with sorption by vegetation. *Communications in Nonlinear Science and Numerical Simulation*, vol. 22, n° 1-3, 2015, p. 348–366.

[PUJ 08] PUJOS C., RÉGNIER N., DEFAYE G.
Determination of the inlet temperature profile of an extrusion die in unsteady flow. *Chemical Engineering and Processing: Process Intensification*, vol. 47, n° 3, 2008, p. 456–462, Elsevier.

[RAO 86] RAO N.
Computer Aided Design of Plasticating Screws. 1986.

[RAU 92] RAUWENDAAL C.
Conveying and Melting in Screw Extruders with Axial Screw Movement. *Int. Polym. Proc.*, vol. 17, 1992, p. 26.

[ROH 98] ROHE T., BECKER W., KREY A., NÄGELE H., KÖLLE S., EISENREICH N.
In-line monitoring of polymer extrusion processes by NIR spectroscopy. *Journal of Near Infrared Spectroscopy*, vol. 6, n° 1, 1998, p. 325–332, SAGE Publishing.

[RUB 08] RUBERG M., WATERFIELD R., ELSASS M., KELSAY S.
Experimental Study on the Energy Efficiency of Different Screw Designs for Injection Molding. *SPC ANTEC Conference Proceedings*, 2008, p. 474–477.

[SAR 04] SARKAR A., JAYARAMAN G.
The effect of wall absorption on dispersion in oscillatory flow in an annulus: application to a catheterized artery. *Acta Mechanica*, vol. 172, n° 3, 2004, p. 151–167.

[SCO 14] SCOTT G. D., KILGOUR D. M.
The density of random close packing of spheres. *Journal of Physics D: Applied Physics*, vol. 2, n° 6, 2014, p. 863–866.

[SHA 76a] SHAPIRO J., HALMOS A., PEARSON J.
Melting in single screw extruders. *Polymer*, vol. 17, n° 10, 1976, p. 905–918, Elsevier.

[SHA 76b] SHAPIRO J., HALMOS A., PEARSON J.
Melting in single screw extruders. *Polymer*, vol. 17, n° 10, 1976, p. 905–918.

[SIR 53] SIR GEOFFREY TAYLOR F. R. S.
Dispersion of soluble matter in solvent flowing slowly through a tube. *Proc. R. Soc. Lond. A*, vol. 219, n° 1137, 1953, p. 186–203.

[SON 11] SONG F., NI Y., TAN Z.
Optimization design, modeling and dynamic analysis for composite wind turbine blade. *Procedia Engineering*, vol. 16, 2011, p. 369–375, Elsevier.

[SPA 68] SPARROW E., FARIAS F. D.
Unsteady heat transfer in ducts with time-varying inlet temperature and participating walls. *International Journal of Heat and Mass Transfer*, vol. 11, n° 5, 1968, p. 837 - 853.

[SQU 71] SQUIRES P., WOLF C.
Designing extruders for quality performance. *SPE JOURNAL*, vol. 27, n° 4, 1971, p. 68.

[STE 08] STELLER R., IWKO J.
Polymer Plastication during Injection Molding. *Int. Polym. Proc.*, vol. 23, 2008, p. 252.

[STE 12] STEVENS M., COVAS J.
Extruder principles and operation. Springer Science & Business Media, 2012.

[SYR 97] SYRJÄLÄ S.
Numerical study of fully developed non-Newtonian fluid flow and heat transfer in a rectangular channel with a moving wall. *International communications in heat and mass transfer*, vol. 24, n° 1, 1997, p. 11–25, Elsevier.

[TAD 66] TADMOR Z.
Fundamentals of plasticating extrusion. I. A theoretical model for melting. *Polymer Engineering & Science*, vol. 6, n° 3, 1966, p. 185–190, Wiley Online Library.

[TAD 70] TADMOR Z., KLEIN I.
Engineering principles of plasticating extrusion. Van Nostrand Reinhold Co., 1970.

[TAD 79a] TADMOR Z., GOGOS C. G.
Principles of Polymer Processing. 1979.

[TAD 79b] TADMOR Z., GOGOS C. G.
Principles of Polymer Processing. John Wiley, 1979.

[TAD 13] TADMOR Z., GOGOS C. G.
Principles of polymer processing. John Wiley & Sons, 2013.

[TED 71] TEDDER W.
NEW THEORY OF SOLIDS CONVEYING IN SINGLE-SCREW EXTRUDERS. *SPE JOURNAL*, vol. 27, n° 10, 1971, p. 68.

[VER 14] VERA-SORROCHE J., KELLY A. L., BROWN E. C., GOUGH T., ABEYKOON C., COATES P. D., DENG J., LI K., HARKIN-JONES E., PRICE M.
The effect of melt viscosity on thermal efficiency for single screw extrusion of HDPE. *Chemical Engineering Research and Design*, vol. 92, n° 11, 2014, p. 2404 - 2412.

[VER 15] VERA-SORROCHE J., KELLY A. L., BROWN E. C., COATES P. D.
Infrared melt temperature measurement of single screw extrusion. *Polymer Engineering & Science*, vol. 55, n° 5, 2015, p. 1059–1066, Wiley Online Library.

[WIL 99] WILCZYNSKI K.
Single-screw extrusion model for plasticating extruders. *Polymer-Plastics Technology and Engineering*, vol. 38, n° 4, 1999, p. 581–608.

[XU 10] XU J., LU T., HODSON H., FLECK N.
Analysis of thermal dispersion in an array of parallel plates with fully-developed laminar flow. *International Journal of Heat and Fluid Flow*, vol. 31, n° 1, 2010, p. 57–69.

[YAN 08] YANG Y., YANG W., ZHONG H.
Temperature distribution measurement and control of extrusion process by tomography. *2008 IEEE International Workshop on Imaging Systems and Techniques* IEEE, 2008, p. 170–174.

[YU 81] YU J.
Dispersion in laminar flow through tubes by simultaneous diffusion and convection. *Journal of Applied Mechanics*, vol. 48, n° 2, 1981, p. 217–223, American Society of Mechanical Engineers.

[YUN 01] YUNG K. L., XU Y.
Analysis of a Melting Model for an Extruder with Reciprocation. *J. Mater. Process. Technol.*, vol. 117, 2001, p. 21.

[YUN 02] YUNG K., XU Y., LAU K.
Simulation of transient process in melting section of reciprocating extruder. *Polymer*, vol. 43, n° 3, 2002, p. 983–988, Elsevier.

[YUN 03] YUNG K. L., XU Y., LAU K. H.
Transient Melting Models for the Three Stages of Reciprocating Extrusion. *J. Mater. Process. Technol.*, vol. 139, 2003, p. 170.

[ZEH 67] ZEHEV TADMOR I. D., KLEIN I.
Melting in plasticating extuders theory and experiments. *Polymer engineering and Science*, vol. 7, n° 3, 1967, p. 198–217.

[ZHU 91] ZHU F., CHEN L.
Studies on the theory of single screw plasticating extrusion. Part I: A new experimental method for extrusion. *Polymer Engineering & Science*, vol. 31, n° 15, 1991, p. 1113–1116.

[ZHU 01] ZHU F.
Extrusion theory and application. *China Light Industry Press, Beijing*, , 2001, p. 41–48.

FOLIO ADMINISTRATIF

THESE DE L'UNIVERSITE DE LYON OPEREE AU SEIN DE L'INSA LYON

NOM: **BU** DATE de SOUTENANCE: 14 March 2019
Prénoms: **Liangxiao**

TITRE: Study of Thermal Homogeneity in Single-Screw Plastication Process

NATURE : Doctorat Numéro d'ordre: 2019LYSEI014

Ecole doctorale: Mécanique, Énergétique, Génie Civil, Acoustique (ED 162 MEGA)

Spécialité: GÉNIE MÉCANIQUE

RESUME: Single-screw plastication, used in extrusion and in injection molding, is a major way of processing commodity thermoplastics. In injection molding, a high level of reliability is usually achieved that makes this process ideally suited to mass market production. Nonetheless, process fluctuations still appear that make molded part quality control an everyday issue. In this work, a combined modeling of plastication, throughput calculation, and laminar dispersion are used, to investigate how thermal fluctuations could generate and propagate along the screw length and affect the melt homogeneity at the end of the metering section. To do this, we used plastication models to relate changes in processing parameters to changes in the plastication length. Moreover, a simple model of throughput calculation is used to relate the screw geometry, the polymer rheology, and the processing parameters to get a good estimate of the mass flow rate. Hence, we found that the typical residence time in a single screw is around one-tenth of the thermal diffusion timescale. This residence time is too short for the dispersion coefficient to reach a steady state but too long to be able to neglect radial thermal diffusion and resort to a purely convective solution. Therefore, a full diffusion/convection problem has to be solved with a base flow described by the classic pressure and drag velocity field. The major importance of the processing parameters in the breakthrough curve of arbitrary temperature fluctuations at the end of the metering section of the injection molding screw is demonstrated. When the flow back-pressure is high, the temperature fluctuation is spread more evenly with time, whereas a pressure drop in the flow will results in a breakthrough curve which presents a larger peak of fluctuation. A commercial Computational Fluid Dynamics (CFD) software, ANSYS Polyflow, was used to verify the model.

MOTS-CLÉS: Numerical simulation, Single-screw plastication, Thermal fluctuation, Drag and pressure flow, ANSYS Polyflow, ANSYS Workbench

Laboratoire (s) de recherche : Laboratoire de Mécanique des Contacts et des Structures (LaMCoS), UMR CNRS 5259 - INSA de Lyon

Directeur de thèse: **Yves BEREAUX** Co-Directeur de thèse: **Jean-Yves CHARMEAU**

Président de jury: **Thierry BARRIERE**

Composition du jury: **Thierry BARRIERE**, **Nadine ALLANIC**, **Yves BEREAUX**, **Nicolas REGNIER**, **Claire BARRES**, **Jean-Yves CHARMEAU**